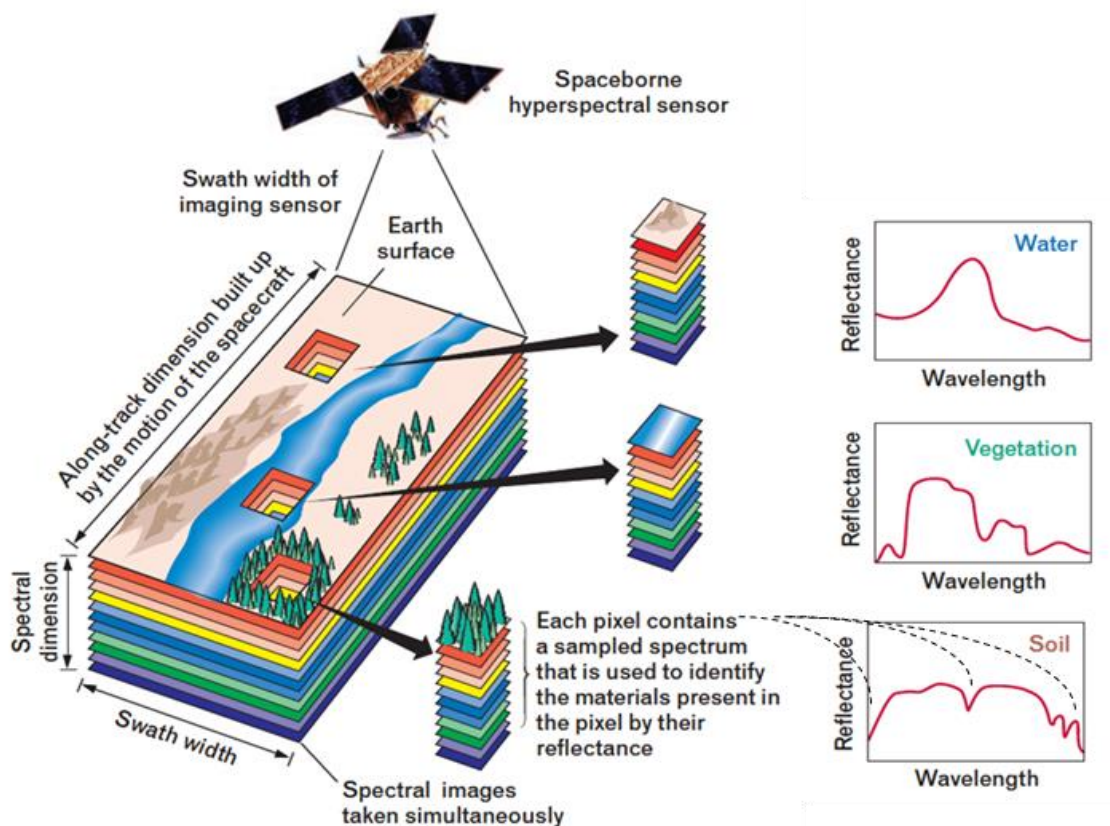


Remote Sensing

- a Tool for Environmental Observations -



Department of Physical Geography
Faculty of Geosciences
Utrecht University, The Netherlands
November 2015

Steven M. de Jong (Ed.)
Elisabeth Addink
Fionna Heuff



Preface

These lecture notes are part of the bachelor course ‘Aardobservatie en Data-analyse’ (GEO2-4208) and for the master course Remote Sensing (GEO4-4408) for students in earth sciences and environmental sciences at the Faculty of Geosciences, Utrecht University. Students from outside the faculty or university are also most welcome to attend to the course. Basic knowledge of surveying techniques in geography, basic knowledge of physics and mathematics and some computer skills are expected from the students. The course is an introductory course to the concepts, physics and basic processing of earth observation images and to basic data analysis. Emphasis is put on land use and land cover mapping, soils, geology and geomorphology. We will use images acquired by satellite sensors such as IKONOS, SPOT-XS, Landsat and, ASTER, Sentinel and airborne sensors such as DAIS7915 and HyMap. Remote sensing techniques are increasingly used in environmental studies for data acquisition e.g. land cover mapping, water quality control, water balance studies, soil erosion studies, climate change etc. Consequently, it is important for students in disciplines concerned with the environment to have some basic knowledge of Remote Sensing.

The objective of these lecture notes is to provide an overview of Remote Sensing techniques as a tool for environmental studies for students with a limited knowledge and little experience with Remote Sensing. The notes present an overview of currently available sensors aboard satellites and/or aircrafts (space borne and airborne sensors), it presents image pre-processing and image correction methods, procedures for image analysis and image interpretation techniques using a wide range of examples. Furthermore, it gives practical directions, literature sources and internet links for students who wish to enlarge their knowledge in the field of Remote Sensing and related topics.

The courses comprises next to a series of lectures a number of practical computer exercises. The exercises range from the interpretation of analogue photos to the processing of satellite images in optical and microwave wavelengths (Landsat, ERS imagery, Radar images acquired by ERS and SeaSATetc.). The software used during the practical exercises is Erdas/Imagine for the Bachelor course and IDL/Envi for the Master course. The exercises introduce image correction and analysis methods, procedures for land cover classification, image ratioing, digital filtering, multivariate analysis of imagery and more advanced techniques like linear spectral unmixing and spectral angle mapping in the master course.

The lecture notes should be used as a reference during the practical computer exercises and are helpful for the students to prepare for the final exam.

All the latest information about the remote sensing course , the digital full-colour copies of the lecture notes and exercises and some other information are available on BlackBoard.

Elisabeth Addink & Steven de Jong

Contents

Preface

1.	Introduction	4
1.1	A Remote Sensing System.....	4
1.2	The electromagnetic spectrum	5
1.3	Sources of electromagnetic energy	7
1.4	Atmospheric transmission	8
1.5	Interactions mechanisms with the earth surface	11
1.6	Sensors and scanners.....	14
1.7	Colour technology.....	18
2.	Multi-spectral Scanning	21
2.1	Introduction	21
2.2	Meteorological Satellites and their Sensors	21
2.3	Earth Resources Satellites.....	23
2.4	Airborne Sensors.....	33
3.	Remote Sensing in the Microwave Region (RADAR)	37
3.1	Introduction	37
3.2	Principle of a Radar System	37
3.4	Spatial Resolution	39
3.5	SAR: Synthetic Aperture Radar	41
3.6	Geometry of Radar Images	43
3.7	Radar Return and Image Signatures	45
3.8	Radar Satellites	48
3.9	RADAR Interferometry	51
3.10	Other satellites: GOCE & GRACE	53
4.	Thermal Infrared Remote Sensing	56
4.1	Introduction	56
4.2	Temperature and Emissivity	56
4.3	Heat transfer	56
4.4	Thermal properties of Materials.....	59
4.5	Thermal sensors.....	60
4.6	Heat Capacity Mapping Mission: HCMM	61
4.7	Interpretation of thermal infrared images	61
5.	Image Corrections and Analysis Techniques.....	63
5.1	Introduction	63
5.2	Digital Image Structure	63
5.3	Radiometric Corrections	65

5.4 Geometric Corrections.....	69
5.5 Image Enhancement	72
5.6 Digital Image Filtering	72
5.7 Spectral Ratioing	75
5.8 Digital Image Transformation	77
5.9 Image classification.....	79
 6. Image Interpretation.....	86
6.1 Introduction	86
6.2 Spectral Behaviour of Vegetation	86
6.3 Spectral Behaviour of Soils.....	89
6.4 Multi-temporal Remote Sensing & Change Detection	92
6.5 Imaging Spectroscopy	94
6.6 Remote Sensing projects in the Netherlands	96
 7. Remote Sensing Software and Geographical Information Systems	99
7.1 Introduction	99
7.2 Remote Sensing Software	99
7.2 Data Integration Issues	100
7.3 Modelling Spatial Processes in a GIS using Remote Sensing Data.....	100
 Information sources and important addresses:	103
 References and further reading:.....	105

1. Introduction

Remote sensing is a technique to observe the earth surface or the atmosphere from out of space using satellites (space borne) or from the air using aircrafts (airborne). Remote sensing is also called ‘earth observation’ or ‘teledetection’. Remote sensing uses a part or several parts of the electromagnetic spectrum. It registers reflected or emitted radiation. Remote sensing techniques enable us to study objects without being in touch with that object or without interfering with the object. Hence, remote sensing leaves the object undisturbed while observing, that is one of the major advantages of remote sensing compared to laboratory analyses or field experiments. Figure 1.1 illustrates the principle of data acquisition and data analysis using electromagnetic sensing of the surface of the earth.

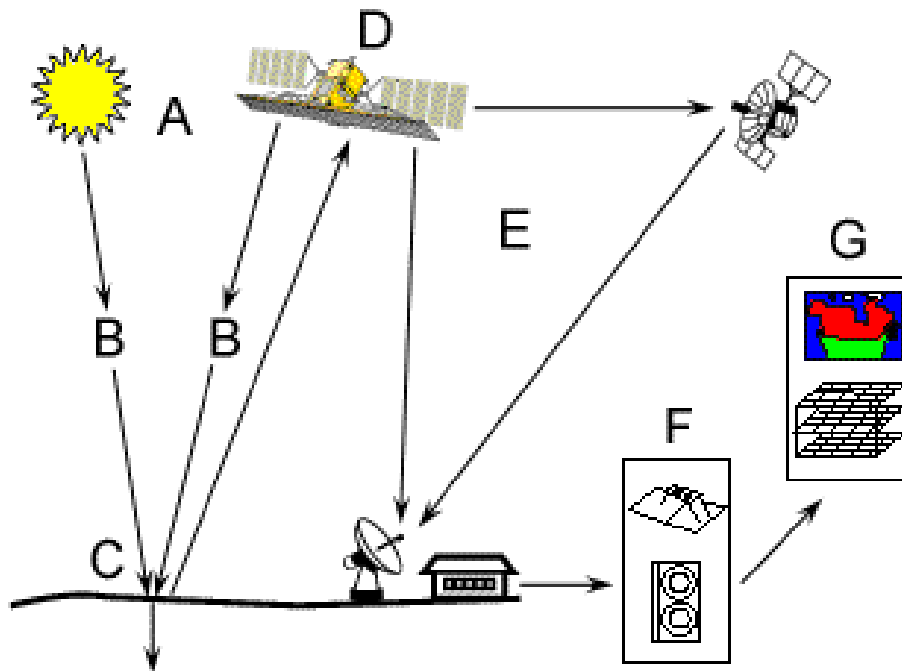


Figure 1.1: A system for electromagnetic Remote Sensing of the Earth including communication facilities.

1.1 A Remote Sensing System

A remote sensing system using electromagnetic energy consists basically of four components:

1. **A source of electromagnetic energy**, this is most often the sun’s reflected energy by the surface of the studied object or the emitted heat by the earth itself, or it is an artificial man-made source of energy such as microwave radar.
2. **Atmospheric interaction**, electromagnetic energy passing through the atmosphere (sun to earth’s surface and earth’s surface to the sensor) is distorted, absorbed and scattered.
3. **Earth’s surface interaction**, the intensity and characteristics of electromagnetic radiation reflected from or emitted by the earth’s surface is a function of the characteristics of the objects at the surface and a function of wavelength.
4. **The sensor**, a man-made sensor is used to register emitted or reflected electromagnetic energy (camera, radiometer, CCD). The characteristics and the quality of the sensor determine how well the radiation can be recorded.

This schematic representation of a Remote Sensing system should be kept in mind and will be helpful to understand the later discussions of the performance of certain remote sensing systems.

The source of energy utilized for remote sensing observation is used to divide remote sensing systems into passive and active systems:

A passive remote sensing system observes the radiation reflected by the object of interest. The energy source of such a system is most often the sun. Examples of passive remote sensing systems are the sensors aboard the Landsat satellites and the SPOT satellites.

Active remote sensing systems combine the energy source and the sensor. The artificial energy source emits electromagnetic energy in specific wavelengths towards the object and the sensor registers the reflected radiation. Especially radar systems, such as the Sideways Looking Airborne Radar (SLAR) and SAR (Synthetic Aperture Radar) are most often active systems. Another well-known example of an active remote sensing system is a photo camera with a flash. Figure 1.2 shows the components of an active and passive remote sensing system.

1.2 The electromagnetic spectrum

The link between the components of a remote sensing system is electromagnetic energy. Energy is usually transferred from one point to another by conduction, convection and radiation. In remote sensing we are primarily concerned with energy transfer by means of *radiation*: electromagnetic energy refers to all energy that moves with the velocity of light in a harmonic wave pattern.

The wave concept explains how electromagnetic energy propagates or moves. However, this energy can only be detected as it interacts with matter. In this interaction, electromagnetic energy behaves as though it consists of many individual bodies (*photons*) that have particle-like properties such as energy and momentum (Sabins, 1987). When light bends or refracts as it goes from one medium into another it behaves like a wave. When a radiometer measures the intensity of light, the photons produce an electric signal proportional to the number of photons.

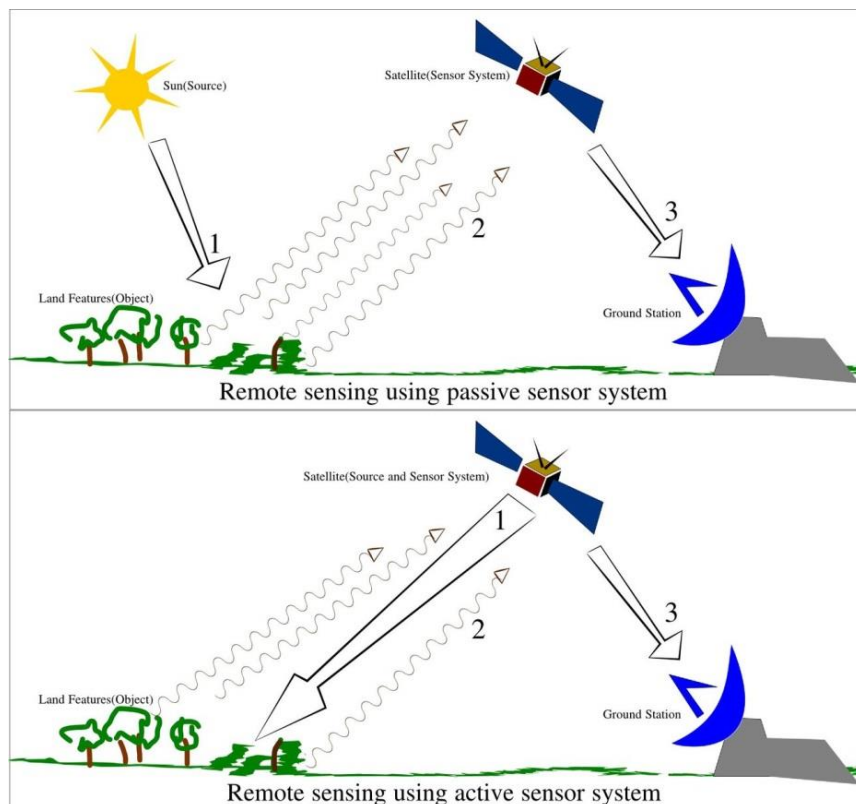


Figure 1.2: The four components of a Remote Sensing system (active and passive): the source of radiation, the atmosphere, the Earth surface or objects and the sensor (Wikipedia).

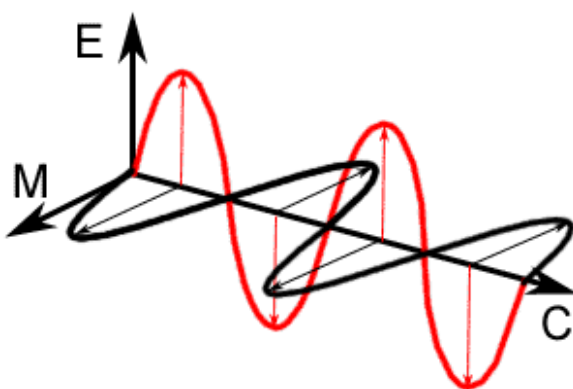


Figure 1.3: Electromagnetic radiation (or light) can be represented as waves.

Three measurements are used to describe electromagnetic waves:

- **wavelength** (λ in micrometer: μm or nanometres: nm , $1\mu\text{m}=1000\text{nm}$) which is the distance between the successive wave peaks;
- **frequency** (v in Hertz: Hz) which is the number the number of wave peaks passing a fixed point per unit time;
- **velocity** (c in m/s) which is a constant (speed of light: $3 \times 10^8 \text{ m/s}$).

The electromagnetic spectrum categorizes electromagnetic waves by their wavelengths (figure 1.3). The most important wavelengths for remote sensing are:

- the **visible wavelengths**, an extremely small part of the spectrum divided in:

blue:	0.4 - 0.5 μm
green:	0.5 - 0.6 μm
red:	0.6 - 0.7 μm
- **near infrared:** 0.7 - 1.1 μm ;
- **short-wave infrared:** 1.1 - 2.5 μm ;
- **thermal infrared:** 3.0 - 14.0 μm ;
- **microwave region:** 10^3 - $10^6 \mu\text{m}$ or 1 mm to 1 m.

Most often names such as near infrared or microwave are assigned to parts of the spectrum for convenience. Use these names with care because they are not clearly defined with wavelengths. It is preferable to use nanometres (nm) or micrometres (μm) to indicate parts of the spectrum. Figure 1.4 shows the electromagnetic wavelengths categorized to wavelengths.

Velocity, wavelength and frequency are related by:

$$c = \lambda * f$$

The energy of the wavelength (the photon model) is used to describe the energy of the radiation:

$$Q = h * f \text{ or } Q = \frac{(h*c)}{f}$$

Q : Energy of a photon (Joules:J)

h : Planck's constant $6.626 \times 10^{-34} \text{ J sec}$

v : frequency

λ : wavelength (μm)

c : velocity of light ($3 \times 10^8 \text{ m/s}$)

From these formulae it can be seen that the energy of a photon is inversely proportional to its wavelength: the longer the wavelength involved, the lower its energy content.

1.3 Sources of electromagnetic energy

Every object with a temperature above absolute zero (0°K or -273°C) radiates energy. Apart from the most commonly used source of radiant energy, the sun, all terrestrial objects are also sources of radiation (although their energy content is much lower). The amount of energy emitted is mainly a function of the temperature of the object and is described by **the Stefan-Boltzmann law**:

$$W = \sigma * T^4$$

W : total radiated energy (Watts/m^2);

σ : Stefan-Boltzmann constant $5.67*10^{-8} \text{ W m}^{-2} \text{ K}^{-4}$;

T : absolute temperature ($^{\circ}\text{K}$) of the object.

Note the importance (power relation) of the temperature of the emitting object.

The Stefan-Boltzmann relation is only valid for so-called black bodies. A **blackbody** is an ideal material that absorbs all the radiant energy that strikes it. A blackbody is a physical abstraction because no object at the earth surface has an absorptivity of 1 and no object radiates the full amount of energy given in the Stefan-Boltzmann equation. Therefore, for real materials a property called emissivity (ε) has been defined as the ratio of the radiant flux of the real material and a blackbody. Remember that emissivity is wavelength dependent.

Wien's displacement law

The temperature of the object does not only determine the amount of energy radiated, but controls also the wavelength at which the maximum amount of energy is radiated, generally referred to as λ_{\max} .

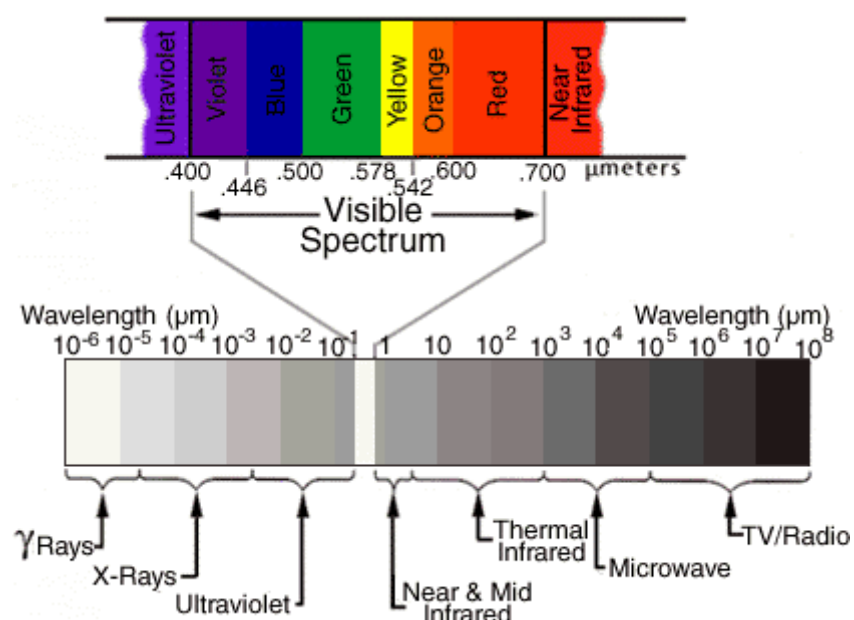


Figure 1.4: The electromagnetic spectrum. Note the logarithmic scale! (Lillesand & Kiefer, 1994).

Figure 1.5 shows radiant curves for objects ranging in temperature from 6000°K (the sun) to 200°K (the coldest objects at the surface of the earth). Hence, with increasing temperature the total amount of radiant energy increases and the radiant peak (λ_{max}) shifts to shorter wavelengths. This shift is described by **Wien's displacement law**:

$$\lambda_{max} = \frac{A}{T_{rad}}$$

A : constant 2897 $\mu\text{m} \cdot \text{K}$;

T_{rad} : radiant temperature °K.

This formula is useful to calculate the wavelength of the radiant energy peak of objects. For example, the temperature of the earth is approximately 300°K (27°C) and its λ_{max} is situated around 9.7 μm . Consequently, thermal infrared observations of the earth are carried out around 9.7 μm (thermal infrared region: 3-14 μm). Figure 1.5 shows the spectral distribution of energy radiated from a blackbody of various temperatures.

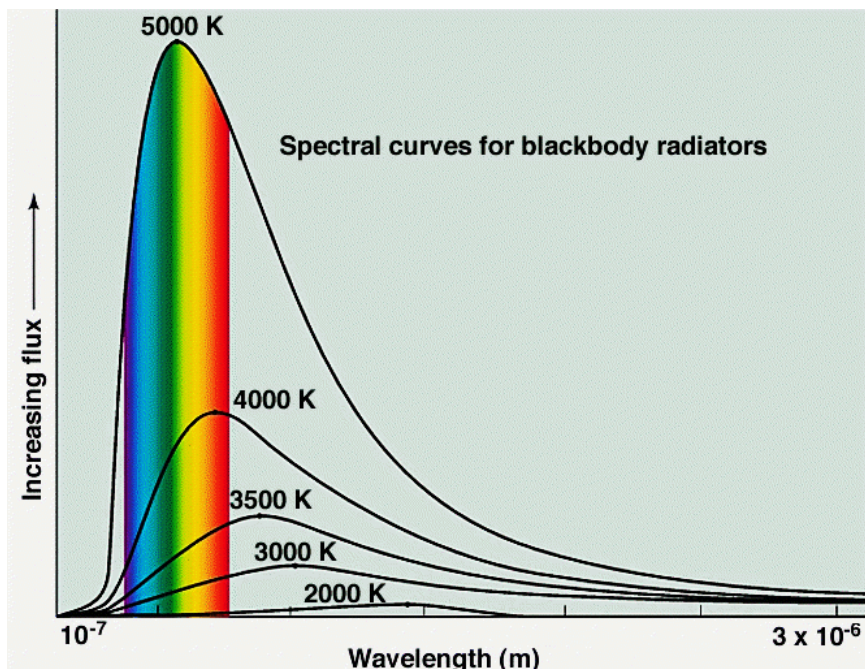


Figure 1.5: Spectral distribution of energy radiated from a blackbody of various temperatures according to the law of Stefan-Boltzman and the displacement law of Wien (<http://woodahl.physics.iupui.edu>).

1.4 Atmospheric transmission

Electromagnetic energy emitted by the sun must pass the atmosphere before it reaches the surface of the earth. A sensor aboard a satellite or aircraft measures reflected radiation which also has to pass the atmosphere or at least a part of the atmosphere. The distance radiation has to pass through the atmosphere is called **path length**. Unfortunately, the atmosphere is not completely transparent for radiation. Radiation is absorbed and scattered in the atmosphere. Absorption and scattering are both a function of wavelength and path length. Furthermore, they depend on the conditions in the atmosphere at the time of data acquisition. As the conditions of the atmosphere vary largely in space and time, it is very difficult to assess the exact effect of atmospheric distortion upon the sensed images. As a result it is also very difficult to correct images for these effects.

Absorption

The human eyes inform us that the atmosphere is essentially transparent to light. Therefore, it is often assumed that these conditions exist for all electromagnetic energy at any wavelength. However, the gases of the atmosphere absorb radiation at specific wavelengths: absorption bands (figure 1.6). Wavelengths shorter than 0.3 μm are completely absorbed, protecting us against lethal ultraviolet (UV) radiation. Water (H_2O) and hydroxyl (OH) absorb radiation in specific bands called the **water absorption bands**. The most important water absorption bands are located at 1.4 and 1.9 μm and around 3.1 and 6.2 μm . Minor water absorption bands are located at 0.9 and 2.6-2.8 μm . Other absorbing gases in the atmosphere are CO_2 and O_3 . Consequently, remote sensing observations are limited to the parts of the atmosphere that transmit radiation (table 1.1). These parts of the spectrum are called **atmospheric windows**. The most important atmospheric windows for remote sensing are:

Visible region:	0.4 - 0.7 μm
Infrared	0.7 - 2.5 μm
Thermal infrared	3.0 - 5.0 μm
Thermal infrared	8.0 - 14.0 μm
Microwave (radar)	0.01 - 1.0 m

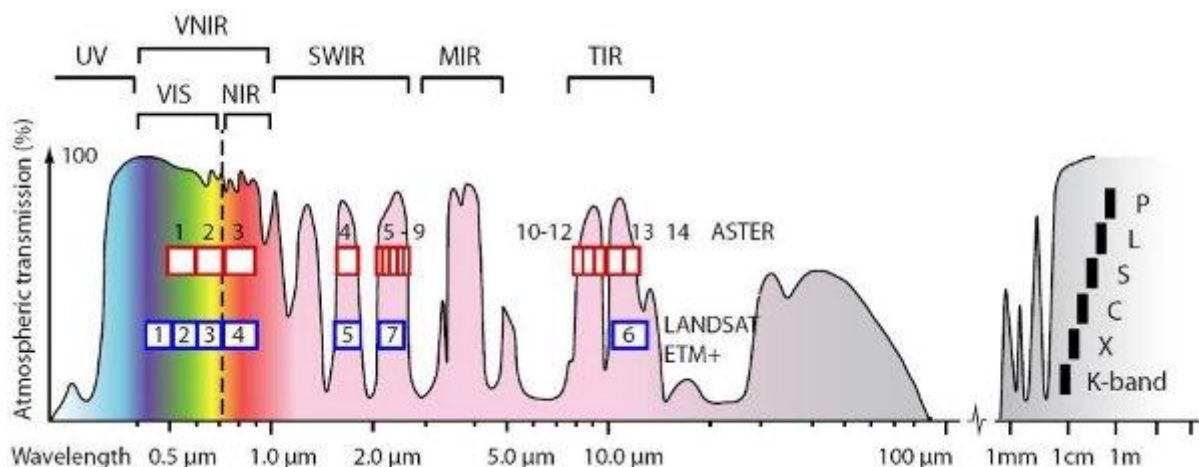


Figure 1.6: Atmospheric windows in the visible, infrared and microwave regions of the spectrum. Wavelengths bands of commonly used remote sensing systems are shown (www.intechopen.com/source/html/9531/image6.jpg).

Scattering

Atmospheric scattering results from interactions between radiation and gases and particles in the atmosphere (figure 1.7 and table 1.1). Two types of scattering are recognized: **selective scattering and non-selective scattering**. In non-selective scattering all wavelengths of light are equally scattered. Non-selective scattering is caused by particles (dust, clouds and fog) much larger than the energy wavelengths being sensed. Water droplets with a diameter of 5 to 100 μm cause for example non-selective scattering. In selective scattering, the shorter wavelengths of ultraviolet and blue are scattered more severely than the longer wavelengths. Selective scattering is caused by smoke, fumes and by gases such as nitrogen, oxygen and carbon dioxide. Examples of selective scattering are Rayleigh scatter and Mie scatter.

Rayleigh scatter is the most common type of scattering and affects the short visible wavelengths. It results in haze. Rayleigh scatter is caused by particles in the atmosphere much smaller than the

wavelength of radiation ($< 0.1\lambda$). A blue sky is a result of Rayleigh scatter. Various types of atmosphere and their degree of Rayleigh scatter are shown in figure 1.8.

Mie scatter is caused by particles in the atmosphere with the same size as the wavelength of radiation e.g. water vapour and dust.

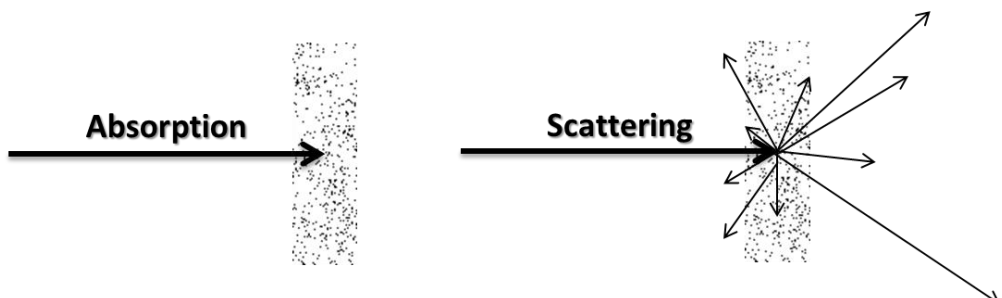


Figure 1.7: Atmospheric absorption and atmospheric scattering of electromagnetic radiance by particles in the atmosphere.

Table 1.1: Types of atmospheric scattering in order of importance (Curran, 1985).

Type of scatter	Size of effective atmospheric particles	Type of effective atmospheric particles	Scatter	Effect of scatter on visible and near visible wavelengths
Rayleigh	Smaller than the wavelength of radiation. Usually $< 0.1\lambda$.	Gas molecules	Molecule absorbs high energy radiation and re-emits. Scatter is inversely proportional to fourth power of wavelength.	Affects short visible wavelengths, resulting in haze in photography, skylights and blue skies
Mie	Same size as the wavelength of radiation	Spherical particles of water vapor, fumes and dust	Physical scattering under overcast skies	Affects long visible wavelengths
Non-selective	Larger than the wavelength of radiation	Water droplets and dust	Physical scattering by fog and clouds	Affects all visible wavelengths equally, resulting in white fog and clouds
Raman	Any	Any	Photon has elastic collision with molecule resulting in a loss or gain in energy; this can decrease or increase wavelength	Variable

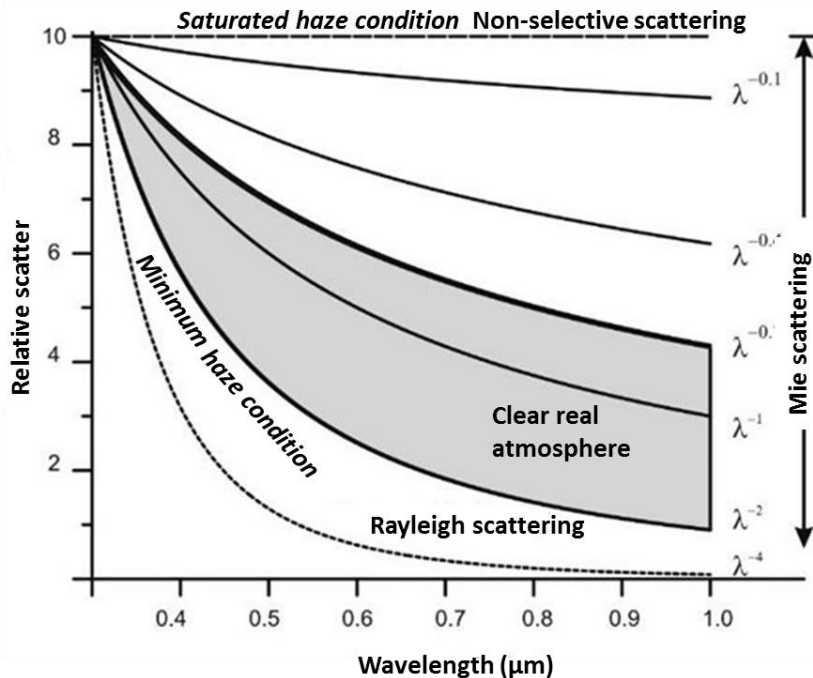


Figure 1.8: Relative scatter as a function of wavelength for various levels of atmospheric haze (Adapted from: Sabin, 1987).

1.5 Interactions mechanisms with the earth surface

Environmental researchers using remote sensing techniques are mainly interested in the interaction mechanisms between radiation and the objects at the surface of the earth (except of course when the atmosphere and its constituents are the research topic e.g. for ozone or CFK concentration or aerosol studies). Atmospheric interference makes things only difficult for people interested in land applications of remote sensing. Electromagnetic energy that encounters matter, whether solid, liquid or gas, is called **incident radiation**. Interactions with matter can change the following properties of the incident radiation:

- intensity;
- direction;
- wavelength;
- polarization;
- phase

The information of interest to the environmental researcher e.g. land cover, soil type, condition of the vegetation or crop or lithologic formation is deduced from these changes. Figure 1.9 shows the five most common results of radiation-matter interaction:

1. **transmission**, radiation is passed through the substance and very often refracted. Think of light coming from the air medium into water causing a change in velocity of the electromagnetic radiation: refraction.
2. **absorption**, the electromagnetic energy is absorbed by the matter and used to heat the object.
3. **emitted by the substance**, the electromagnetic energy is absorbed, used to heat the object and the object emits radiation according to the Stefan-Boltzmann equation.
4. **scattering**, the radiation is deflected in all directions. Surfaces with roughness comparable to the wavelength of the incident radiation cause scattering.

5. **reflection**, the incident radiation is returned from the surface with the angle of reflection equal and opposite to the angle of incidence. Reflection is caused by smooth surfaces relative to the wavelength. **Diffuse reflectors or Lambertian reflectors** are rough surfaces that reflect uniformly in all directions. **Specular reflectors** are flat surfaces that act like a mirror (angle of reflection = angle of incidence). Most earth surfaces are neither perfectly specular nor diffuse reflectors but act somewhat between these two extremes (figure 1.10). Direction of vibration or **polarization** may differ from the incident wave.

In Remote Sensing, the differences between diffuse reflectance of objects are most often measured and interpreted. Differences of reflection by objects in the visible wavelength give the human eye the sense of colour.

Do not confuse albedo and spectral reflectance. **Albedo** is the ratio of the total amount of electromagnetic energy reflected by a surface to the amount of energy incident upon it, most often in the spectral interval of 0.4 to 2.5 μm . **Spectral reflection** is the ratio of radiant energy reflected by a surface to the energy incident on it in a specific spectral interval e.g. the visible green: 0.5-0.6 μm . Reflectance is often used for both. Be always aware of the spectral region used.

This chapter shows that it is rather expensive and a bit cumbersome to make spectral wavelengths visible for the human eye, which are normally not visible e.g. infrared and thermal infrared. The motivation for all these efforts is that many objects at the earth surface have a very different spectral behaviour outside the visible wavelengths. Information on the condition of vegetation and soils can much better be derived from spectral measurements in near infrared and short-wave infrared than from spectral data in the visible wavelengths. Figure 1.11 shows an example for vegetation. The differences of the spectral reflection curves of deciduous trees and coniferous trees are much larger in the near-infrared than in the visible part of the spectrum. The same is true for crops, soils and rock formation in specific parts of the spectrum as will be discussed in the following chapters.

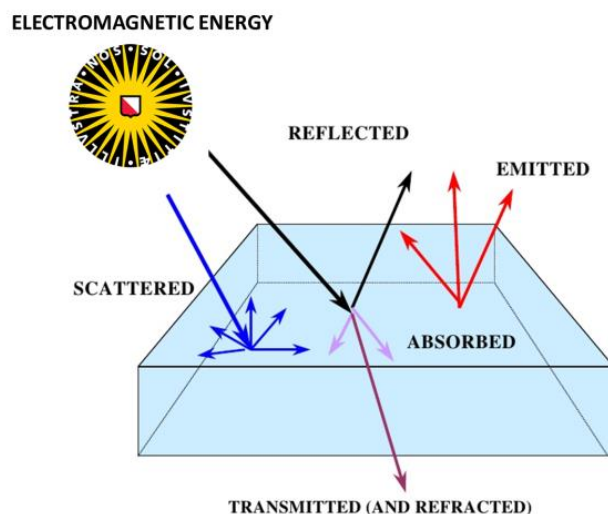


Figure 1.9a: Interaction mechanisms between electromagnetic energy and matter (*Adapted from: Jenkins, J. on www.slidesharecdn.net*).

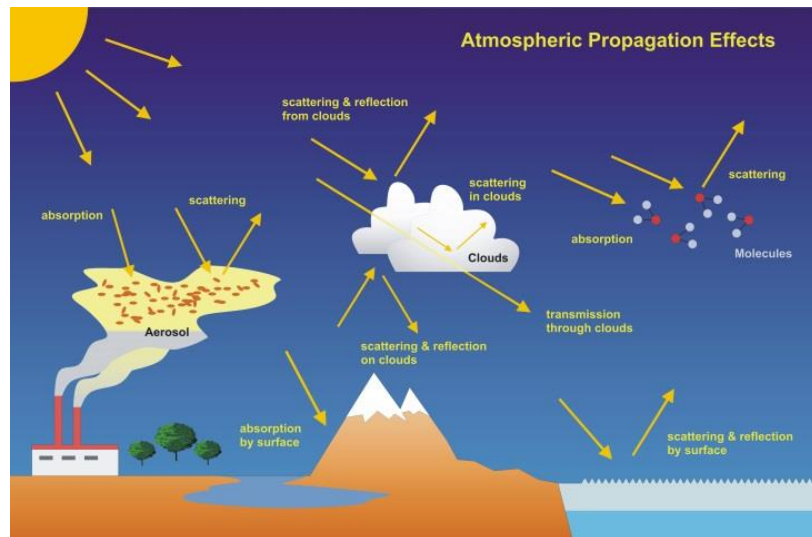


Figure 1.10b: Illustration of the more complex interaction between electromagnetic radiation, the atmosphere and the Earth's surface (<http://atmos.caf.dlr.de/>).

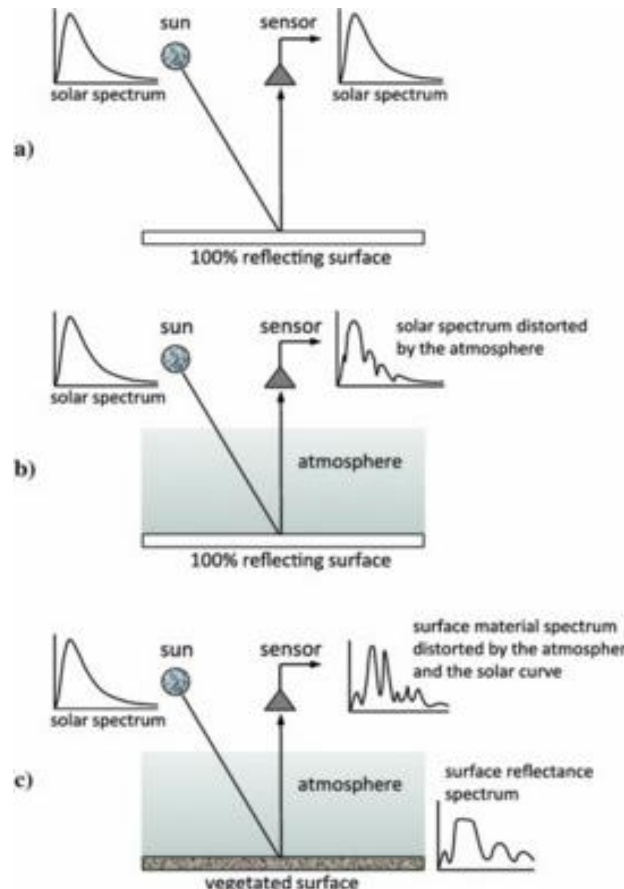


Figure 1.11c: Distortion of surface material reflectance spectrum by the atmosphere with a) detection of the solar curve from a perfectly reflecting surface in the absence of the atmosphere, b) the effect of the atmosphere on detecting the solar curve, c) detection of the real spectrum distorted by the atmosphere and the solar curve (Richards, 2012).

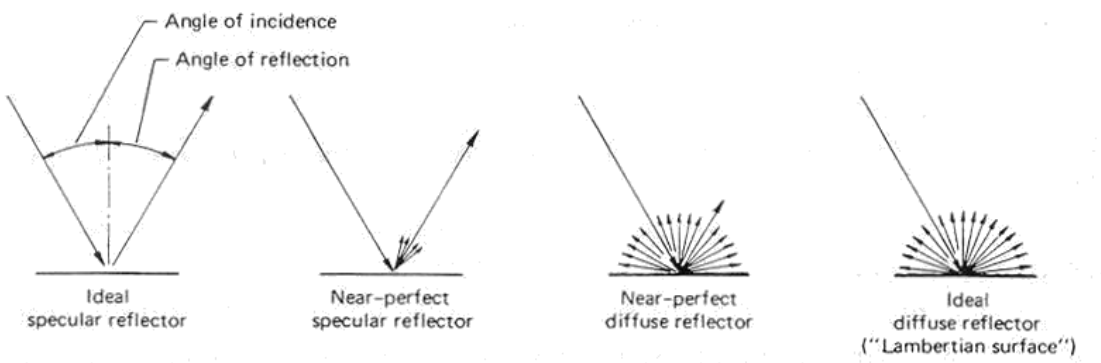


Figure 1.12: Specular and diffuse reflectors (Lillesand & Kiefer, 1994).

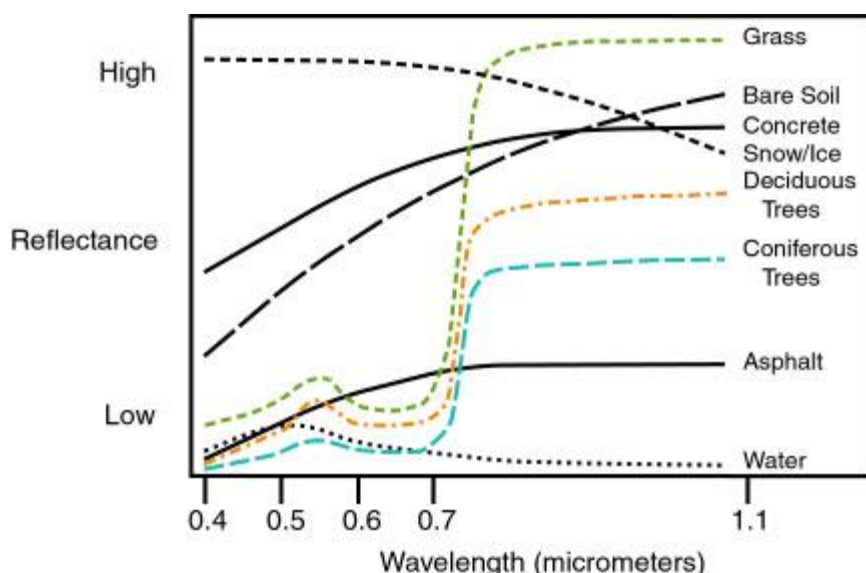


Figure 1.13: Spectral reflectance curves for vegetation and a number of other objects (www.ccpo.odu.edu).

1.6 Sensors and scanners

The most well-known type of remote sensing system is the photo camera. The reflected radiation is directly registered on film. However, photographic systems are limited to visible and near infrared spectral range 0.3 to 0.9 μm . Electronic detectors are required to measure radiation outside this range; they extend the potential range of sensing from approximately 0.3 to 14 μm .

Sensors

Sensors are tools for indirect image registration in contrast to the conventional camera. A sensor or detector is a device that receives electromagnetic radiation, converts it into a (electric) signal and presents it in a form suitable for obtaining environmental information (Curran, 1985). This suitable form is most often a digital format, the intensity of the radiation is expressed in the classes available in a byte or word. This largely facilitates computer processing of sensor-derived information.

Some knowledge about the technical operation of a sensor and scanner is important because the airborne or space borne images are sometimes affected by the performance of the system. Patterns or lines in the images caused by the sensor should not be misinterpreted by the environmentalist.

Scanners

A **scanner** or a scanning system employs a detector with a narrow field of view which sweeps across the terrain, the parallel scan lines are combined together to produce an image. There are four common methods of scanning (figure 1.12):

- cross-track scanner;
- circular scanner;
- along-track scanner;
- side scanning system.

The most widely used scanner is the cross-track scanning system. A faceted mirror is horizontally rotated by an electric motor. Constructing images by line scanning relies on the forward motion of the platform (satellite or aircraft) carrying the device. The dimensions of the ground resolution cell (or pixel) are determined by the detector instantaneous field of view IFOV (the field of view of the detector at one moment) and the altitude of the scanning system. The along-track scanner does not use a mirror, instead it has an individual detector for each ground resolution cell across the ground swath. The side-scanning system is mostly an active system, which provide its own energy source, and is used for radar or microwave systems. A more extensive description of scanners can be found in Lillesand and Kiefer (1994) or Sabins (1987).

Multi-spectral scanner

The previous described systems record basically a single image that represents a single spectral band (one single portion of the entire spectrum). For many remote sensing applications, it is necessary to record a scene with multi-spectral images (multiple images showing different parts of the spectrum). The basic principle of a multi-spectral scanner is the same as for one cross-track scanners (figure 1.13):

1. A telescope directs the radiation onto the rotating mirror.
2. The rotating mirror (powered by an electric motor) reflects the radiation passing through the telescope into the optics (the mirror is set at an angle of 45° which allows it to scan the terrain from side to side).
3. The optics focus the radiation into a narrow beam.
4. A refracting grid splits the narrow beam into its reflected and emitted components. The emitted radiation goes directly to the thermal infrared detectors.
5. A prism is placed in the path of the reflected radiation to divide it into its spectral components.
6. The detectors sense the radiation, then the signal is amplified and passed in electronic form to a device to store the data (tape unit, hard disk etc.).

Most multi-spectral scanning systems scan multiple lines at a time (e.g. 6 lines for the Landsat MSS and 16 lines for the Landsat TM).

Remote Sensing Systems Used to Collect Aerial Photography, Multispectral and Hyperspectral Imagery

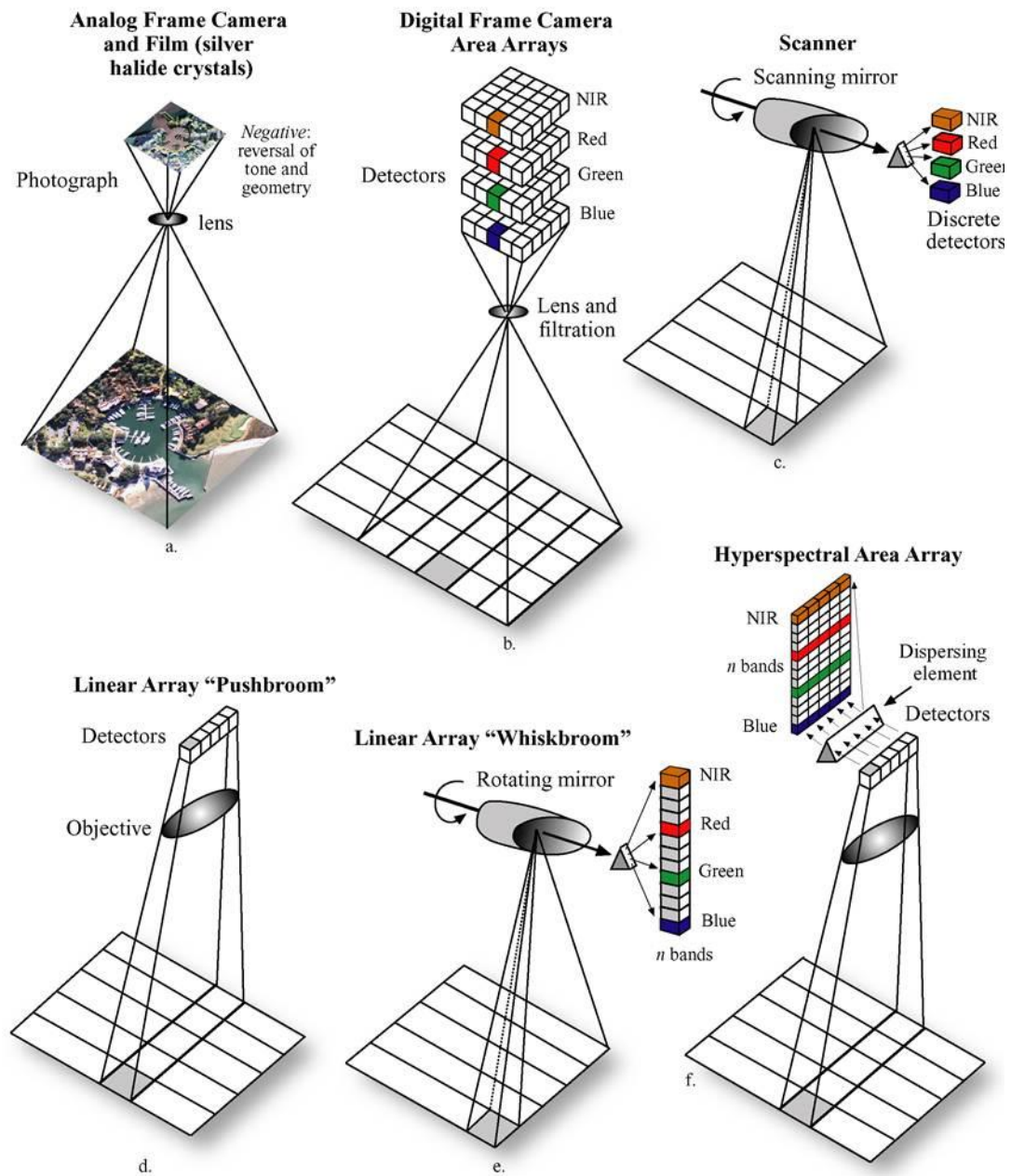


Figure 1.14: Scanning systems for acquiring remote sensing images (www.e-education.psu.edu)

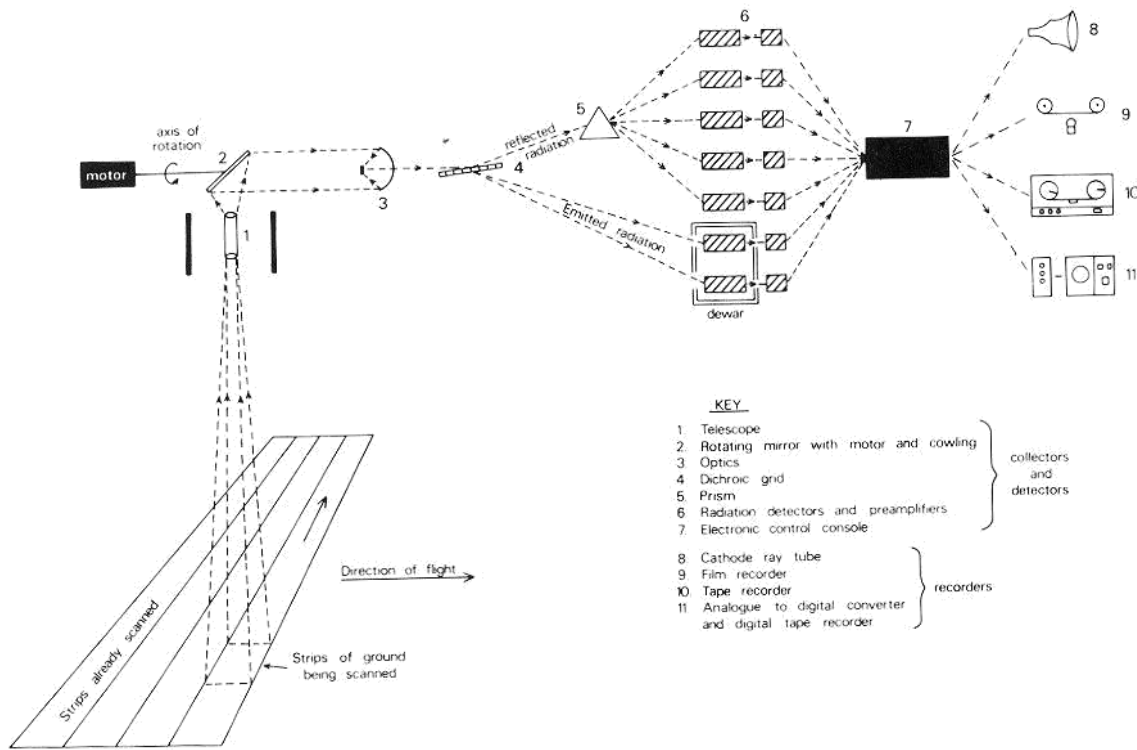


Figure 1.15: Diagrammatic representation of a multi-spectral scanner (Curran, 1985).

The construction and the technical performance of a remote sensing system determines whether objects can be detected and/or identified in an image. Detectability is the ability of an imaging system to record the presence or absence of an object. Recognisability is the ability to identify an object, the latter requires a skilled interpreter. Hence, the design of a remote sensing system is a complex task and a balance has to be found between the following points:

- the spectral resolution, the band width or spectral regions of the sensors aboard the system;
- the radiometric resolution or intensity resolution, the range of reflectance values that must be registered and the number of grey levels that must be distinguished.
- photometric accuracy, the sensitivity of the sensors should be the same (or at least comparable) in all wavelengths;
- spatial resolution, the pixel size (pixel = acronym for picture element) should match with the size of the objects to be detected.
- geometric accuracy, the image should have the least possible systematic and stochastic geometric distortions.
- temporal resolution, the frequency of image acquisition should match with the temporal changes of the objects of interest.

Apart from the above-mentioned considerations, the following points are important: the position of the atmospheric windows and the spectral region in which the source of electromagnetic energy emits.

1.7 Colour technology

The first reconnaissance or the interpretation of remote sensing images is most often performed with the human eye. Apart from grey tones, texture and patterns, colour and colour patterns play an important role in the interpretation. Therefore, it is important to have some knowledge of colour, mixing of colours and colour film technology. The average human eye can discriminate many more shades of colour than it can tones of grey. Hence, the use of colour increases the interpretability of images greatly.

The colours seen by the human eye are in fact described by three variables (or dimensions). The Munsell colour scale specifies colours based on value, hue, and chroma. In Remote Sensing we use the same approach, but with a slightly different naming convention: intensity, hue and saturation (IHS):

- **Intensity** (value) relates to the total brightness of a colour (amplitude of the wave);
- **Hue**, or colour tone, refers to the dominant or average wavelength of light contributing to a colour (frequency);
- **Saturation** (chroma) specifies the purity of the colour.

Hence, a three dimensional space (international colour cone) is required to describe these three variables (figure 1.14). Image processing normally uses additive colours like in televisions.

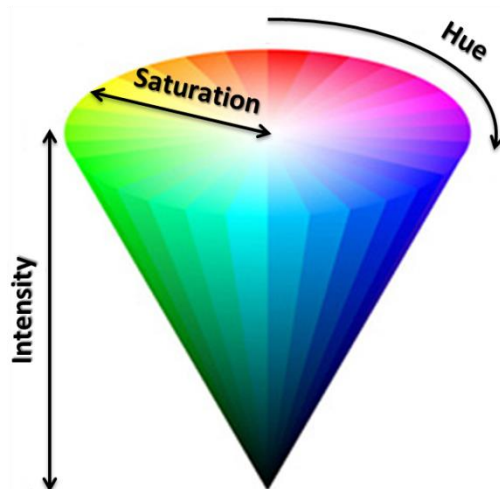


Figure 1.16: A three dimensional space is required to described colour in RS. The Munsell colour systems uses value and chroma instead of intensity and hue respectively (Adapted from: <http://www.tomjewett.com/>)

Additive primary colours

The visible part (0.4-0.7 µm) of the spectrum can be divided into six gradational colours: violet, blue, green, yellow, orange and red. Almost all colours can be synthesized by adding different portions of **blue, green and red**. These are called the **three additive primary colours** because synthetic white light forms when equal amounts of blue, green and red are superimposed. The range of each additive primary colour spans one-third of the visible spectrum. A colour image can be produced by adding these three primary colours on a television screen or computer monitor.

Subtractive primary colours

Colours on e.g. film can also be produced by subtracting specific parts of the spectrum. In order to mix colours for films, the **three subtractive primary colours** must be used: **yellow, magenta and cyan**.

Colour films

Colour prints are colour photographs with an opaque base. Colour film is a transparent medium that may be either positive or negative. On conventional negative film, the colour present is complementary (!) to the colour of the object photographed and the density on the film is the inverse of the brightness of the object.

Colour negative films consist of a transparent base coated with three emulsion layers (figure 1.15). Each layer is sensitive to one of the additive primary colours: blue, green or red. During developing of the film, each emulsion layer forms a colour dye that is complementary to the primary colour that exposed the layer: the blue-sensitive emulsion layer forms a yellow negative image, the green-sensitive layer forms a magenta negative layer and the red-sensitive layer forms a cyan negative layer. A more comprehensive description of colour film technology is given by Lillesand et al. (2015).

Colour infrared film (CIR)

The spectral sensitivity of the three layers of colour emulsion on a film may be changed to register the electromagnetic energy of other wavelengths than the visible ones. A shift of the wavelengths towards the near infrared is most widely used. Such a film is called IR colour film or false colour film. It was designed for military purposes and hence it was earlier called camouflage detection film. The sensitivity of the film is shifted as follows: the blue-imaging layer is exposed by green light, the green-imaging layer is exposed by red light and the red-imaging layer is exposed by reflected near infrared. Hence, a false colour film is not sensitive for thermal infrared!

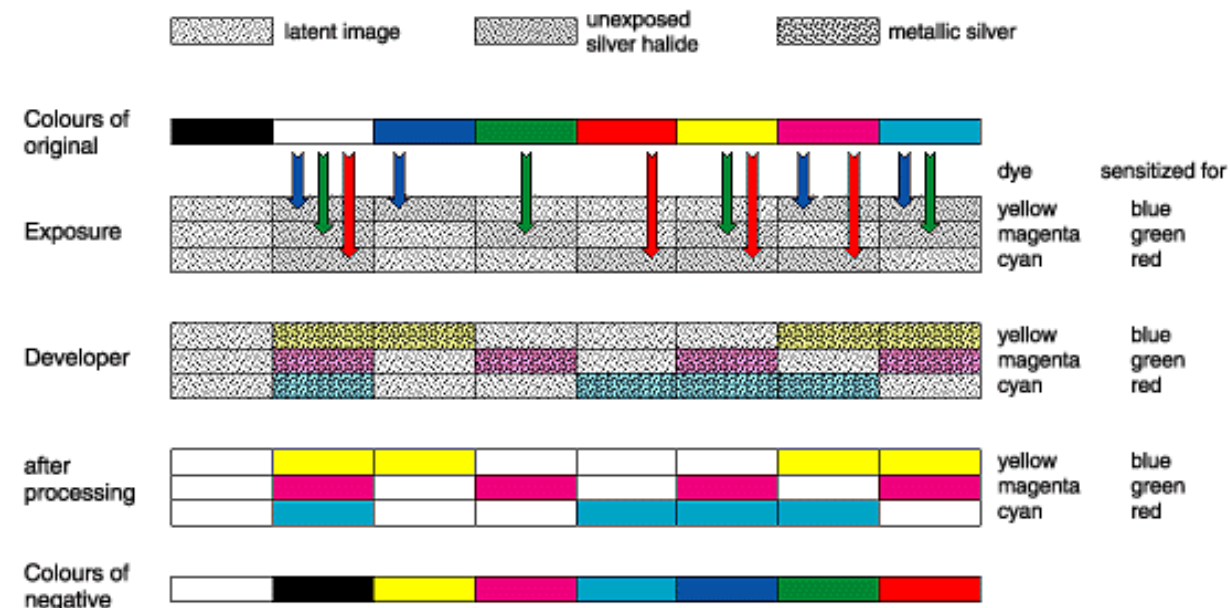


Figure 1.17: Colour formation on IR colour film (Lillesand & Kiefer, 1994).

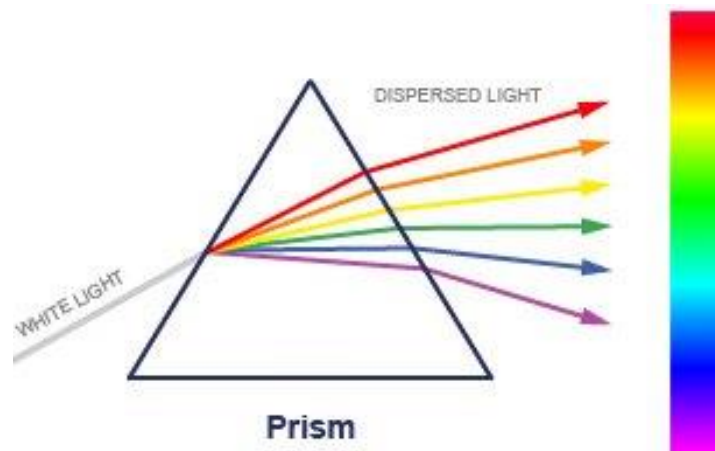


Figure 1.18: A prism is used to split white light into its individual components (www.epicphysics.com).

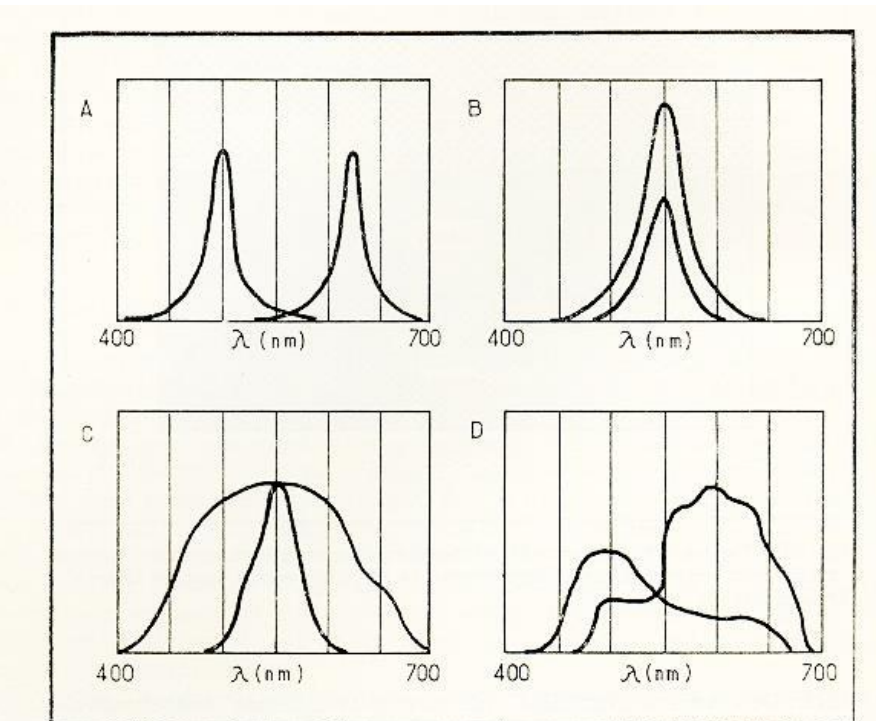


Figure 1.19: Illustration of how A) wavelength (hue), B) intensity and C) saturation of colour interact and D) mix colours.

2. Multi-spectral Scanning

2.1 Introduction

A multi-spectral scanner is an airborne or space borne remote sensing system that simultaneously acquires images of the same scene at different wavelengths. The **field of view (FOV)** is the solid angle through which an instrument is sensitive to radiation. The sensors of a multi-spectral scanner are normally working in specific parts of the spectral range from 0.35 up to 14 μm . These specific parts of the spectrum in which remote sensing observation are made, are called bands or channels.

The reflected radiation (0.3-2.5 μm) is usually detected by silicon photodiodes that are placed in the correct geometric position behind the prism. The emitted thermal infrared radiation is normally detected by photon detectors, manufactured from mercury doped germanium (Ge:Hg) which is sensitive to wavelengths from 3 to 14 μm , or they are manufactured from indium antimonide (InSb) which is sensitive for the spectral range from 3 to 5 μm , or they are made from mercury cadmium telluride (MCT or HgCdTe) which is sensitive from 8 to 14 μm . The electric signal produced by these photon detectors is theoretically proportional to the radiation energy in the selected spectral band. However, calibration of the signal is always necessary. The number of bands or channels varies largely from system to system.

Two important advantages of multi-spectral scanning are:

- Objects at the surface of the earth have varying reflection behaviour through the optical spectrum, they can be recognized and/or identified more easily using several spectral bands than using just one band.
- A large number of objects do not reflect radiation very well in the visible part of the spectrum. Remote sensing observations outside the visible wavelengths or in combination with observations in the visible spectrum produce a much more contrasting image, which is helpful to identify objects or to determine their condition.

2.2 Meteorological Satellites and their Sensors

NOAA-AVHRR

The first satellite for remote sensing observations was launched in 1960 and was called TIROS: Television and Infrared Observation Satellite. It was developed for meteorological purposes by the National Oceanic and Atmospheric Administration (NOAA) of the USA. This early weather satellite sent down rather coarse views of cloud patterns. NOAA refined the sensors and the orbits of TIROS and has continued and will continue to launch weather satellites. One of their most famous series of satellites among environmentalists is the NOAA-AVHRR (NOAA-AVHRR 12 was launched on 14 may 1991). AVHRR stands for Advanced Very High Resolution Radiometer and was also built for meteorological observation. It has a near-polar, sun-synchronous orbit at an altitude of approximately 830 k. Due to its large field of view, its spatial resolution is low (i.e. its pixel size is large: $\pm 1.1 \text{ k}$). Lillesand & Kiefer (1994), page 502 and colour plate 16, 17 and 18 show examples of NOAA-AVHRR images. It has the following five spectral bands:

NOAA-AVHRR Band	Bandwidth (μm)	Orbit
1	0.58 - 0.68	Altitude: 830 km Orbit incl.: 98.9° Repeat time: 1 day IFOV: $\pm 1.1 \text{ km}$
2	0.72 - 1.10	
3	3.55 - 3.93	
4	10.5 - 11.5	
5	11.5 - 12.5	

NOAA-AVHRR are used by environmentalists to monitor changes in vegetation cover at a continental scale e.g. Tucker et al. (1986) and Tucker et al. (1984). NOAA-AVHRR data are also used for the ARTEMIS project (the Africa Real Time Environmental Modelling using Imaging Systems). This project of the Food and Agricultural organization (FAO) was funded by the Netherlands and aims at supplying a continuous, real-time overview of the ecological conditions of the African continent. This enables planners to avoid famine due to bad harvests. The point of contact in the Netherlands to obtain NOAA images is the KNMI at de Bilt.

NIMBUS

The NIMBUS satellite, the first NIMBUS was launched in 1964 and NIMBUS-7 was put in orbit in 1978, was developed by NASA for meteorological and oceanographic research: measuring sea water temperature, to map phytoplankton concentration and suspended materials. The sensor aboard NIMBUS is the Coastal Zone Colour Scanner CZCS:

NIMBUS-CZCS Band	Bandwidth (μm)	Orbit
1	0.43 - 0.45	Altitude: 910 km Orbit incl.: $\pm 98^\circ$ IFOV: $\pm 800 \text{ m}$
2	0.51 - 0.53	
3	0.54 - 0.56	
4	0.66 - 0.68	
5	0.70 - 0.80	
6	10.5 - 12.5	

Meteosat

This satellite is operated by the European Space Agency (ESA) and is located on a fixed position above the Greenwich Meridian over West Africa. Such an orbit is called a **geostationary orbit**: it is an orbit at an altitude of 35.786 km in the equatorial plane, which matches speed so that a satellite remains over a fixed point on the earth's surface. Meteosat-1 was launched in November 1977. The Meteosat record images every 30 minutes in three wavelengths in visible and near-infrared, in the water vapour absorption region and in the thermal infrared.

The meteosat images are probably very familiar to you because they are shown almost every evening during the weather forecast on television. Due to their poor spatial resolution, environmentalists rarely use the meteosat images. You can visit <http://weather.msfc.nasa.gov/GOES/> for various GOES images.

Meteosat Band	Bandwidth (μm)	Orbit
1	0.4 - 1.1	Altitude: 35.786 km Geostationary orbit Record image every 30 minutes Pixel size: 2.5 - 5.0 km
2	5.7 - 7.1	
3	10.5 - 12.5	

2.3 Earth Resources Satellites

The large number of remote sensing satellites is for most new-comers very confusing. The most important of these will be discussed in this section. They comprise the Landsat, SPOT, Pléiades and Sentinel series, ASTER, MODIS, NOAA-AVHRR, ERS, SMOS and SMAP. Important properties to know of these satellites are their orbit (geostationary or polar, altitude and/or pixel size) and the spectral positions of their sensors.

The Landsat program

The American Landsat series of satellites were developed within the 'Earth Resources Programme' of NASA in the early seventies. The first of eight Landsat satellites was launched on 22 July 1972. At that time it was called ERTS-1: Earth Resources Technology Satellite. Later on this name was changed into Landsat-1. This satellite was of great importance because it provided many, high quality beautiful images which gave remote sensing technology world-wide recognition. Over the years, 7 more satellites have been launched, but only 6 have been operational because Landsat 6 failed to reach orbit.

Landsat 8, launched in February 2013, is the youngest in the series and Landsat 9 is scheduled for 2023. Visit <http://landsat.gsfc.nasa.gov/> for all the information about the Landsat satellites and their data.

Figure 2.2. shows the Landsat 1-8, excluding 6, satellites, approximately the sizes of a small car.

The Landsat satellites are in a sun-synchronous orbit (figure 2.3) at an altitude of approximately 700 km and with an inclination of 98.2°. They require approximately 100 minutes to circle the earth and they have a repeat time of 16 days. This means that they make an image of the same area every 16 days. The sensors provide(d) images of 185 by 185 km. MSS provides images in 64 grey levels (6 bits), and TM and OLI send down images in 256 grey levels (8 bits).

The Landsat 1-5 satellites all carried aboard a multi-spectral scanning system MSS. Landsat 4-7 also had/have a Thematic Mapper (TM, and in the case of Landsat 7 ETM+), while Landsat 8 carries an Operational Land Imager (OLI) and Thermal Infrared Sensor (TIRS). Landsat 1,2 and 3 carried in addition a return beam vidicon (RBV) television camera. See the tables below for more detailed specifications. The TM was an improvement of the earlier MSS sensor, having more spectral bands and an increased spatial resolution.

The first 5 Landsat satellites were very successful. Unfortunately, the launching of Landsat-6 came to a bad end. Immediately after launch radio contact was lost and the satellite never reached its orbit (a loss of US \$220 million). Landsat 6 was extended with the ETM: the Enhanced Thematic Mapper. Apart from this ETM there was an eight band, a panchromatic channel (0.50 - 0.90 µm) with a spatial resolution of 15 m.

It took another 6 years before Landsat 7 with aboard the ETM+ sensor was launched on 15 April 1999. Landsat 7 ETM+ is the successor of the very successful Thematic Mapper (TM) instruments on Landsat 4 and 5. Landsat 7 is equipped with six bands in the visible to shortwave infrared with a

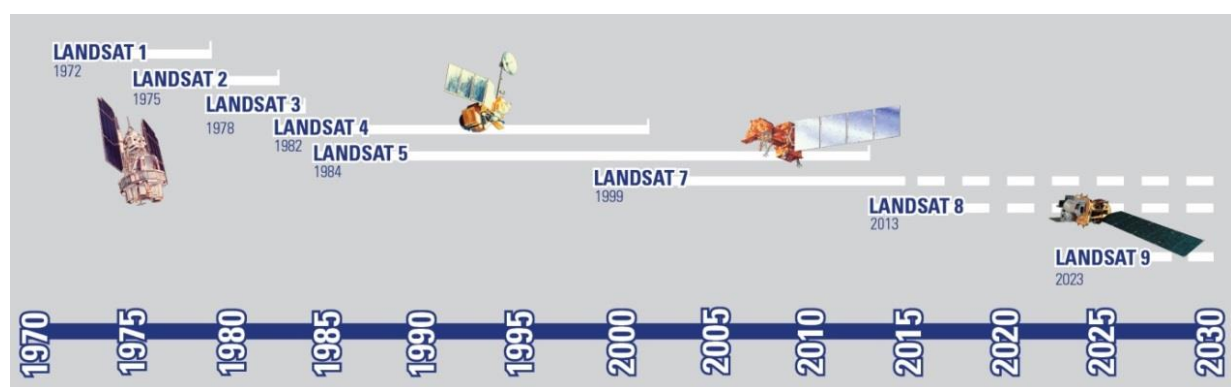


Figure 2.1: Timeline of the Landsat program (USGS.com).

resolution of 30m, one band in the thermal infrared with a resolution of 60m and with a panchromatic band with a resolution of 15m. A permanent instrument malfunction occurred on May 31, 2003. The problem was caused by failure of the Scan Line Corrector (SLC), which compensates for the forward motion of the satellite. Since then only limited useful data is acquired in "SLC-off" mode (LANDSAT, 2003).

Almost 14 years later, Landsat 8 was launched. The spectral bands of the OLI, while similar to Landsat 7's ETM+ sensor, provide enhancement from prior Landsat instruments, with the addition of two new spectral bands: a deep blue visible channel (band 1) specifically designed for water resources and coastal zone investigation, and a new infrared channel (band 9) for the detection of cirrus clouds. A new Quality Assurance band is also included with each data product. This provides information on the presence of features such as clouds, water, and snow. The TIRS instrument collects two spectral bands for the wavelength covered by a single band on the previous TM and ETM+ sensors (landsat.usgs.gov).

The data quality (signal to noise ratio) and radiometric quantization (12-bits) of the OLI and TIRS is higher than previous Landsat instruments (8-bit for TM and ETM+), providing significant improvement in the ability to detect changes on the Earth's surface. At least 400 scenes are collected daily, and placed into the USGS archive to become available for download within 24 hours after acquisition (landsat.usgs.gov).

Table 2.1 gives an overview of sensors and their spatial resolution aboard the Landsat satellites. Note the differences in pixel size.



Figure 2.2: From left to right and top to bottom: Landsat 1-8, excluding 6 (<http://landsat.gsfc.nasa.gov>).

Table 2.1: Landsat Sensor band characteristics (<http://landsat.gsfc.nasa.gov/>, landsat.usgs.gov).

	Band width (μm)						
Band	MSS	TM	ETM+	OLI/TIRS	Band	Application	Spatial Resolution (m)
				0.43 - 0.45	1	Ultra-Blue: Coastal/Aerosol	30
1	0.5-0.6	0.45-0.52	0.45-0.52	0.45 - 0.51	2	Blue	60/30*
2	0.6-0.7	0.52-0.60	0.52-0.60	0.53 - 0.59	3	Green	60/30*
3	0.7-0.8	0.63-0.69	0.63-0.69	0.64 - 0.67	4	Red	60/30*
4	0.8-1.1	0.76-0.90	0.77-0.90	0.85 - 0.88	5	NIR	60/30*
5	-	1.55-1.75	1.55-1.75	1.57 - 1.65	6	SWIR I	60/30*
		10.40-12.50	10.40-12.50	10.60 - 11.19	10	TIR	120/60/100**
6	-			11.50 - 12.51	11		
7	-	2.08-2.35	2.09-2.35	1.36 - 1.38	7	SWIR II	30
8	-	-	0.52-0.9	2.11 - 2.29	8	PAN	15
				0.50 - 0.68	9	Cirrus Clouds	30

*60m: MSS, 30m: TM/ETM+/OLI

**120m: MSS, 60m: TM/ETM+, 100m: TIRS

Blue: Designed for water body penetration (coastal waters)
Green: designed to measure green reflectance peak of vegetation for crop and vegetation discrimination.
Red: designed to sense in chlorophyll absorption bands for species differentiation.
NIR: useful for determining vegetation types, vigor and biomass content and for delineating water bodies.
SWIR I: Indicative of vegetation moisture content and soil moisture. Useful to discriminate clouds from snow.
TIR: Useful in vegetation stress analysis, soil moisture mapping and thermal mapping.
SWIR II: Useful for discrimination of mineral and rock types. Also sensitive for vegetation moisture content.

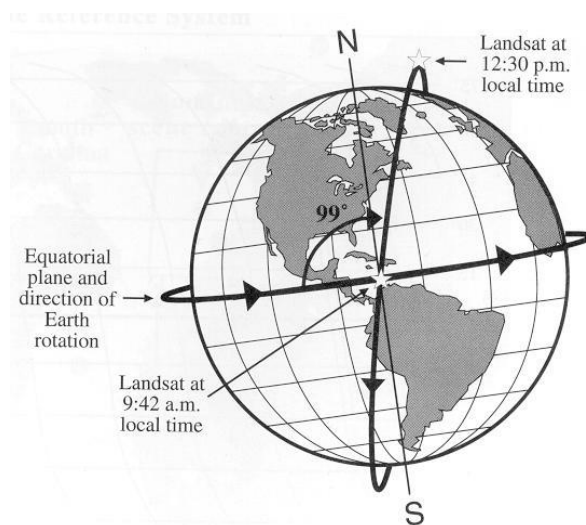


Figure 2.3: Sun-synchronous orbit of Landsat 4 and 5 (CCRS tutorial & Lillesand & Kiefer, 2000).

SPOT & Pléiades

The acronym of SPOT stands for **Système Probatoire d'Observation de la Terre** (Earth Observation Test System) and was the first earth observation satellite launched by an European country. It was developed and operated by the CNES: Centre National d'Études Spatiales at Toulouse. Recently the SPOT program has been taken over by Airbus Defence and Space (ADS). The SPOT sensor is a pushbroom scanner, it does not have moving parts such as a rotating mirror. Instead it has an array of detectors and each scan line is sampled at one go. Between 1986 and 2014, seven SPOT satellites have been launched. They had a near-polar, sun-synchronous, 832 km high orbit with a repeat time of 26 days. However, the direction of the sensors of SPOT could be changed up to 27°, enabling the SPOT-sensors to make oblique views of the earth (figure 2.4). This capability increased the repeat time considerable, up to several days. Each image covered a square of 60 or 120 km on a side, with a spatial resolution of 10 m (SPOT 1-4) or 2.5 m (SPOT 5) in panchromatic mode and had a very high geometric accuracy. The VEGETATION sensor was added to SPOT 4 and 5. This instrument was mainly designed for monitoring vegetation dynamics at the continental scale but it was also useful for meteorological observation and oceanographic studies. VEGETATION had a swath of 2250 km wide and a spatial resolution of 1 km at nadir. A few spectral bands (blue and mid infrared) are added compared to the earlier, high-resolution SPOT-XS (multispectral) designs. SPOT 5 was additionally equipped with a HRS (High-Resolution Stereoscopic imaging instrument) dedicated to taking simultaneous stereo pairs of a swath 120 km across (width of the observed scene centered on the satellite ground track) and 600 km long (maximum length of a scene) (figure 2.5). The stereo pairs are acquired in panchromatic (black and white) mode with a spatial resolution of 10 metres (along-track sampling of 5 meters) and a telescope viewing angle of ± 20°. The SPOT 5 mission operated beyond its years and is scheduled to be de-orbited before the end of 2015 (spot.cnes.fr). The SPOT program will then be completely taken over by Airbus Defence and Space (<http://www.space-airbusds.com/en/programmes/spot-603.html>), who already have SPOT 6 and 7 in orbit. These upgrades not only provide higher resolution images, they feature an additional blue band and, when operated together, make revisit times of 1 day possible.

Table 2.2: SPOT characteristics (Source: www.geo-airbusds.com)

Sensor	Band	Spatial Resolution m)	Spectral Range	Other
SPOT 1	PAN	10	0.50 - 0.73 µm	
SPOT 2	1: Green	20	0.50 - 0.59 µm	
SPOT 3	2: Red	20	0.61 - 0.68 µm	
	3: NIR	20	0.78 - 0.89 µm	
SPOT 4	Monospectral	10	0.61 - 0.68 µm	
	1 : Green	20	0.50 - 0.59 µm	
	2 : Red	20	0.61 - 0.68 µm	
	3 : NIR	20	0.78 - 0.89 µm	
	4: SWIR	20	1.58 - 1.75 µm	
SPOT 5	PAN	2.5 or 5	0.48 - 0.71 µm	
	1 : Green	10	0.50 - 0.59 µm	
	2 : Red	10	0.61 - 0.68 µm	
	3 : NIR	10	0.78 - 0.89 µm	
	4: SWIR	20	1.58 - 1.75 µm	
SPOT Veg (onboard SPOT 4&5)	0: Blue	1000	0.45 - 0.52 µm	Swath: 2250 km
	2: Red		0.61 - 0.68 µm	
	3:NIR		0.78 - 0.89 µm	
	4:SWIR		1.58 - 1.75 µm	
SPOT 6	PAN	1.5	0.45-0.745 µm	Altitude: 660 km
SPOT 7	1: Blue	6	0.45-0.520 µm	Inclination: 98°
	2: Green	6	0.53-0.590 µm	Swath: 60-120 km
	3: Red	6	0.62-0.695 µm	Daily revisit when combined.
	4: NIR	6	0.76-0.890 µm	

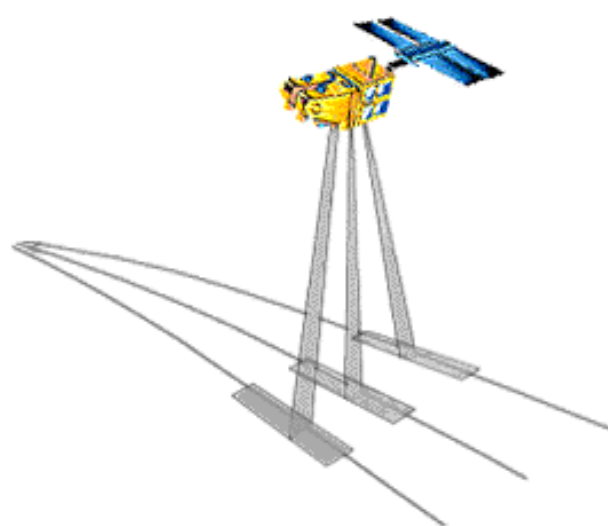


Figure 2.4: An illustration of SPOT off-nadir viewing system (*Curran, 1985*).



Figure 2.5: Illustration of SPOT's stereo-photogrammetric function (www.geo-airbusds.com)

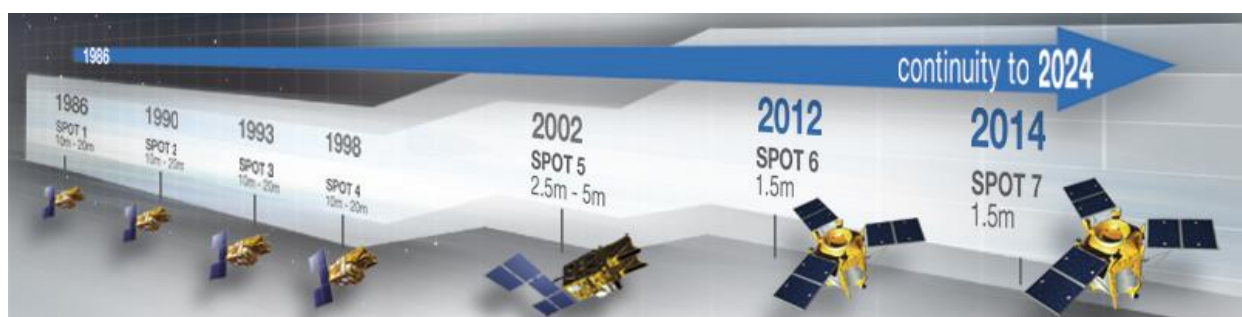


Figure 2.6: SPOT program's timeline (www.geo-airbusds.com)

The SPOT series of remote sensing instruments have been succeeded by the Pléiades twin satellite constellation. Pléiades 1A (launched December 2011) and 1B (December 2012) carry a High Resolution Instrument able to supply (stereoscopic) images of 0.7 m (PAN) and 2.8 m (RGB+NIR) resolution with a FOV of 20 km. The dual satellites can reach every point on Earth on a daily basis. They are spaced 180° apart, but together with the SPOT 6&7 satellites (who share the same orbital plane) they can form a constellation of four systems, spaced 90° apart (www.pleiades.cnes.fr).

Table 2.3: Pléiades Characteristics. (Source: www.pleiades.cnes.fr)

Pléiades Spectral Bands	Spectral range	Resolution
Pan	0.47 - 0.83 µm	0.7 m
Blue	0.43 - 0.55 µm	2.8 m
Green	0.50 - 0.62 µm	2.8 m
Red	0.59 - 0.71 µm	2.8 m
NIR	0.74 - 0.94 µm	2.8 m

Copernicus: Sentinel

The Copernicus program is one of the largest Earth observation programs to date (October 2015). It will provide accurate, timely and easily accessible information to improve the management of the environment, understand and mitigate the effects of climate change and ensure civil security. Copernicus is the new name for the Global Monitoring for Environment and Security program, previously known as GMES. This initiative is headed by the European Commission (EC) in partnership with the European Space Agency (ESA). ESA coordinates the delivery of data from upwards of 30 satellites. The EC, acting on behalf of the European Union, is responsible for the overall initiative, setting requirements and managing the services.

In order to fulfill the operational needs of the Copernicus program a new series of six satellites is being developed specifically for Copernicus: the Sentinels (figure 2.7). When completed they will provide a unique set of observations for land, ocean and atmospheric monitoring. Each Sentinel mission is based on a constellation of two satellites to fulfil revisit and coverage requirements.

Sentinel-1-A was launched April 2014, and is a polar-orbiting, all-weather, day-and-night radar imaging mission for land and ocean services. **Sentinel-1-B** is planned for early 2016. It will share the same orbital plane as 1-B, but with a 180° phase difference. **Sentinel-2**, with 2-A successfully launched on 23 June 2015 and 2-B planned for 2016, is designed to provide multispectral, high-resolution images for land monitoring (vegetation/soil cover, inland waterways etc.) It can also deliver information for emergency services. **Sentinel-3** will be a multi-instrument mission to measure sea-surface topography, sea- and land-surface temperature, ocean colour and land colour with high-end accuracy and reliability. The mission will support ocean forecasting systems, as well as environmental and climate monitoring. **Sentinel-4 and -5** will provide data for atmospheric composition monitoring from geostationary and polar orbits, respectively. The Sentinel-5 Precursor satellite mission is being developed to reduce data gaps between Envisat, in particular the Sciamachy instrument, and the launch of Sentinel-5. This mission will be dedicated to atmospheric monitoring. **Sentinel-6** will carry a radar altimeter to measure global sea-surface height, primarily for operational oceanography and for climate studies (ESA, 2015). For more, in-depth information on the Sentinel Missions, please refer to <https://sentinel.esa.int/web/sentinel>.

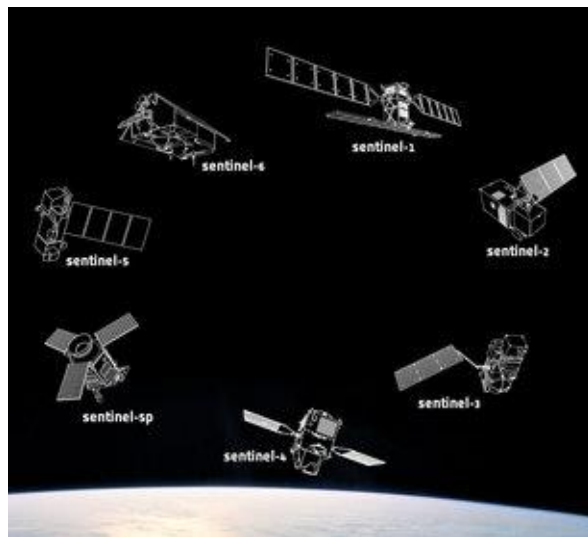


Figure 2.7: Sentinel 1-6 (earth.esa.int).

Sentinel-1 SAR

The first in the series, Sentinel-1, carries an advanced radar instrument to provide an all-weather, day-and-night supply of imagery of Earth's surface. It uses a form of Radar and will therefore be discussed in chapter 3.

Sentinel-2 MSI

Sentinel-2 carries an innovative wide swath high-resolution multispectral imager with 13 spectral bands for a new perspective of land and vegetation. With its multispectral imager and wide swath coverage, the Sentinel-2 mission not only offers continuity, but also expands on the French Spot and US Landsat missions (figure 2.8). The mission is based on a constellation of two identical satellites in the same orbit, 180° apart for optimal coverage and data delivery. Together they completely cover Earth's land surfaces, large islands, inland and coastal waters every five days at the equator (sentinel.esa.int).

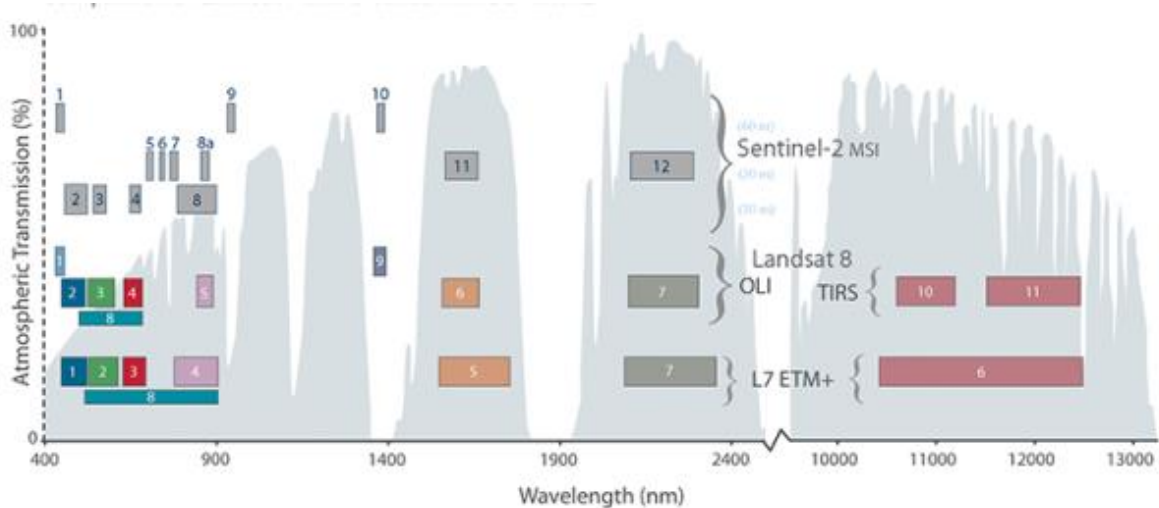


Figure 2.8: Comparison of Sentinel 2 bands with those of Landsat 7 and 8 (www.earth.esa.int).

The mission will mainly provide information for agricultural and forestry practices and for helping manage food security. Satellite images will be used to determine various plant indices such as leaf area chlorophyll and water content indexes.

As well as monitoring plant growth, Sentinel-2 can be used to map changes in land cover and to monitor the world's forests. It will also provide information on pollution in lakes and coastal waters. Images of floods, volcanic eruptions and landslides contribute to disaster mapping and help humanitarian relief efforts (*sentinel.esa.int*).

Narrowing the width of the Sentinel-2 spectral bands limits the influence of atmospheric constituents, including water vapor. The original Landsat NIR band (760-900 nm) was found to be band was used in previous missions: for the calculation of the ENVISAT MERIS Global Vegetation Index (MGVI), and in atmospheric corrections for NASA's MODIS sensor. Due to its potential impact on reflectance values, its use as an indicator in weather forecasting and its role in the trapping of incoming solar radiation, the presence of cirrus cloud needs to be addressed. Adding a spectral band at 1375 nm (band 10) enables cirrus detection. The correction of data for thin cirrus can be managed using Visible to Near InfraRed (VNIR) band information. This band is included in the MODIS instruments as band 26, and it is used in current US multispectral missions such as LANDSAT-8 and the Visible Infrared Imaging Radiometer Suite (VIIRS) (*sentinel.esa.int*).

Table 2.4: Sentinel-2 bands (www.earth.esa.int).

Band	Band width (μm)	Spatial Resolution (m)	Comment
1	0.43 - 0.45	60	Aerosol detection
2	0.46 - 0.52	10	
3	0.54 - 0.58	10	
4	0.65 - 0.68	10	
5	0.70 - 0.71	20	
6	0.73 - 0.75	20	
7	0.77 - 0.79	20	
8	0.78 - 0.90	10	
8a	0.86 - 0.88	20	
9	0.94 - 0.96	60	
10	1.36 - 1.39	60	Cirrus cloud detection
11	1.57 - 1.66	20	
12	2.10 - 2.28	20	

Table 2.5: Comparison of Landsat, SPOT and Sentinel 2 instrument characteristics (NASA, CNES, ADS, ESA)

	Landsat 1-8	SPOT 1-5/6&7	Sentinel 2
Instrument principle	Scanner	Pushbroom	Pushbroom
Repeat cycle (days)	16	26/1	5*
Swath width (km)	185	2*60	290
Spectral bands	11	5	13
Spatial resolution (m)	15, 30, 60	2.5, 10, 20/1.5, 6	10,20,60

TERRA Platform

On December 18, 1999, NASA launched Terra, its Earth Observing System (EOS) flagship satellite and became operational in February 2000. In particular, the mission is designed to improve understanding of the movements of carbon and energy throughout Earth's climate system (TERRA, 2005). Instruments aboard TERRA comprise ASTER for land surface studies, CERES for cloud and radiant energy monitoring, MISR a multiple view-angle instruments to 'look' e.g. into vegetation canopies, MODIS for monitoring large-scale changes in the biosphere and MOPITT to observe the

lower atmosphere. Two instruments, ASTER and MODIS, are of particular interest for geographical research and are presented below in more detail.

ASTER aboard TERRA

ASTER (Advanced Spaceborne Thermal Emission and Reflection Radiometer) instrument delivers high resolution, multispectral images since its launch in December 1999. ASTER is part of the TERRA platform and collects data in 14 bands across the spectral region from the visible to the thermal infrared. The spatial resolution varies with wavelength: the Visible and Near-infrared (VNIR) has three bands with a spatial resolution of 15 m, the Shortwave Infrared (SWIR) has 6 bands with a spatial resolution of 30 m, and the Thermal Infrared (TIR) has 5 bands with a spatial resolution of 90 m. A second near infrared band is pointed backwards providing stereo capabilities for DEM generation (ASTER, 2003).

Table 2.6: Aster system properties.

Characteristic	VNIR	SWIR	TIR
Spectral Range	1: 0.52 - 0.60 µm Nadir looking	4: 1.600 - 1.700 µm	10: 8.125 - 8.475 µm
	2: 0.63 - 0.69 µm Nadir looking	5: 2.145 - 2.185 µm	11: 8.475 - 8.825 µm
	3N: 0.76 - 0.86 µm Nadir looking	6: 2.185 - 2.225 µm	12: 8.925 - 9.275 µm
	3B: 0.76 - 0.86 µm Backward looking	7: 2.235 - 2.285 µm	13: 10.25 - 10.95 µm
		8: 2.295 - 2.365 µm	14: 10.95 - 11.65 µm
		9: 2.360 - 2.430 µm	
Ground Resolution	15 m	30m	90m
Data Rate (Mbits/sec)	62	23	4.2
Cross-track Pointing (deg.)	±24	±8.55	±8.55
Cross-track Pointing (km)	±318	±116	±116
Swath Width (km)	60	60	60
Detector Type	Si	PtSi-Si	HgCdTe
Quantization (bits)	8	8	12

MODIS aboard TERRA and AQUA

MODIS (Moderate Resolution Imaging Spectroradiometer) is a key instrument aboard the Terra (EOS AM) and Aqua (EOS PM) satellites. Terra MODIS and Aqua MODIS are viewing the entire Earth's surface every 1 to 2 days, acquiring data in 36 spectral bands in resolutions ranging from 250m to 1000m (MODIS, 2003). MODIS is designed for monitoring large-scale changes in the biosphere that will yield new insights into the workings of the global carbon cycle. MODIS can measure the photosynthetic activity of land and marine plants (phytoplankton) to yield better estimates of how much of the greenhouse gas is being absorbed and used in plant productivity. Coupled with the sensor's surface temperature measurements, MODIS' measurements of the biosphere are helping scientists track the sources and sinks of carbon dioxide in response to climate changes (MODIS, 2003).

Table 2.7: MODIS system properties (modis.gsfc.nasa.gov/).

Primary Use	Band	Bandwidth	Spectral Radiance	Required SNR
Land/Cloud/Aerosols Boundaries	1	620 - 670	21.8	128
	2	841 - 876	24.7	201
Land/Cloud/Aerosols Properties	3	459 - 479	35.3	243
	4	545 - 565	29	228
	5	1230 - 1250	5.4	74
	6	1628 - 1652	7.3	275
	7	2105 - 2155	1	110
	8	405 - 420	44.9	880
	9	438 - 448	41.9	838
Ocean Colour/Phytoplankton /Biogeochemistry	10	483 - 493	32.1	802
	11	526 - 536	27.9	754
	12	546 - 556	21	750
	13	662 - 672	9.5	910
	14	673 - 683	8.7	1087
	15	743 - 753	10.2	586
	16	862 - 877	6.2	516
	17	890 - 920	10	167
	18	931 - 941	3.6	57
Atmospheric Water Vapor	19	915 - 965	15	250

IKONOS

The first real commercial satellite was IKONOS. IKONOS is developed, built and maintained by the company Space Imaging. The first IKONOS satellite is launched on 27 April 1999 but failed. The second launch of an exact copy of the first Ikonos satellite took place on 24 September 1999. The sensor aboard Ikonos has a panchromatic band with a spatial resolution of 1 by 1 meter. Next it has a sensor with four multi-spectral bands: blue, green, red, and infrared of 4 by 4 meters. Various other, high spatial resolution sensors will follow Ikonos in the next few years. Examples are the EarlyBird and EarthWatch satellites by the EarthWatch Company. These image approach the level of detail and the quality of aerial photographs although the images are acquired from an orbit at 680 km.

Bands	Bandwidth (nm)	Spatial resolution (m)	Orbit
Ikonos Panchromatic		1x1	Altitude: 681 km Swath: 11 km
1	450 – 900 nm		
Ikonos XS		4x4	
1	450 – 520 nm (Blue)		
2	520 – 600 nm (Green)		
3	630 – 690 nm (Red)		
4	760 – 900 nm (NIR)		

Envisat

Envisat was an initiative of the European Space Agency (ESA) and was the successor of ERS1 and 2. Its launch was delayed several times but eventually reached orbit in January 2002. Envisat was a very large satellite (platform) (the largest civilian Earth observation mission) and carried 10 advanced instruments:

- MERIS: Medium Resolution Imaging Spectrometer
 - for ocean pigment concentration, clouds and water vapour and vegetation status.
- MIPAS: Michelson Interferometric Passive Atmospheric Sounder
 - for monitoring atmospheric gasses while looking at Earth limb (horizon).
- ASAR: Advanced Synthetic Aperture Radar
 - for ocean and sea ice applications and deforestation mapping
- GOMOS: Global Ozone Monitoring by Occultation of Stars
 - for ozon monitoring in the atmosphere using absorption features in star spectra.
- RA2: Radar Altimeter 2
 - for determining very accurately the satellite's orbit to calibrate the various sensors
- MWR: Microwave Radiometer
 - for measuring atmospheric humidity.
- LRR: Laser Reflectometer
 - for measure orbit altitude calibration of the Envisat platform
- SCIAMACHY: Scanning Imaging Absorption Spectrometer for Atmospheric Chartography
 - for measuring the concentration of trace gasses in the atmosphere
- AATSR: Advanced Along Track Scanning Radiometer
 - for measure sea surface temperature to study ocean currents and El Nino
- DORIS: Doppler Orbitography for Radiopositioning Integrated by Satellite.
 - for measuring ocean surface topography and variations in ice coverage.

Envisat had a sun-synchronous orbit with a mean altitude of 800 km. The Envisat mission ended on 08 April 2012, following the unexpected loss of contact with the satellite. More information on Envisat and its launch can be found on the internet pages: <http://www.esa.int> and <http://envisat.esa.int>

ERS: European Remote Sensing satellite

The main instrument aboard is a SAR-imaging radar, it does not have a multi-spectral scanner aboard. Therefore, the ERS satellite is described in the chapter on radar or microwave remote sensing.

SMOS (Soil Moisture and Ocean Salinity) and SMAP (Soil Moisture Active Passive)

SMOS (ESA) and SMAP (NASA) are both passive microwave (radar) based missions developed to monitor top soil moisture content and (in the case of SMOS) ocean salinity. Both will be discussed in the chapter on radar remote sensing.

HCMM: Heat Capacity Mapping Mission

See the chapter on thermal remote sensing.

2.4 Airborne Sensors

Remote sensing observations are not only made from out of space but are also frequently carried out by sensor systems mounted in an aircraft. The systems used is always a trade-off between technical possibilities, costs and the image specifications requested by the users. Furthermore, sensors in an experimental stage of development are often first tested in an aircraft before they are planned aboard satellites. Physical Geography of Utrecht is for example involved in feasibility studies of imaging

spectrometers such as AVIRIS, DAIS7915 and GERIS. Some examples of airborne sensors are presented in the next sessions.

CAESAR

CAESAR is an acronym for CCD Airborne Experimental Scanner for Applications in Remote Sensing and is developed and built by the Dutch NLR and TNO. It can be used for terrestrial and marine surveys. For that purpose, it has a modular design in such a way that the sensors can be changed following the user's requirements. The 'land mode' of Caesar has 3 spectral channels centred on 0.55, 0.67 and 870 µm. The spatial resolution depends on the altitude of the aircraft. At nominal altitude of 3000 m, the pixel size is around 0.75 m. A detailed study to the usefulness of CAESAR for vegetation survey is carried out by Kloosterman et al. (1991).

Daedalus

Another well-known airborne scanner is the Daedalus scanner. In its basic mode it has twelve channels from which seven in the visible wavelengths, three in the near infrared red part of the spectrum and two in the thermal bands. The spatial resolution at the nominal aircraft altitude of 19.5 km is around 25 m.

GERIS and AVIRIS

GERIS (Geophysical Environmental Research Imaging Spectrometer) developed by the GER-company and AVIRIS (Airborne Visible and Infrared Imaging Spectrometer) developed by the Jet Propulsion Laboratory (JPL) of NASA are so-called *imaging spectrometers*. Imaging spectroscopy refers to the acquisition of images in many, very narrow, contiguous spectral bands in the optical part of the spectrum: the visible, near-infrared and mid-infrared portions of the spectrum (Goetz et al., 1985). Spectral reflectance curves of minerals and some vegetation tissues have diagnostic, narrow absorption bands which allow their identification by remote observation (figure 2.9). Imaging spectroscopy requires a bandwidth of approximately 15 nm, otherwise the spectral signature with absorption features is lost in the overall reflectance (De Jong, 1994). Therefore, GERIS and AVIRIS have narrow bands in the optical range of the spectrum (table 2.8):

AVIRIS has **224** contiguous spectral bands with a bandwidth of 10 nm between 0.4 and 2.5 µm and a nominal pixel size of 20 meters. Examples and applications of imaging spectroscopy will be discussed in the following sections.

Table 2.8: Technical Specifications of GERIS.

Wavelength Range	Module	Channels	Bandwidth
0.477 - 0.843 µm	VIS/NIR	31	12.3 nm
1.440 - 1.800 µm	SWIR I	4	120 nm
2.005 - 2.443 µm	SWIR II	28	16.2 nm
Average altitude: 3000 m			
Instantaneous field of view (IFOV): 90°			
Nominal ground resolution: 10 x 10 m			
Pixels per scanline: 512			
Dynamic range: 16 bits			

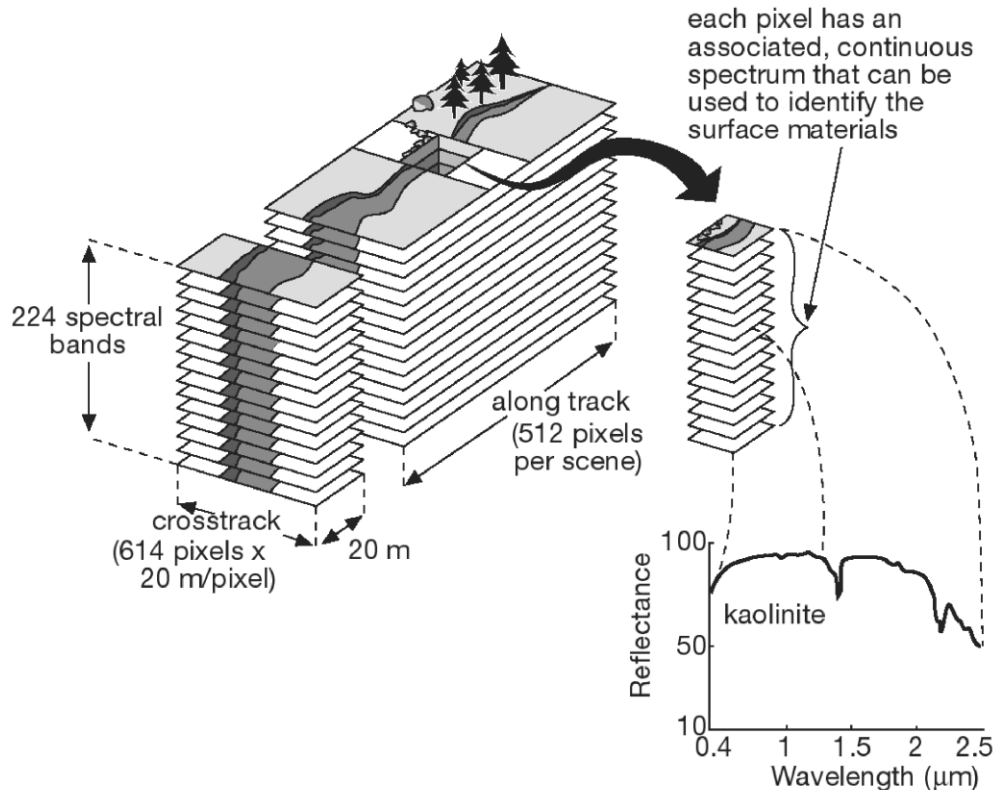


Figure 2.9: Concept of imaging spectroscopy.

Unmanned Airborne Vehicles

Rapid technological advancements have led to the development of a new, very versatile method of remote sensing image acquisition. Unmanned Airborne Vehicles (UAVs) or drones fill a niche in the remote sensing system hierarchy, being able to provide on-demand, high-resolution images at a relatively low cost. They are extremely versatile in the sense that UAVs can be equipped with various sensors (RGB, NIR, LiDAR) depending on the research objective, and because flight plans can be easily changed according to weather conditions. Depending on the sensor drones can provide images with a spatial resolution of centimetres.

UAVs take series of images over a (pre-programmed) flight path. By means of on-board GPS and orientation instruments the images can at a later stage be georeferenced in certain software packages (e.g. Agisoft Photoscan). Since multiple images are acquired over the same area, UAV images also provide the possibility of stereo-photogrammetric research, e.g. for creating a Digital Elevation Model of an area.

Drones are often employed in agriculture: by means of a NIR sensor farmers use the high-resolution images to monitor the health of their crops on almost a plant-by-plant basis. This allows them to precisely determine where to add extra fertilizer or water. UAVs have also been applied in wildlife reserves: using the information gathered by the drones rangers can quickly assess where illegal woodcutting or poaching is occurring, allowing for rapid response and prevention.

UAVs can be as simple or as complex as need be. In principle a hobby-airplane with a simple hand-held camera can already provide images one could need.

Even though UAVs can provide excellent images, obtaining them still requires one to travel to the area under investigation.



Figure 2.10: Deploying the SenseFly Swinglet UAV (www.sensefly.com).

3. Remote Sensing in the Microwave Region (RADAR)

3.1 Introduction

Radar is most often an active remote sensing system, it provides its own source of electromagnetic energy. The radar system 'illuminates' the terrain with electromagnetic energy with intervals of wavelengths between 1 mm and 1 m and detects the energy returning from the objects in the terrain. Passive Radar systems exist but the amount of energy emitted by objects (Stefan Boltzmann equation) in the microwave part of the spectrum is very small, consequently pixels must be large and bands must be wide.

Radar is an acronym for **Radio Detection and Ranging**. Radar was developed during World War II for navigation and target location (Sabins 1987). These systems use the familiar rotating antenna and circular CRT (Cathode-Ray-Tube) display. Radar systems have a few important advantages over other remote sensing systems (FAO, 1993):

1. Due to its own energy source radar systems operate independent of the sun. Hence, observations are possible during day and night.
2. Control of the emitted electromagnetic energy in terms of frequency or wavelength, power and polarization.
3. Control of the depression angle and azimuth angle to meet the objectives of the study.
4. The radiation in the microwave region of the spectrum is hardly scattered nor absorbed in the atmosphere by clouds or fog. As a result, radar observations can be made independent of weather conditions. Radar 'looks through' the clouds and fog. This is especially useful for remote sensing of regions in the humid tropics e.g. tropical rainforest with an almost permanent cloud cover.
5. The penetrating capacity of radar enables it to obtain information on subsurface features, when low soil density and low soil moisture conditions permit.

Radar remote sensing was developed using airborne systems such as the SLAR. The usefulness of space borne radar remote sensing was proven by the Seasat satellite in 1978. Space born radar images are now widely available from many sources e.g. the European ERS 1, 2, ENVISAT and Sentinel-1 satellites, SMOS and its USA counterpart SMAP and ASCAT.

3.2 Principle of a Radar System

The working method of radar is explained here by describing the airborne **SLAR system: Side Looking airborne Radar**, but radar systems aboard aircrafts are also applicable to satellite systems. The SLAR system is shown in figure 3.1. An antenna emits radar pulses (short bursts of electromagnetic energy) sideways and the same antenna receives the return pulses from the terrain. Compare solid and dashed lines in figure 3.1. An electronic switch or duplexer, prevents interference between emitted and received pulses by blocking the receiver circuit or emission unit. The reflection or backscatter by the various objects (stronger or weaker) produces an image with various greytones.

The pulses from the antenna illuminate strips of terrain in the *look direction* or range direction of the system. The look direction is oriented with an angle of 90° to the *azimuth direction* (i.e. the aircraft's flight direction). Figure 3.1 also illustrates that the time the radar pulse is travelling (antenna - house - antenna, antenna - tree - antenna), is important. The shortest travel time (the house near the aircraft) is called *near range*, the longer travel time (the tree) is called *far range*. The travel time of the pulses ($c=3*10^8$ m/s) is registered and used to create a scan line on a monitor. Multiple scan lines put together makes an image. Hence, radar differs from other remote sensing systems because it records data (images) on the basis of time rather than angular distance.

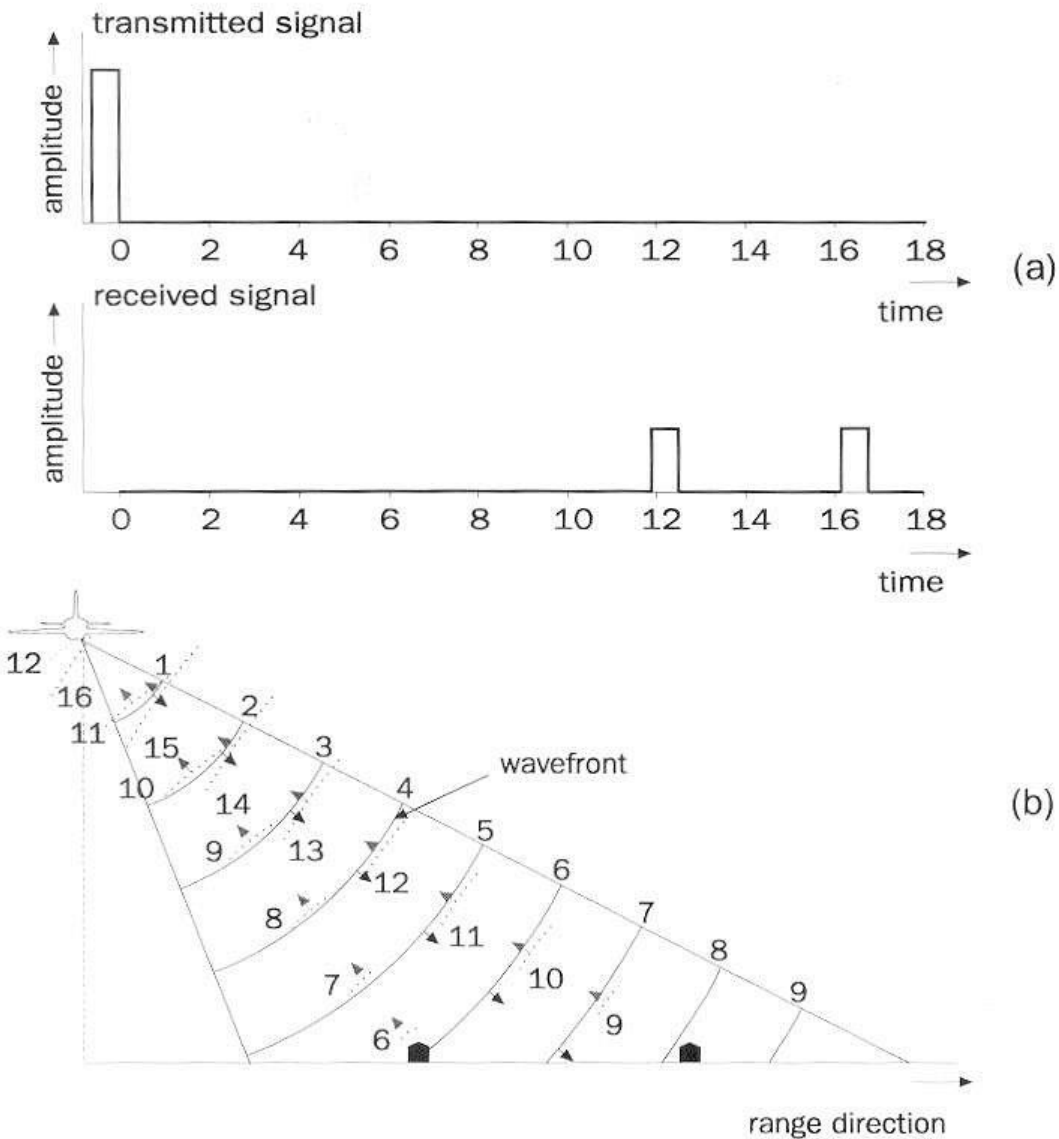


Figure 3.1: Operating principle of SLAR (Lillesand & Kiefer, 1994).

3.3 Radar Wavelengths

Radar systems do not use the entire microwave region of the spectrum but uses specific bands. As radar was developed during war time, all information was classified and a random letter code was assigned to different frequencies or wavelengths. This random letter code is very confusing and unfortunately, it is still used to specify radar systems aboard satellites and aircrafts. Table 3.1 summarizes the most important letter codes with their frequency and wavelength.

Table 3.1: Radar wavelengths and frequencies used in remote sensing (Sabins, 1987).

Band	Wavelength (cm)	Frequency (GHz)
Ka	0.8 - 1.1	40.0 - 26.5
K	1.1 - 1.7	26.5 - 18.0
Ku	1.7 - 2.4	18.0 - 12.5
X	2.4 - 3.8	12.5 - 8.0
C	3.8 - 7.5	8.0 - 4.0
S	7.5 - 15.0	4.0 - 2.0
L	15.0 - 30.0	2.0 - 1.0
P	30.0 - 100.0	1.0 - 0.3

3.4 Spatial Resolution

The spatial resolution in the look direction (range) and azimuth direction (aircraft heading) of a radar system is determined by the engineering properties of the antenna. An important property is the **depression angle (γ)**, the angle between the horizontal plane and a beam from the antenna to the target (figure 3.2). The depression angle is steep near the aircraft and shallower at far range. The second important factor is the pulse length (τ). **Pulse length** is the duration of the emitted pulse and is measured in μsec . Hence, the spatial resolution in the **range (look) direction** varies with the distance from the aircraft. Figure 3.3 and 3.5 illustrate the principle of spatial resolution in the range (look) direction.

The spatial resolution in the azimuth direction (aircraft heading) is determined by the width of the terrain strip illuminated by the radar beam. As the distance between radar pulse and aircraft increases, the radar beam gets wider. Consequently, at near range the resolution is smaller than in the far range. Figure 3.4 illustrates the principle of azimuth resolution. The angular beam width is a function of the distance from the aircraft but also of the wavelength of electromagnetic energy used. The angular beam width of a radar system is inversely proportional to *antenna length*. Therefore, spatial resolution improves with longer antennas, but there are practical limitations to the maximum antenna length (depends on the size of the aircraft or satellite). Formulae to compute the spatial resolutions of radar systems can be found in Sabins (1987).

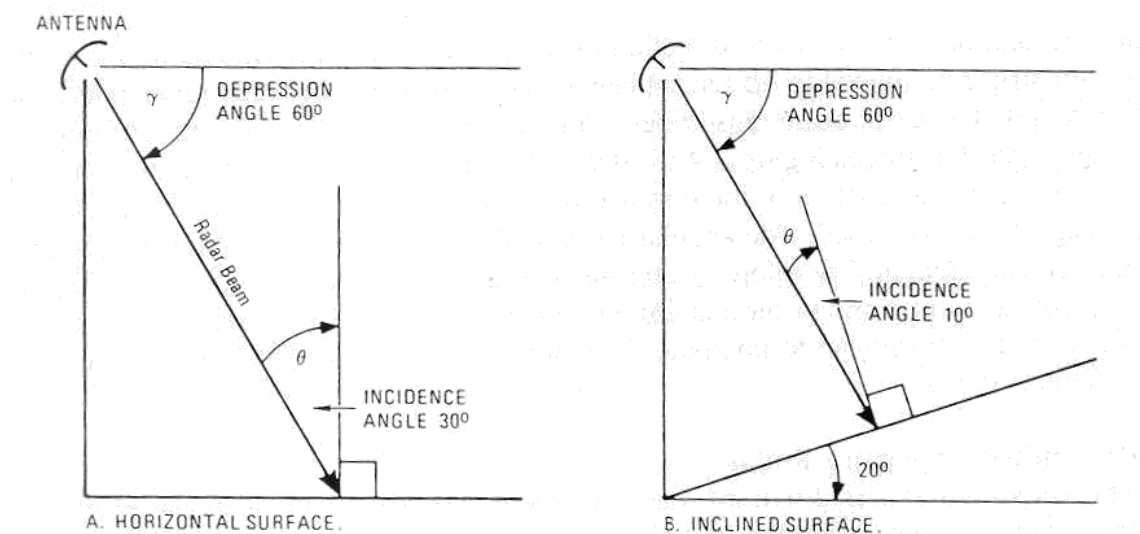


Figure 3.2a: Incidence angle and depression angle (Sabins, 1987).

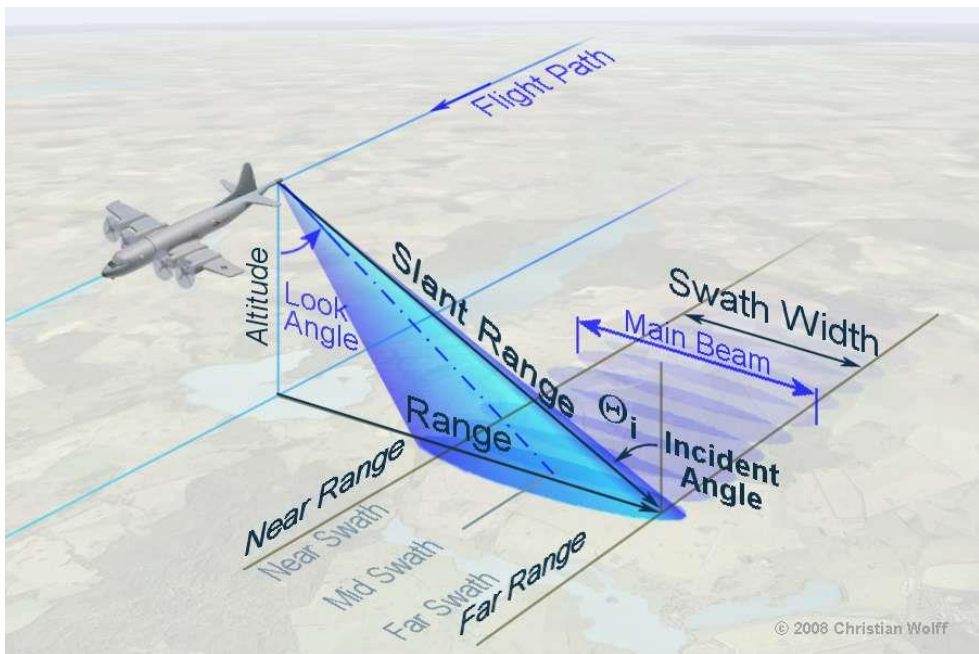


Figure 3.3b: Range, incidence angle, look angle and depression angle (180-look angle) (www.radartutorial.eu).

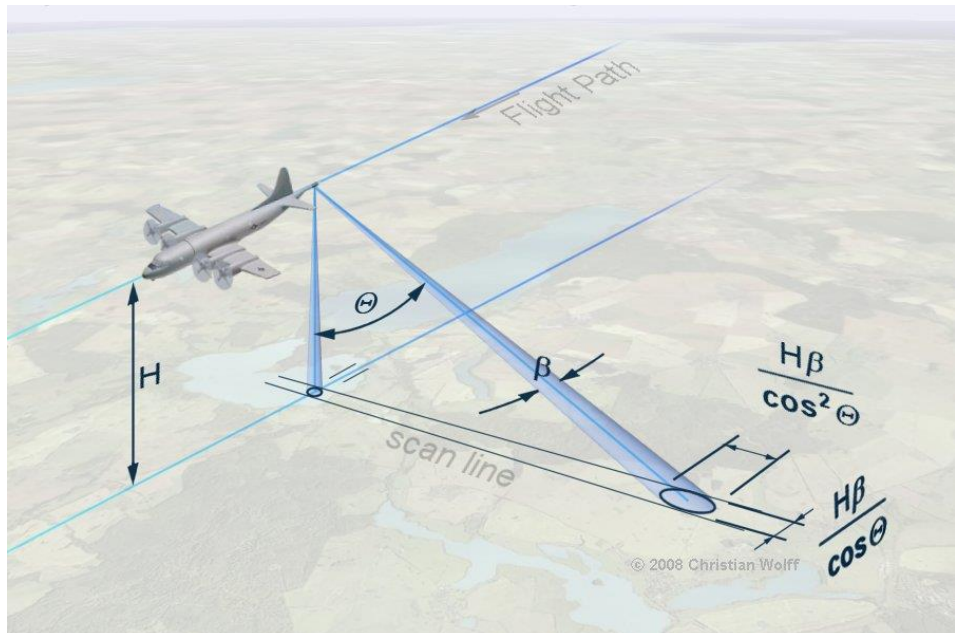


Figure 3.4: Radar resolution in range ($\frac{H\beta}{\cos^2 \Theta}$) and azimuth ($\frac{H\beta}{\cos \Theta}$) direction with increasing range, with:
 H = flight altitude, Θ = grazing angle and β = antenna beam width (www.radartutorial.eu).

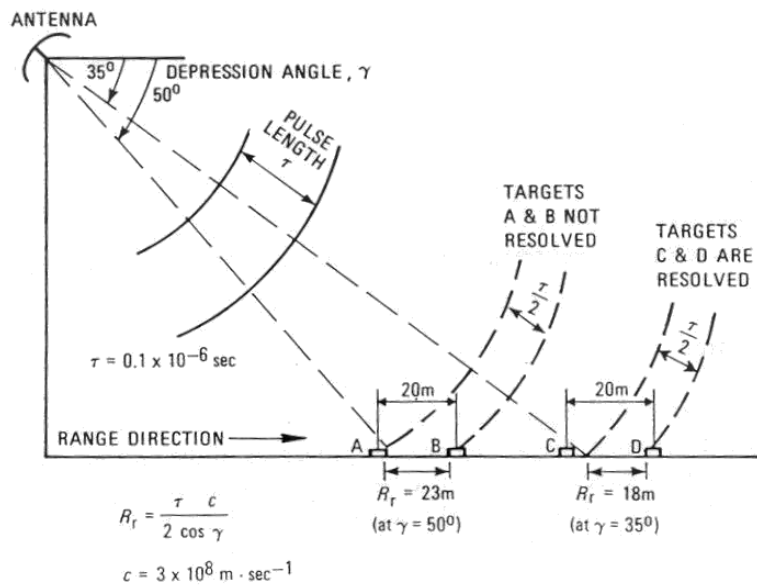


Figure 3.5: Radar resolution in the range (look) direction (Sabins, 1987).

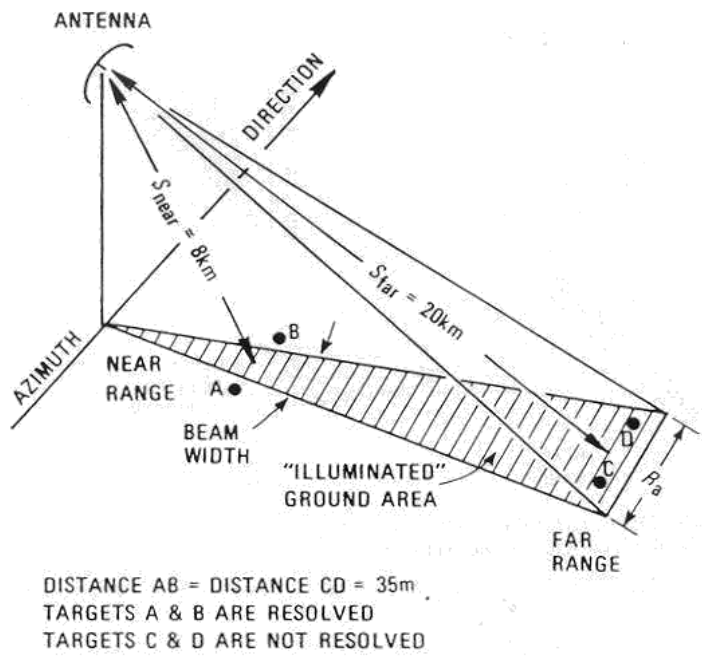
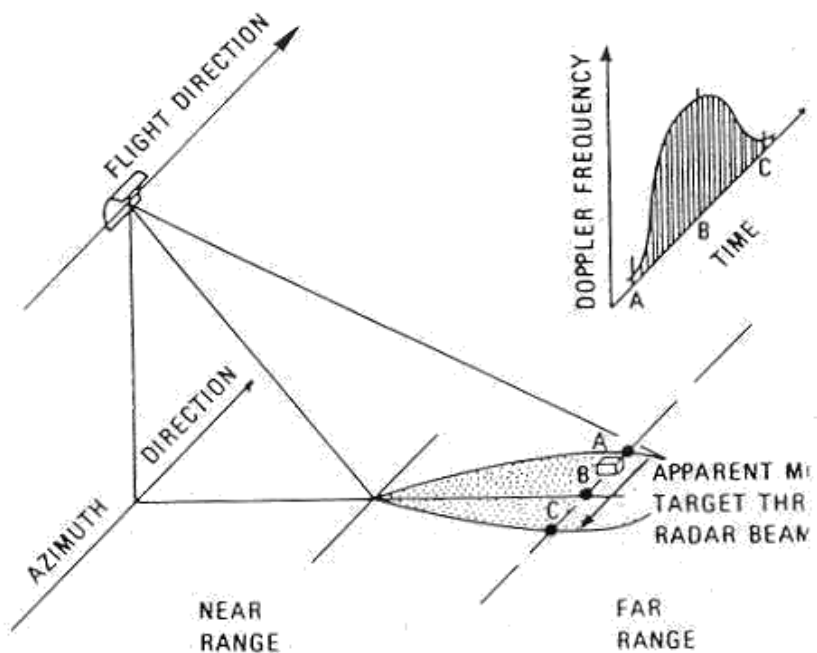


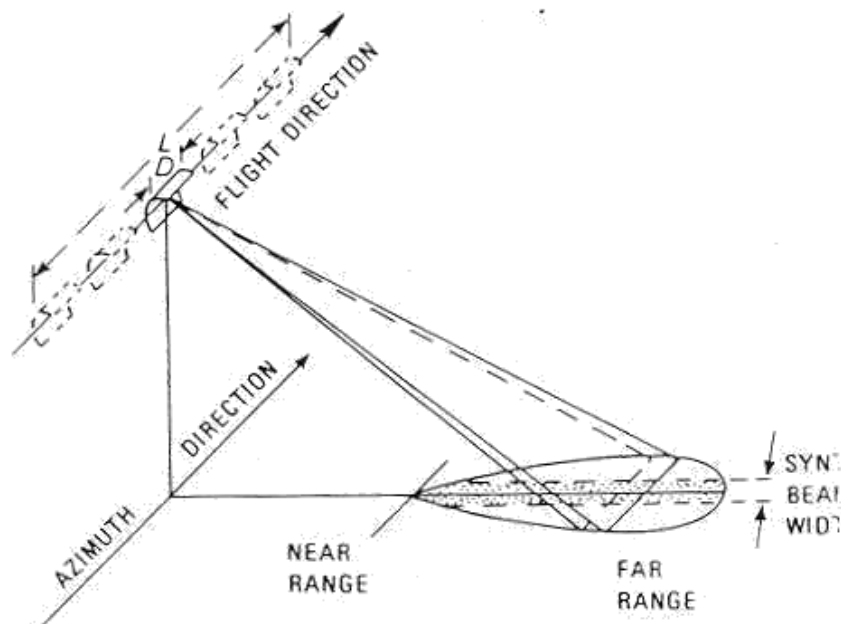
Figure 3.6: Radar beam width and resolution in the azimuth direction (Sabins, 1987).

3.5 SAR: Synthetic Aperture Radar

In the previous section it was discussed that apart from wavelength, the antenna length was an important factor to determine the spatial resolution of a radar system: spatial resolution improves with longer antennae. Traditional radar systems used an antenna of the maximum practical length or **real aperture**. The **Synthetic Aperture Radar or SAR** employs a relatively small antenna that transmits a broad beam. The Doppler principle (and special software) are employed to synthesize the azimuth resolution of a very narrow beam. Hence, a technical trick is used to increase the antenna length. Figure 3.6 and 3.7 show the SAR principle.



A. DOPPLER FREQUENCY SHIFT DUE TO RELATIVE MOTION OF TARGET THROUGH RADAR BEAM.



B. RESOLUTION OF SYNTHETIC-APERTURE RADAR IN THE AZIMUTH DIRECTION. NOTE THAT THE PHYSICAL ANTENNA LENGTH D IS SYNTHETICALLY LENGTHENED TO L .

Figure 3.7: Synthetic Aperture Radar (SAR) system (Sabins, 1987).

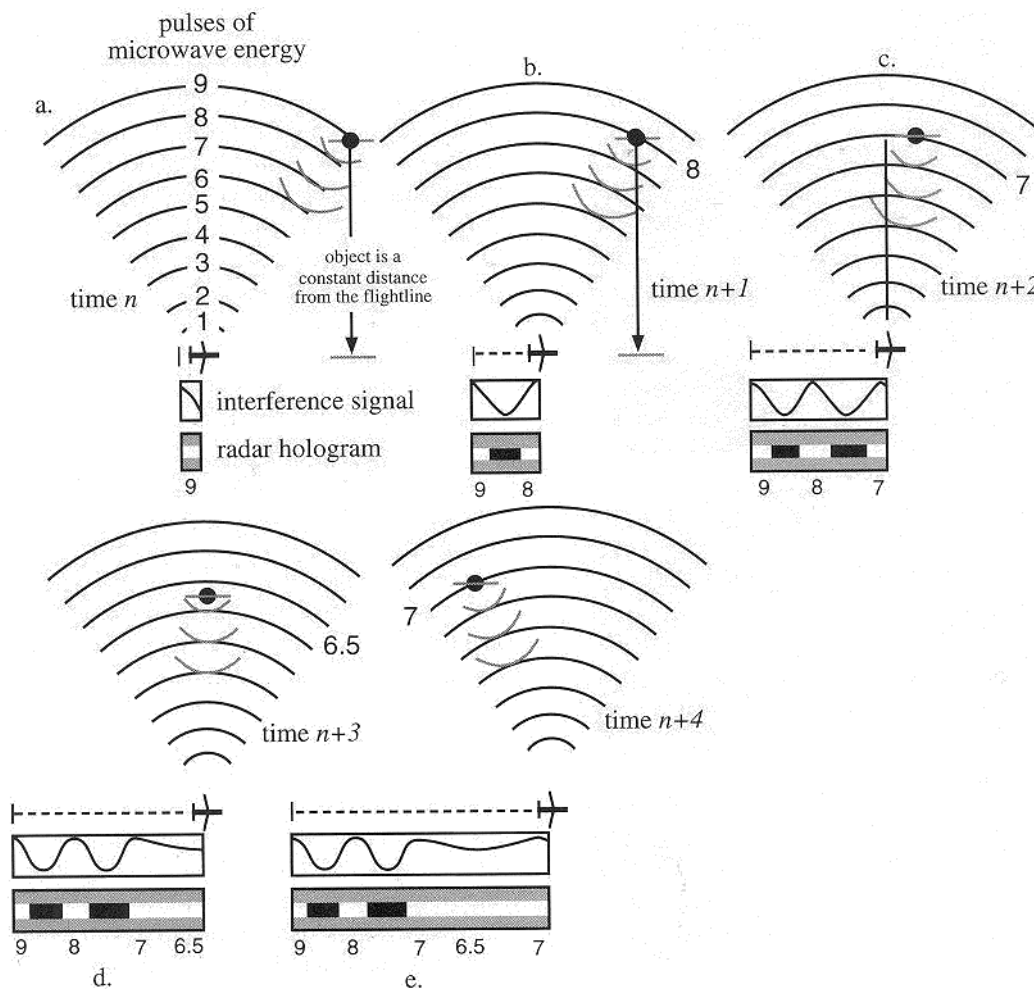


Figure 3.8: Concept of Synthetic Aperture Radar (SAR) system cont'd.

3.6 Geometry of Radar Images

The nature of the radar remote sensing systems causes specific geometric characteristics in the images such as shadows, and bright spots, slant-range distortion and image displacement. Generally, topography has four effects on radar images: corner reflection, long shadows, terrain overlay and terrain foreshortening:

Corner reflection occurs when a microwave pulse is reflected straight back to the antenna as a result of double reflection from a horizontal and then a vertical surface as shown in figure 3.8. The returning pulse has so much energy that it saturates the system and produces a white spot on the radar image.

Long shadows are the results of an object shielding an area from the oblique microwave pulse (figure 3.9). Long shadows are an advantage for the geomorphologists as they give an impression of the relief of the terrain. On the other hand it is a loss of data, no observations can be performed in the shadow portions of the terrain.

Terrain layover is the result of a microwave pulse hitting a high point like the top of a steep mountain before it hits a low point like a river valley, which is further from the aircraft ground track but nearer to the antenna (figure 3.9). As a result all tall objects seem to lean towards the aircraft's ground track.

Terrain foreshortening is a result of a microwave pulse hitting a point like a valley before or at the same time, that the pulse hits a higher point such as a mountain (figure 3.9). As a result a slope facing the antenna will be compressed on a radar image.

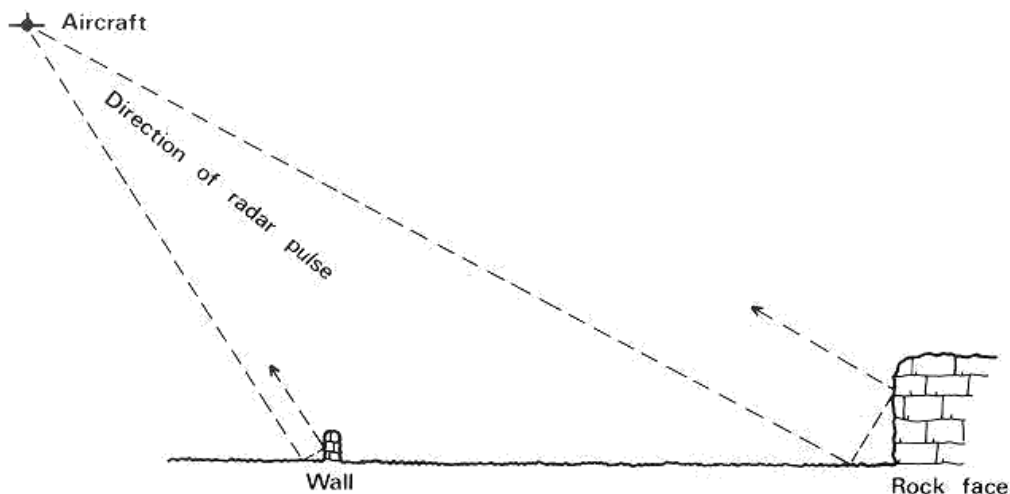


Figure 3.9: Corner reflection: the microwave radiation is reflected straight back to the antenna (Curran, 1985).

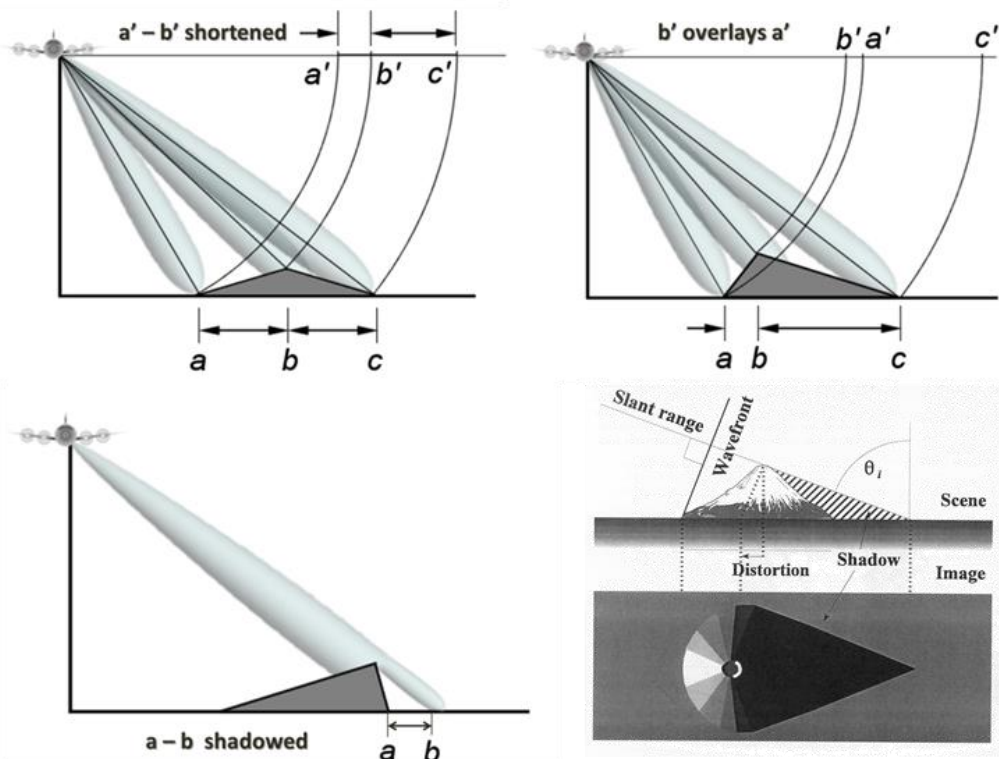


Figure 3.10: Radar illumination and shadows at different depression angles (www.radartutorial.eu and Henderson & Lewis, 1998).

3.7 Radar Return and Image Signatures

Radar images are always characterized by speckle. **Speckle** refers to the grainy or salt and pepper pattern of dark and bright spots in radar images. Speckle is a result of the antenna transmitting many minor pulses along with each major pulse. These pulses often reinforce or suppress the backscatter of the major pulse and speckle in the image is the result. Speckle is tedious for visual interpretation of radar images and it hampers seriously automatic analysis and classification.

Stronger radar returns produce normally brighter signatures on an image than weaker returns. The intensity of the radar return (backscatter) for both aircraft and satellite systems is determined by the following properties:

1. Radar System properties:

- Wavelength
- Depression angle
- Polarization

2. Terrain properties:

- Dielectric properties especially moisture content
- Surface roughness
- Feature orientation.

The **dielectric constant** or complex dielectric constant is a measure of the electric properties of the surface. It consists of two parts: permittivity and conductivity. In dry conditions most natural materials have a dielectric constant between 3 and 8. Water itself has a high dielectric constant around 80. Consequently, a change in moisture content generally results in a significant change in the dielectric properties of natural surfaces: increasing moisture content is associated with an increased radar reflectivity. The electromagnetic wave penetration in an object is an inverse function of water content. For vegetation, penetration depth depends on moisture, density and geometric structure of the plants: leaves and branches.

Surface roughness is the terrain property that most strongly influences the strength of the radar returns. Surface roughness is not the same as topographic relief. Surface roughness is measured in centimetres and is determined by the textural features of the surface comparable in size to the radar wavelength such as leaves and branches of vegetation and sand, gravel and cobble particles. For most surfaces the vertical relief or average height of surface irregularities is an adequate approximation of surface roughness. Surfaces are mostly grouped in smooth and rough surfaces (figure 3.10) according to the Rayleigh criterion. The *Rayleigh criterion* considers a surface to be smooth if:

$$h < \lambda / (8 \sin \gamma)$$

where h is the vertical relief (cm), λ is the radar wavelength (cm) and γ is the depression angle of the radar system. For a radar system with a wavelength of 23.5 cm (e.g. Seasat) and a depression angle of 70° the surface relief below which the surface will appear smooth on the radar image is 3.1 cm. An example of the effect of surface roughness can be observed in the zones of contact between land and water. Inland water bodies tend to be relatively smooth (little or no waves), most radar radiation is reflected away from the radar system and the water body appears as a dark spot on the image. The sea with many waves and hence a rough surface has many exposed and shadowed surfaces resulting in a pattern of dark and bright spots or lines.

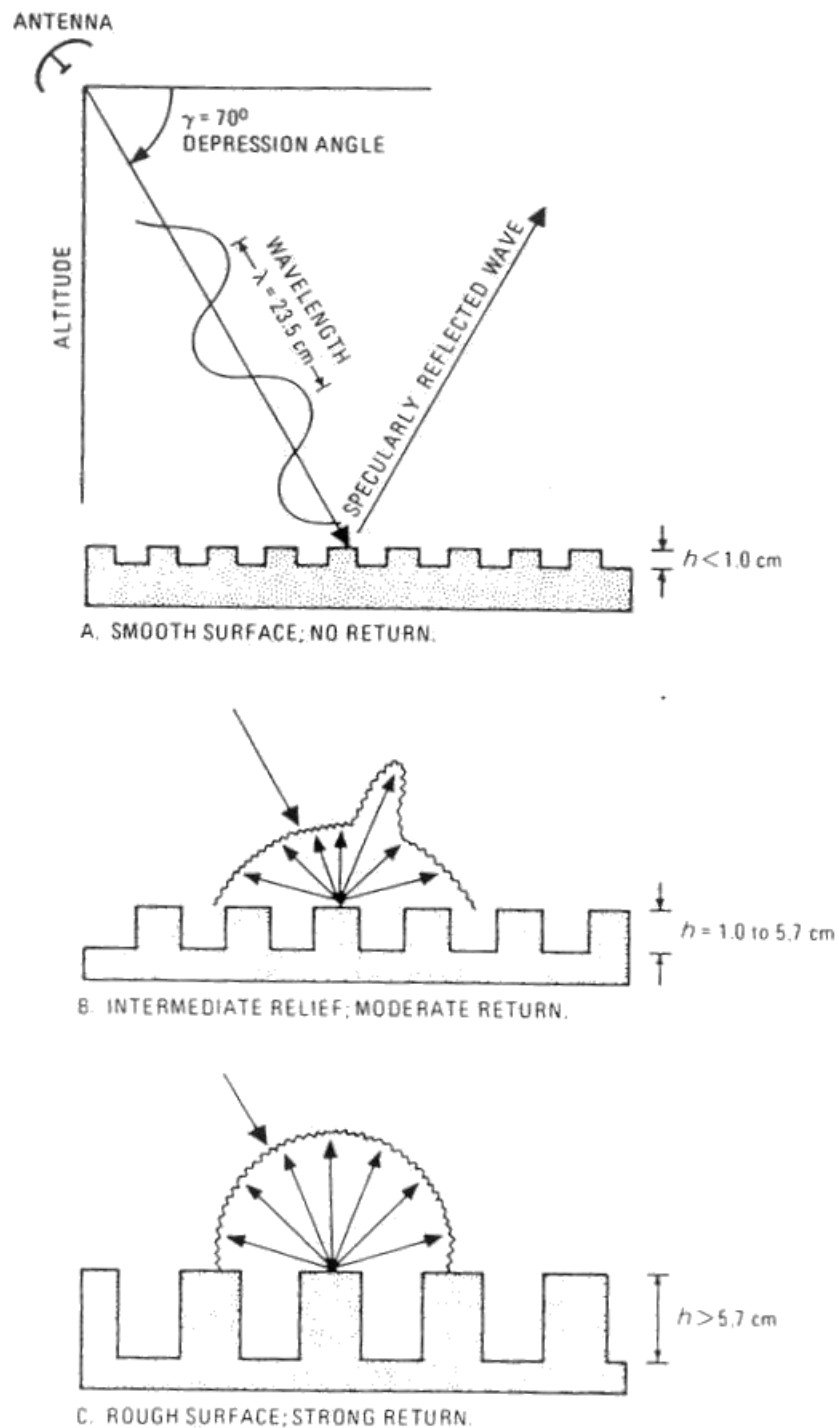


Figure 3.11: Models of surface roughness criteria and return intensity for a 23.5 cm radar system (Sabins, 1987).

Look direction and **feature orientation** are closely related and their effect on the radar image depends on the chosen aircraft track and the look direction of the radar system and the topographical properties of the terrain. Linear geologic features such as faults, outcrops and lineaments that are oriented at a normal or oblique angle to the radar look direction are enhanced by highlights and shadows in the

image. Features oriented parallel with look direction are suppressed and are difficult to recognize in the image.

The wavelength of the incident radar radiation determines:

- the penetration depth of the waves into the objects at the surface
- the relative roughness of the surface considered (see section on surface roughness).

Penetration depth tends to increase with longer wavelengths. A X-band radar (3 cm) will only penetrate the first leaves on top of the trees of a forest. Hence, such an image will provide information on the canopy structure of the forest. A L-band radar (23 cm) will penetrate much further and in that case the image contains information on branches and tree trunks. Figure 3.11 illustrates the effect of wavelength on different natural surfaces.

Polarization describes the direction or orientation in which the electromagnetic radiation vibrates (e.g. in the vertical or horizontal plane). When radar radiation strikes the terrain, most of the energy returns to the antenna with the same polarization as the emitted pulse. This energy is recorded as like polarized or parallel polarized. However, terrain surfaces also tend to change the polarization of the electromagnetic energy. Most radar systems transmit polarized pulses and can register vertical and/or horizontal polarization. Radar systems carry often an indication of the type of polarization transmitted and the type of polarization that they register: **HH, VH, HV, VV**. The first term refers to the polarization of the emitted radiation, the second term to the received radiation. Hence, X_{HV} refers to the X-band, H transmit and V receive.

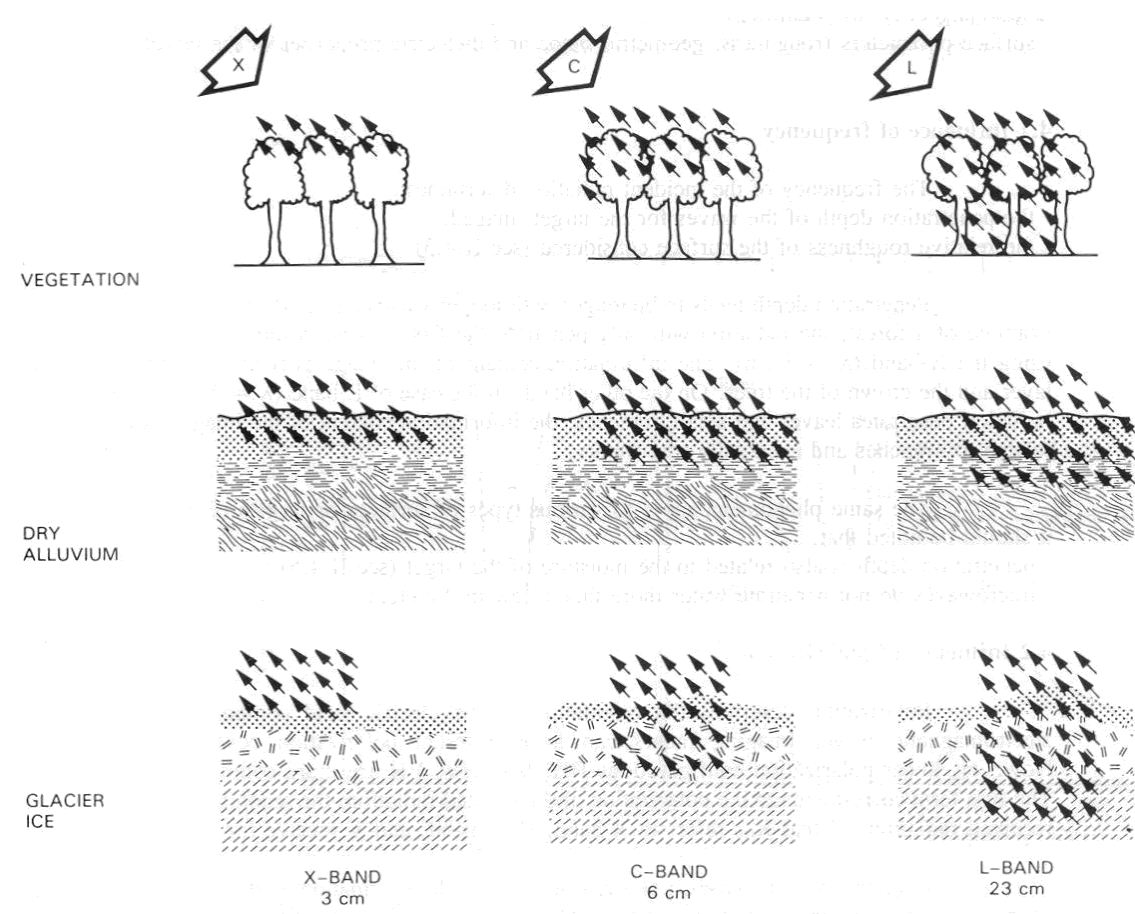


Figure 3.12: Backscatter of natural targets in the microwave spectrum (FAO, 1993).

3.8 Radar Satellites

Although earth resources satellites are in orbit since 1972 and provide many images of the earth's surface, the data availability for applications in agriculture and renewable resources has been a problem. The main cause for the limited data availability is poor atmospheric conditions: cloud cover and/or rain or other bad weather conditions. Especially, the tropical zones with an almost continuous cloud coverage and the temperate climate zones with very frequent cloud coverage lack sufficient optical images for e.g. land cover surveys. Therefore, radar techniques which are independent of solar illumination and atmospheric conditions has been an issue of research and several radar satellites are planned or already available.

Seasat

Seasat was an experimental satellite designed by NASA to establish the utility of microwave sensors for remote sensing of the oceans, but Seasat images have also proven to be valuable for terrain observations. Seasat was launched in June 1978 and unfortunately it ceased operation already in October 1978 because of a major electrical failure. Seasat had a circular, *non* sun-synchronous orbit at an altitude of 800 km with two interesting sensors aboard 1) a radiometer in two wavebands: visible (0.47-0.94 µm) at a spatial resolution of 2 km and thermal infrared (10.5-12.5 µm) at a spatial resolution of 4 km, 2) a Synthetic Aperture Radar or SAR with an L-band (23.5 cm with an HH polarisation and a nominal spatial resolution of 25 m and a depression angle between 67° and 73°.

ERS: European Remote Sensing satellite

Very important satellite were ERS-1 and ERS-2. ERS-1 was the first European satellite of the European Space Agency ESA and was launched on 17 July 1991 and retired in March 2000. ERS-1 is shown in figure 3.12. ERS-2 was launched in 1995 and was retired in September 2011. Apart from a radar remote sensing system this satellite had several other instruments, which are briefly described here. A detailed description can be found at <https://earth.esa.int/web/guest/missions/esa-operational-eo-missions/ers>. ERS-1 and 2 both carried three principal sensors:

1. AMI: the Active Microwave Instrumentation with three modes, a Synthetic Aperture Radar (SAR) in the C-band (5.7 cm) in image mode and in wave mode and a Wind Scatterometer.
2. RA: the Radar Altimeter
3. ATSR: Along Track Scanning Radiometer with two instruments, a thermal infrared radiometer (IRR) and a microwave sounder (MWS).

ERS-2 added an additional sensor for atmospheric ozone monitoring: GOME, Global Ozone Monitoring Experiment. The two satellites acquired a combined data set extending over two decades.

This satellite and its planned successors were aimed at worldwide monitoring of oceans, coastal waters, polar seas and ice and also were, to a more limited extent, of significance to land applications e.g. agricultural statistics.

The most important properties of ERS for environmentalists were:

ERS:

- | | |
|--|---------------------------|
| 1. AMI: SAR-C system | Altitude: 785 km |
| 2. RA: Radar Altimeter: K _u -band | Inclination: 98.5° |
| 3. ATSR-thermal radiometer | Revisit period: ± 16 days |
| 4. GOME ozone monitor | SAR pixel size: ± 30 m |
| | ATSR pixel size: ± 50 km |

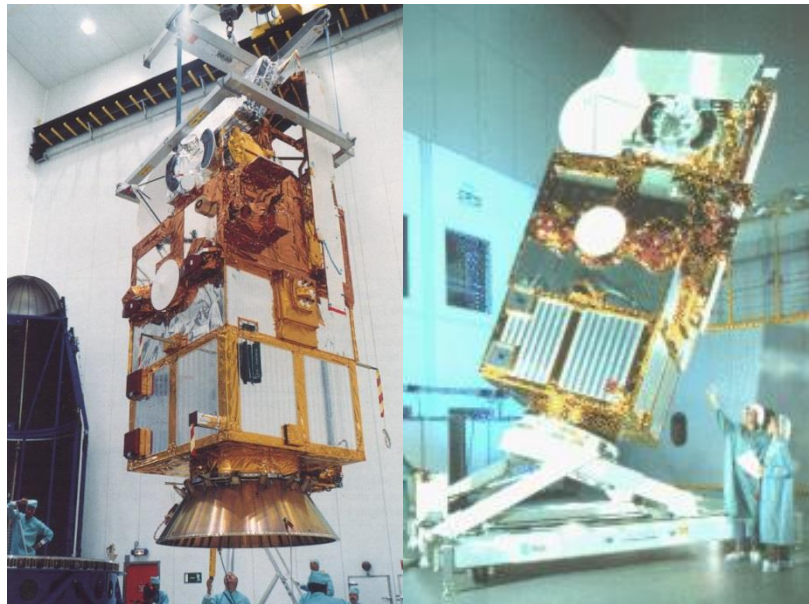


Figure 3.13: The ERS-1(left) and 2 (right) satellites in the test room at ESTEC in Noordwijk NL (earth.esa.int).

The **AMI in image mode, SAR**, obtained strips of high-resolution images (± 30 m), 100 km in width to the right of the satellite track with a nominal angle of 23° . The AMI in wave mode measured the change in reflectivity of the sea surface due to surface waves and provided information on wavelength and direction of wave systems. The **wind scatterometer** used three sideways looking antennae to measure radar backscatter from the sea surface for 50 km resolution overlapping cells. A mathematical model is used to compute surface wind vectors: speed and direction (ESA, 1993). The **radar altimeter** was a radar system looking straight down under the satellite and measure echoes from oceans and ice surfaces. It was used to derive information on wave height and sea surface elevation and/or on ice field topography. The **ATSR, Along Track Scanning Radiometer** had a thermal infrared radiometer to measure sea-surface and cloud-top temperatures over areas of approximately 50 by 50 km at an accuracy of 0.5 K.

The added instrument for ERS-2 was **GOME: Global Ozone Monitoring Experiment**. GOME was a nadir-viewing spectrometer which observed solar radiation (240 to 790 nm with a spectral resolution of 0.2-0.4 nm) transmitted through or scattered from the earth's atmosphere (stratosphere). The recorded spectra were used to derive information on the atmosphere's content on ozone, nitrogen oxide, water vapour and other trace gases. This instrument was not designed to monitor the earth's surface, therefore it used spectral regions outside the atmospheric windows to collect information on the gases atmosphere using absorption spectra. A more advanced version of GOME was SCIAMACHY on board EnviSat.

Other radar satellites were/are the Canadian Radarsat-1 and -2, the Japanese JERS-1, the Russian Almaz-1, and the joint US-Japan TRMM (Tropical Rainfall Monitoring Mission). TRMM was developed to monitor tropical rainfall and employed the (then) innovative Precipitation Radar, which could provide three-dimensional maps of storm structure. TRMM also carried the TMI (TRMM Microwave Imager): a passive microwave sensor to provide quantitative rainfall information, the VIRS (Visible and Infrared Scanner) for delineating storms and serve as a transfer standard to other measurements, CERES (Clouds and the Earth's Radiant Energy Sensor), which measured the energy at the top of the atmosphere and estimated energy levels within the atmosphere and at the Earth's surface and LIS (Light Imaging Sensor), used to detect and locate lightning (trmm.gsfc.nasa.gov). TRMM had a design lifetime of 3 years but

lasted much longer, providing valuable data for 17 years. The mission officially came to an end 15 April 2015.

Sentinel-1 SAR

The first in the series of Sentinel Satellites discussed in chapter 2, carries an advanced radar instrument to provide an all-weather, day-and-night supply of imagery of Earth's surface. The C-band Synthetic Aperture Radar (SAR) builds on ESA's and Canada's heritage SAR systems on ERS-1, ERS-2, Envisat and Radarsat. It has 4 operational modes:

- Interferometric wide-swath mode at 250 km and 5x20 m resolution
- Wave mode images of 20x20 km and 5x5 m resolution (at 100 km intervals)
- Strip map mode at 80 km swath and 5x5 m resolution
- Extra wide-swath mode of 400km and 20x40m resolution

As soon as 1-B is also in orbit, the mission, as a constellation of two satellites orbiting 180° apart, images the entire Earth every six days (ESA).

The goal of the mission is to continue where the ERS-2 and Envisat missions left off, by providing C-band SAR data. This data provides medium and high resolution imaging, day and night and in all weather conditions, and can be used detect small movement on the ground. This makes it useful for land and sea monitoring.

SMOS (Soil Moisture and Ocean Salinity) and SMAP (Soil Moisture Active Passive)

SMOS (ESA) and SMAP (NASA) are both radar based missions developed to monitor top soil moisture content and (in the case of SMOS) ocean salinity.

They differ from ERS in that they make use of **passive** microwave remote sensing. SMOS is a completely passive system, while SMAP combines both active and passive.

SMOS's main instrument is the Microwave Imaging Radiometer using Aperture Synthesis (MIRAS). It can register the faint microwave emissions from the Earth's surface to map soil moisture and ocean salinity (earth.esa.int). The emissivity of soil and water decreases with increasing moisture and salinity content. Ocean salinity is measured in practical salinity units (psu) and averages about 35 psu. From space, SMOS aims to observe salinity down to 0.1 psu (averaged over 10-30 days and an area of 200 km x 200 km) - which is about the same as detecting 0.1 gram of salt in a litre of water. The accuracy of a single observation is 0.5-1.5 psu (eart.esa.int) .Regarding soil moisture, SMOS can measure as little as 4% moisture in soil on the surface of the Earth. This is about equals being able to detect less than one teaspoonful of water mixed into a handful of dry soil (earth.esa.int). The spatial resolution of each measurement is 35-50 km and SMOS's revisit time is 1-3 days.

SMAP's radiometer also has a 4% accuracy in top soil moisture. However, by combining the passive measurement with an active SAR measurement the spatial resolution of each measurement can be increased to 10 km (smap.jpl.nasa.gov)

The frequency of the emissions in question are in the L- band (21 cm - 1.4 GHz). By international agreement this frequency has been set aside for the sole use of instruments that involve only a receiver. No transmission is allowed in this microwave region. However, in practice, there are some sources of emissions in this frequency causing distortions in the SMOS imagery. These distortion are referred to as RFI: Radio Frequency Interference, a well-known problem in the use of soil moisture mapping using passive radar technology (Wanders et al., 2012).

For more information regarding both missions visit:

<https://earth.esa.int/web/guest/missions/esa-operational-eo-missions/smso> or

<http://smap.jpl.nasa.gov/mission/description/>.

ASCAT: Advanced Scatterometer

The Advanced SCATterometer is the successor of the wind scatterometer on board ERS-1 and ERS-2. It is a real aperture radar, operating at 5.255 GHz (C-band). Its main objective is to measure wind speed and direction over the oceans. From around 837 km altitude, the instrument transmits well characterised pulses of microwave energy towards the sea surface. Winds over the sea cause small scale (centimetre) disturbances of the sea surface which modify its radar backscattering characteristics in a particular way. These backscattering properties are well known and are dependent on both the wind speed over the sea and the direction of the wind in relation to the point from which the sea surface is observed (www.eumetsat.int). Thus, both speed and direction can be determined.

On board ASCAT, two sets of three antennas measure the electromagnetic backscatter from the wind-roughened ocean surface (figure 3.13), in two 500 km wide swaths, on each side of the satellite ground track. The three antennas on each side are make observations in three directions, which are needed to resolve any ambiguity in wind direction (www.eumetsat.int). The instrument was developed under ESA/EUMETSAT contract by Airbus Defence and Space (formerly EADS Astrium).

Like SMOS and SMAP, ASCAT can also be applied in soil moisture studies. Contrary to SMOS, it uses active microwave remote sensing to determine soil moisture content. By means of a change detection method it can provide data in terms of soil moisture content relative to the wettest and driest conditions measured during ASCAT's lifetime (Wanders et al., 2012). The University of Vienna has a data-portal where you can view RS soil moisture products by ASCAT and other systems (<http://rs.geo.tuwien.ac.at/data-viewers/>).

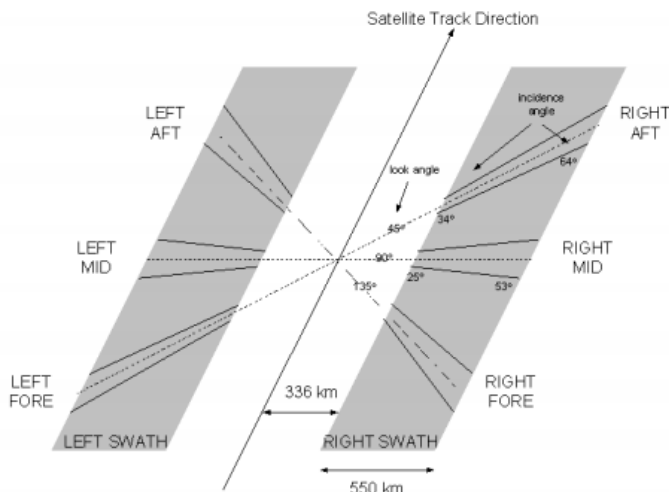


Figure 4-1: ASCAT swath geometry for a Metop minimum orbit height (822 km)

Figure 3.14: ASCAT swath geometry for an orbit height of 822 km ([eumetsat: ASCAT product guide](http://www.eumetsat.int)).

3.9 RADAR Interferometry

Radar interferometry is a fast developing technique for measuring the topography and the deformation of the Earth surface (Hansen 2001). SAR observations are made using a monochromatic radar signal i.e. one frequency. The time that the return signal arrives at the sensor provides the travel time of the signal and hence the distance to the Earth surface. If we now have two observations from two orbits at distance B apart and we compute the shift in phase of the return signal it is possible to derive an digital

elevation model or DEM from Radar images. Radar observations collected over time make it possible to detect deformations of the Earth surface caused by Earthquakes or volcanic eruptions (figure 3.14). An example is shown in figure 3.15. A somewhat more everyday use of InSAR is to monitor ground subsidence in urban areas with millimetre accuracy. Information about the rate and quantity of subsidence can be used by utility (gas, water, electricity) companies to keep track of the need to replace pipelines or cables. Subsidence or displacement of railroad lines, bridges or reservoirs can be tracked in the same way. In the Netherlands, InSAR can be of great import for the of dykes (figure 3.16).

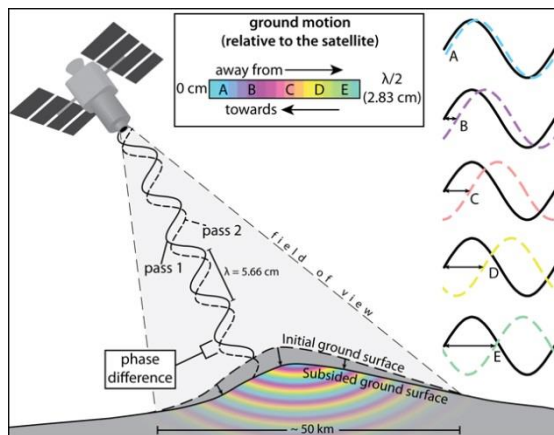


Figure 3.15: Principle of InSAR (volcano.si.edu).

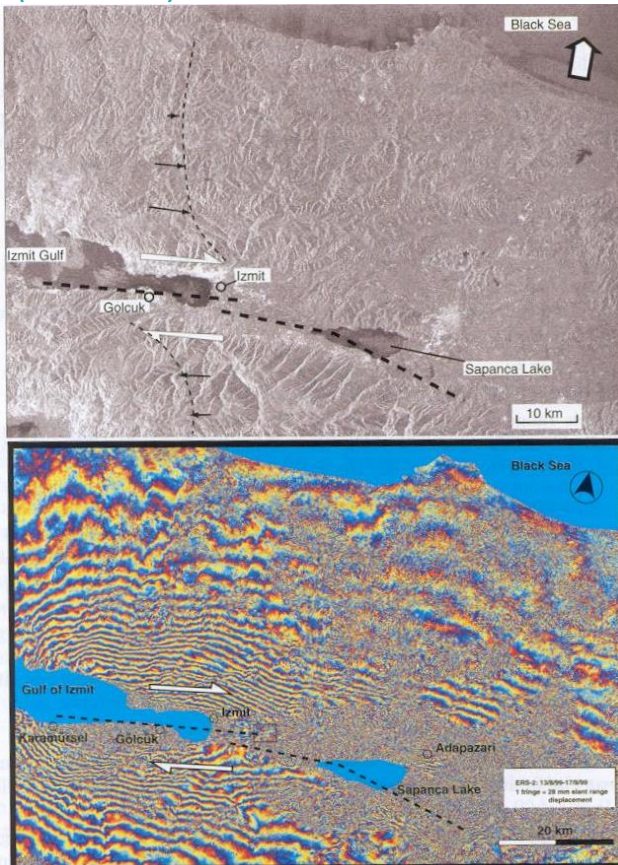


Figure 3.16: A) Radar intensity map of northern Turkey near Izmit and the Black Sea. B) Interferogram constructed of two radar images of 13 August 1999 and 17 September 1999 showing the deformation pattern due to the Izmit earthquake at 17 August 1999 ([Hansen, 2001](#)).

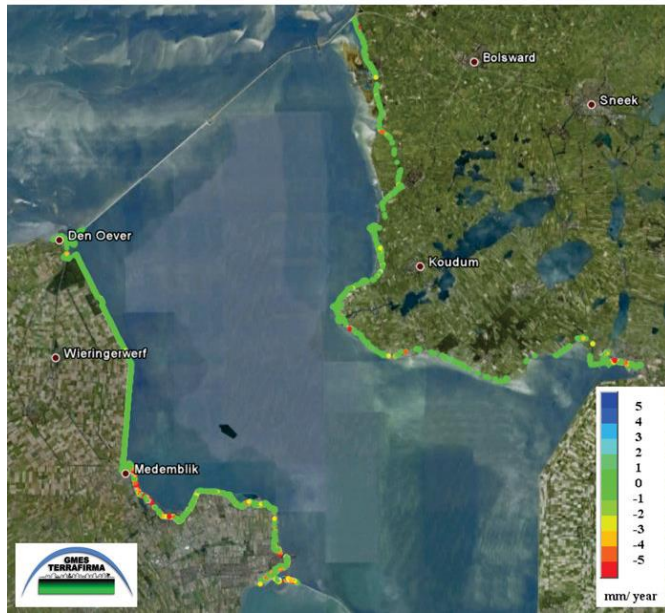


Figure 3.17: Dyke displacement (www.esa.int, www.hansjebrinker.com).

3.10 Other satellites: GOCE & GRACE

GOCE (Gravity field and steady state Ocean Circulation Explorer) from ESA and GRACE (Gravity Recovery and Climate Experiment) from NASA are both developed to monitor and map the Earth's gravity field, but they operate in different ways.

GOCE, launched March 2009, measured variations in the Earth's gravity field (the value of 'g'), resulting in a 'geoid' model of the Earth: the surface of equal gravitational potential defined by the gravity field (figure 3.17). This was then used to derive information about ocean circulation and sea level change and to understand more about processes occurring inside Earth and for use in practical applications such as surveying and levelling. In addition, the measurements are being used to improve estimates of polar ice-sheet thickness and their movement (ESA). The accuracy of the geoid was 1 - 2 cm vertically with 100 km spatial resolution. The satellite orbited Earth as low as possible to observe the strongest possible gravity-field signal – hence GOCE was designed to skim the edge of Earth's atmosphere at a height of about 250 km (ESA).

GOCE's main instrument was the Electrostatic Gravity Gradiometer (EGG), a set of six 3-axis accelerometers mounted in a diamond configuration in an extremely stable structure. Each accelerometer pair formed a 'gradiometer arm' 50 cm long, with the difference in gravitational pull measured between the two ends. Three arms were mounted orthogonally: along-track, cross-track and vertically (figure 3.18). The gradiometer measured gravity gradients in all directions. It was specifically designed for the stationary gravity field. For instance, GOCE data has been used to map the Moho-depth everywhere on Earth (figure 3.19).

On 21 October 2013, the GOCE mission came to a 'natural' end when it ran out of fuel. Three weeks later, on 11 November, the satellite disintegrated in the lower atmosphere.

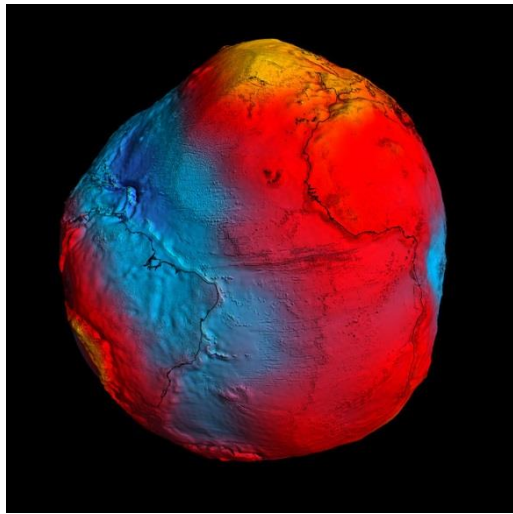


Figure 3.18: GOCE-derived geoid (www.esa.int).

GRACE, launched March 2002, also maps the Earth's gravity field, but in a different way. GRACE consists of two identical spacecraft that fly about 220 kilometers apart in a polar orbit 500 kilometers (310 miles) above Earth. GRACE maps Earth's gravity field by measuring the distance between the two satellites using GPS and a microwave ranging system (NASA). As the pair circles the Earth, areas of slightly stronger gravity will affect the lead satellite first, pulling it away from the trailing satellite, then as the satellites continue along their orbital path, the trailing satellite is pulled toward the lead satellite as it passes over the gravity anomaly. A highly accurate measuring device known as an accelerometer, located at each satellite mass center, will be used to measure the non-gravitational accelerations (such as those due to atmospheric drag) so that only accelerations caused by gravity are considered. The gravity variations studied by GRACE include: changes due to surface and deep currents in the ocean; runoff and ground water storage on land masses; exchanges between ice sheets or glaciers and the ocean; and variations of mass within Earth (NASA). GRACE is also sensitive to permanent changes in the gravity field due to earthquakes. For instance, GRACE data have been used to analyze the shifts in the Earth's crust caused by the earthquake that created the 2004 Indian Ocean tsunami (Wikipedia).

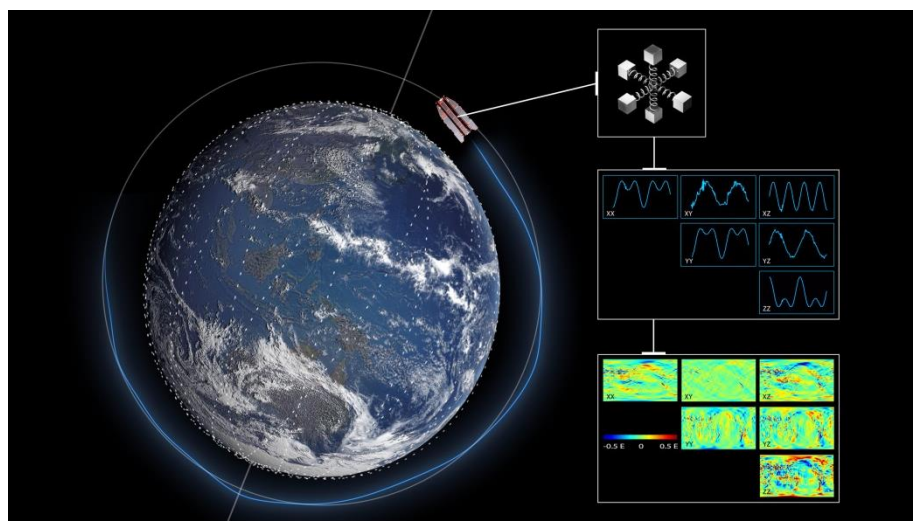


Figure 3.19: Representation of how the GOCE gradiometer works (<http://www.goce-projektbuero.de/>).

Designed for a nominal mission lifetime of five years, GRACE is currently operating in an extended mission phase, which is expected to continue through at least 2015.

For more information, visit:

http://www.esa.int/Our_Activities/Observing_the_Earth/GOCE/Introducing_GOCE or

http://www.nasa.gov/mission_pages/Grace/#.Vh1pcPntIBc.

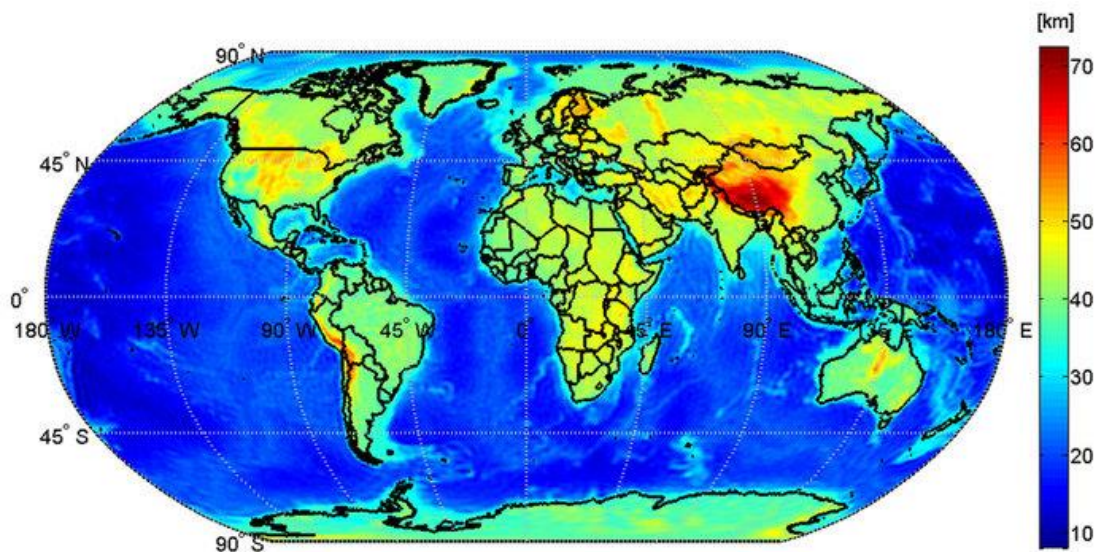


Figure 3.19 : Global Mohorovičić discontinuity depth based on data from the GOCE satellite. The Moho is the boundary between the crust and the mantle, ranging from about 70 km in depth in mountainous areas, like the Himalayas, to 10 km beneath the ocean floor (www.esa.int).

4. Thermal Infrared Remote Sensing

4.1 Introduction

All matter radiates energy at thermal infrared wavelengths (3.0-15.0 μm). We cannot see this radiation because the human eye is only sensitive for radiation in the visible part of the spectrum (0.4-0.65 μm) and not for the thermal part. The emitted radiation can theoretically be computed using the Stefan Boltzmann equation described in chapter 1 and shown in figure 1.4. Unfortunately, this relation is only valid for black bodies in ideal situations. The real world of thermal remote sensing is a bit more complex as will be discussed in this chapter.

4.2 Temperature and Emissivity

The temperature of an object is normally measured by putting a thermometer in direct contact with or even in the object. The temperature measured using this method is called kinetic or internal temperature: T_{kin} . In fact, the kinetic energy of the particles of matter (molecules) is determined. The random motion causes particles to collide, resulting in changes of the energy state (of e.g. the electrons) and the emission of electromagnetic radiation. The amount of energy radiated from an object is called radiant flux and is measured in watts per square centimetre. The concentration of the radiant flux of an object is the radiant temperature: T_{rad} . Important: kinetic temperature and radiant temperature are not the same! The radiant temperature is always less than the kinetic temperature because objects do not behave like black bodies and do not completely obey the Stefan Boltzman equation. This property of objects is called emissivity and is defined as the ratio between the radiant flux of the object and the radiant flux of a blackbody with the same (kinetic) temperature. Water is very close to behaving as a blackbody, Quartz act as a selective radiator its radiation varies with wavelength (figure 4.1 and 4.2). Emissivity values for some objects are:

Pure water	0.993
Wet soil	0.950
Dry soil	0.920
Sand, quartz	0.914
Wood	0.900
Granite	0.815
Polished aluminium	0.060

4.3 Heat transfer

Heat energy is transferred from one place to another by three mechanisms: conduction, convection and radiation:

Conduction transfers heat through material by molecular contact. Heat transfer through a frying pan for cooking is an example.

Convection transfers heat through the physical movement of heated matter. The circulation of heated water and air are examples of convection.

Radiation transfers heat in the form of electromagnetic waves. Heat from the sun reaches the earth by radiation. In contrast to conduction and convection, which can only transfer heat through matter, radiation can transfer heat through a vacuum.

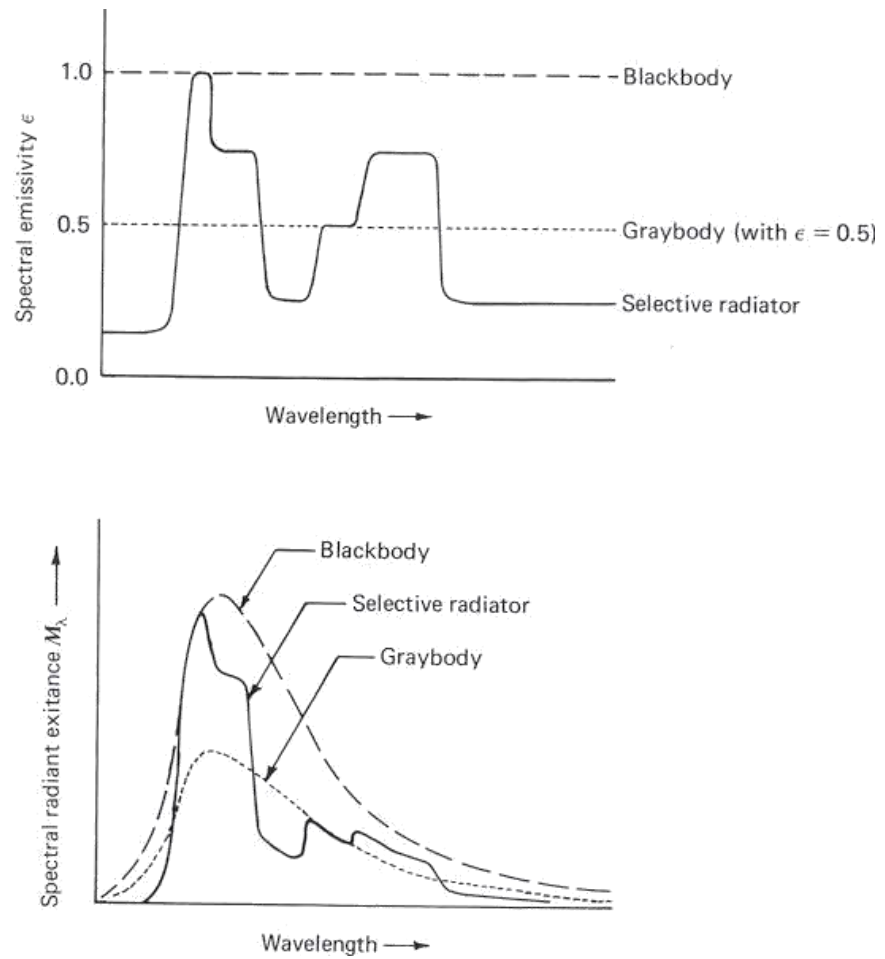
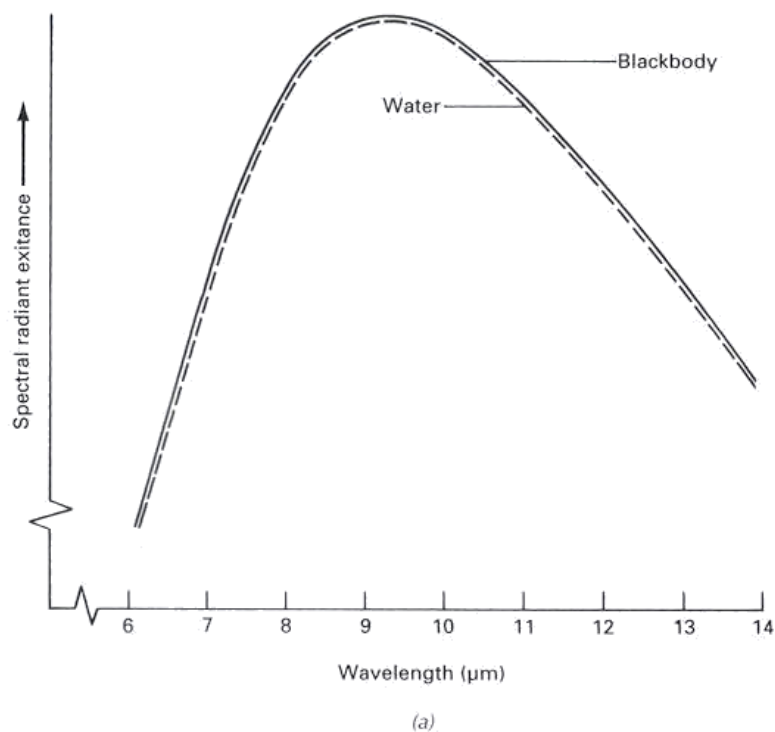


Figure 4.1: Spectral emissivities and radiant exitances for a blackbody, a grey body and a selective radiator (Lillesand and Kiefer, 1994).

Objects at the surface of the earth receive thermal energy mainly by radiation from the sun. There are daily (24 hours) and annually (1 year) cyclic variations in the duration and intensity of the solar energy and hence, in the energy received.

Atmospheric transmission

In the previous chapters it was already discussed that the atmosphere does not transmit radiation in the optical wavelengths equally throughout the spectrum. The same is true for the thermal infrared part of the spectrum. Carbon dioxide (CO_2), ozone (O_3) and water vapour (H_2O) absorb energy at certain wavelengths in the thermal bands. Two important atmospheric windows are distinguished in the thermal part of the spectrum: 3 to 5 μm and 8 to 14 μm (figure 4.3).



(a)

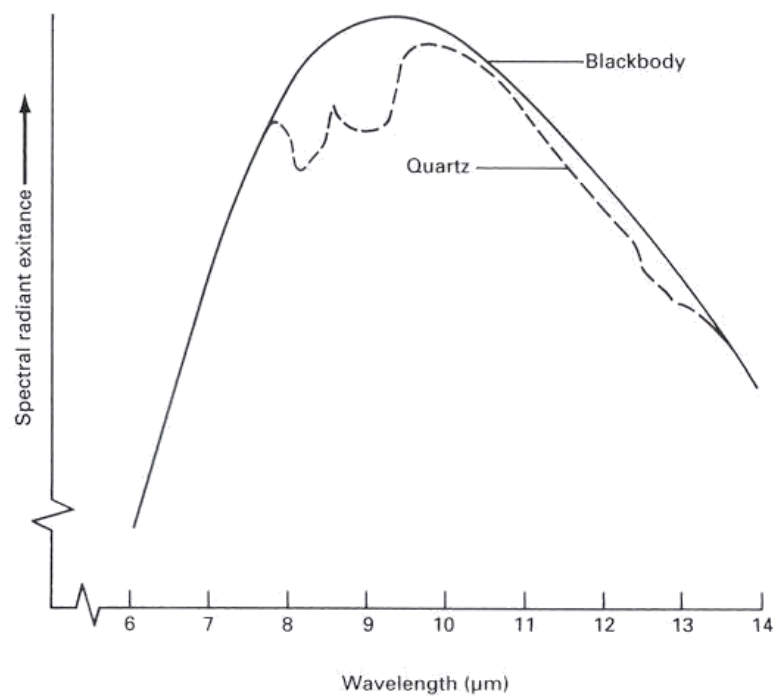


Figure 4.2: Spectral radiance for water (a) versus a blackbody and (b) quartz versus a blackbody (Lillesand and Kiefer, 1994).

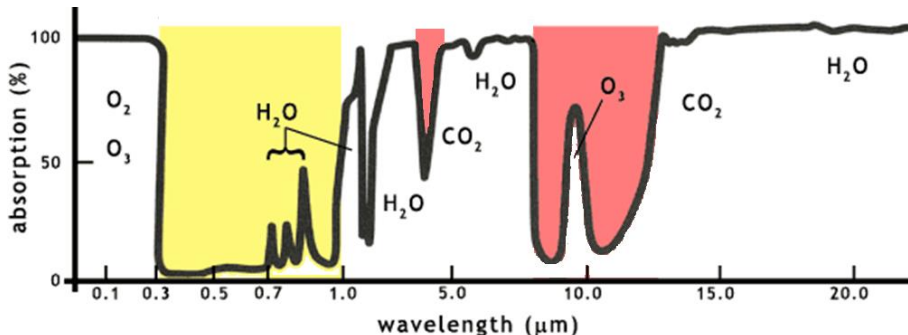


Figure 4.3: Electromagnetic spectrum showing atmospheric absorption and remote sensing windows. Gasses responsible for atmospheric absorption are indicated. Two thermal atmospheric windows are visible in red: 3 to 5 μm and 8 to 14 μm . The solar emission range is indicated in yellow (*adapted from www.helpsavetheclimate.com*).

4.4 Thermal properties of Materials

Radiant energy striking the surface of an object at the earth surface is theoretically partly reflected, partly absorbed and partly transmitted through the material. Consequently, a theoretical balance can be defined as:

$$\text{reflectivity} + \text{absorptivity} + \text{transmissivity} = 1$$

Reflectivity, absorptivity and transmissivity are determined by properties of the material and vary with wavelength of the incident radiation and with the temperature of the surface. For many materials, transmissivity is negligible and the previous equation reduces to (except a glass window for which transmissivity is fairly large):

$$\text{reflectivity} + \text{absorptivity} = 1$$

The absorbed energy causes an increase in the kinetic temperature of the material. For the theoretical, ideal case of a blackbody absorptivity is 1.

To understand the thermal behaviour of objects at the surface of the earth and hence, to interpret correctly thermal images four thermal properties of materials are important:

- thermal conductivity
- thermal capacity
- thermal inertia
- thermal diffusivity.

Thermal conductivity (K) refers to the rate at which heat will pass through a material and is expressed as $\text{W}/\text{m}^* \text{K}$ (or as $\text{cal}/\text{cm}^* \text{sec}^* \text{C}$). It is the amount of energy that will pass through a 1 cm cube of the material in 1 second when the two opposite faces are maintained at 1°C difference in temperature. Rocks and soils are relatively poor conductors of heat.

Thermal capacity (c) is the ability of a material to store heat. Thermal capacity is defined as the amount of calories required to raise the temperature of 1 g of a material by 1°C and is expressed in calories per gram per °C. The thermal capacity of water is large. Consequently, much energy is needed to heat water one degree and it takes a lot of sunny days in spring to heat the swimming water. The thermal capacity of beach sand is pretty low. Hence, you can already burn your feet after one clear, sunny summer day.

Thermal inertia (P) is a measure of the thermal response of a material to temperature changes and is expressed in $\text{cal/cm}^2 \cdot \text{sec}^{1/2} \cdot ^\circ\text{C}$. Thermal inertia is a function of thermal conductivity (K), thermal capacity (c) and the density (ρ) of the material and hence, thermal inertia is defined as:

$$P = (K\rho c)^{1/2}$$

The density of the material is a very important property to determine the thermal inertia. Figure 4.4 illustrates the effect of differences in thermal inertia on surface temperatures. Thermal inertia cannot be determined by remote sensing methods because conductivity, density and thermal capacity must be measured by contact methods. Maximum and minimum radiant temperature however, may be measured from daytime and night-time images. The measured temperature difference (ΔT) will be low for materials with high thermal inertia and vice versa. Using these temperature differences a property called apparent thermal inertia or ATI can be derived:

$$ATI = \frac{1 - \text{albedo}}{\Delta T}$$

A correction for the albedo is necessary to compensate for the effects that differences in absorptivity have on radiant temperature. Dark objects absorb more sunlight during the day than light materials. ATI values should be interpreted with caution because other factors than thermal inertia may influence ΔT (shadow sites or sun-exposed sites, active evapotranspiration of vegetation, changes in the water content during subsequent observations etc.).

Thermal diffusivity (k) refers to the ability of a material to transfer solar heating from the surface to the interior during daytime and at night, during a period of cooling, from the interior to the surface. It is defined as the ratio between the thermal conductivity and the thermal capacity times the density.

Table 4.1: Kinetic versus radiant temperature for four material types.

		Kinetic Temperature T_{kin}		Radiant Temperature $T_{\text{rad}} = \epsilon^{1/4} T_{\text{kin}}$	
Object	Emissivity ϵ	K	°C	K	°C
Blackbody	1	300	27	300	27
Vegetation	0.98	300	27	298.5	25.5
Wet soil	0.95	300	27	296.2	23.2
Dry soil	0.92	300	27	293.8	20.8

4.5 Thermal sensors

Thermal sensors used to record thermal images are often aboard aircrafts. Commercial applications of thermal imagery are the detection of heat losses from houses, buildings and factories and the survey of hot spots of buried pipelines that may indicate leakages. Furthermore, thermal images are used to survey evapotranspiration and to map geologic formation with different thermal properties. A number of satellites have also thermal scanners aboard. The Landsat TM has a thermal infrared scanner (10.4-12.5 μm) with a spatial resolution of 120 m. It is used for soil moisture mapping and evapotranspiration survey. The Enhanced Thematic Mapper (ETM+) of Landsat 7 carries a thermal infrared scanner with a spatial resolution of 60 m. NOAA-AVHRR has thermal infrared scanners in the two thermal atmospheric windows (3.55-3.93 μm and 10.5-11.5 μm) with a ground resolution at nadir of 1.1 km to measure top-cloud temperature and seawater temperatures.

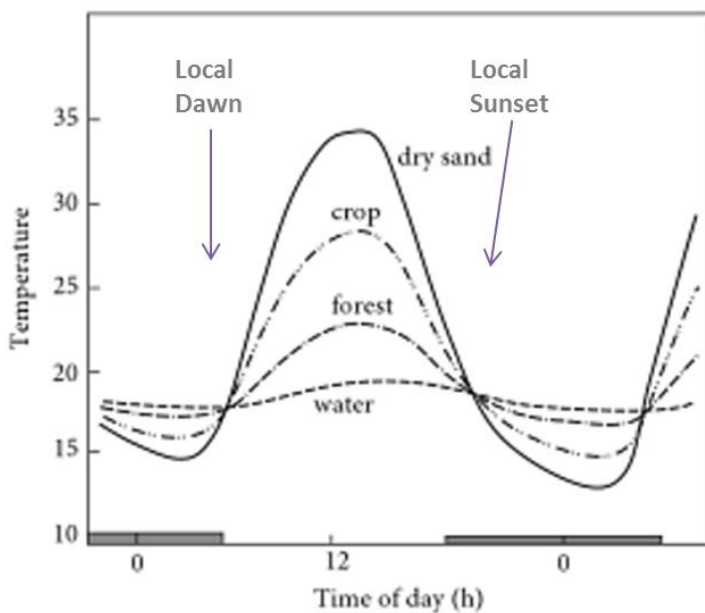


Figure 4.4: Schematic diagram showing the effect of differences in thermal inertia on surface temperature during diurnal solar cycles.

4.6 Heat Capacity Mapping Mission: HCMM

The data of the HCMM were intended initially for conversion to thermal inertia mapping of geological features. However, the images were also applied for vegetation survey and evapotranspiration mapping (Curran, 1985; Galli de Paratesi & Reiniger, 1987). The HCMM satellite contained a scanning radiometer in visible and near infrared (0.55-1.10 μm) and a thermal infrared waveband (10.5-12.5 μm) with a ground resolution of 600 m to 1 km (depending on the viewing angle). The orbits of the satellite were arranged to ensure that images (of the United States and Europe) were obtained during times of maximum and minimum surface temperature (near 1:30 p.m. and 2:30 a.m.). The HCMM-satellite was launched in April 1978 and lasted until end 1980. Examples and a detailed description of HCMM can be found in Sabins (1987) and Galli de Paratesi & Reiniger (1987).

4.7 Interpretation of thermal infrared images

On most thermal infrared images the brightest tones represent the warmest radiant (!) temperatures and the darkest tones represents the coolest temperatures. However be careful: as you will notice during the exercise, image processing techniques allow you to give every colour or grey tone to any digital number (reflectance value or temperature) in an digital image.

Clouds typically have a patchy warm and cool pattern and scattered rain showers produce a pattern of streaks. A heavy overcast layer reduces thermal contrast between terrain objects because of re-radiation of energy between the terrain and the cloud cover. Clouds consist of tiny divided particles of ice and water that have the same temperature as the surrounding air. Energy radiated from the earth surface does not penetrate clouds but is absorbed and reradiated. Smoke plumes in contrast, consist of ash particles and other combustion products so fine that they are penetrated by long wavelengths of thermal radiation. Furthermore, smoke plumes are most often warmer than clouds.

Thermal images of vegetation should be interpreted with care because evapotranspiration from vegetation is an active process controlled by the vegetation or crop itself. During the day, transpiration of water lowers the leaf temperature, causing vegetation to have a cool signature relative to the surrounding soil (figure 4.5). At night the insulating effect of leafy foliage and the high water content

retain heat, which results in warm night-time temperatures. Consequently, if there is a water shortage for the vegetation, it cannot evaporate and its temperature will rise.

The energy balance of the Earth's surface forms the basis of interpretation of thermal images. The energy balance of bare soil, rock and vegetated surfaces makes it possible to model the thermal behaviour which helps to interpret images. In the same way, thermal images are useful to set up the thermal balance of a surface. The heat balance of the earth's surface can be described in terms of incoming and outgoing fluxes:

$$Q = LE + H + G$$

Q: Net radiation [Wm^{-2}];

LE: Latent heat flux [Wm^{-2}];

H: Sensible heat flux [Wm^{-2}];

G: Heat flux into the soil [Wm^{-2}].

The term Q consists of a short-wave and a long wave component. The short-wave component is the energy radiated by the sun, long wave radiation is emitted by the objects at the surface. Q can be described as (Jackson, 1985):

$$Q = (1 - \alpha)R_s + \varepsilon(R_l - \sigma T_s^4)$$

α : Albedo;

R_s : Short-wave incoming radiation flux [Wm^{-2}];

R_l : Long wave sky radiation flux [Wm^{-2}];

ε : Emission coefficient;

σ : Stefan Boltzmann constant [$5.67 \times 10^{-8} \text{ Wm}^{-2}\text{K}^4$];

T_s : Temperature of the surface [K].

Remote sensing imagery can be useful to estimate some of the components of the energy balance. Remote sensing is especially useful to assess the spatial and temporal variability of these variables. Albedo can be estimated from the visible and near infrared channels and surface temperature can be estimated from bands in either or both of the thermal atmospheric windows. Examples and detailed descriptions of surface energy balance studies can be found in Menenti (1993; 1984), Nieuwenhuis et al. (1985) and Nieuwenhuis (1993).

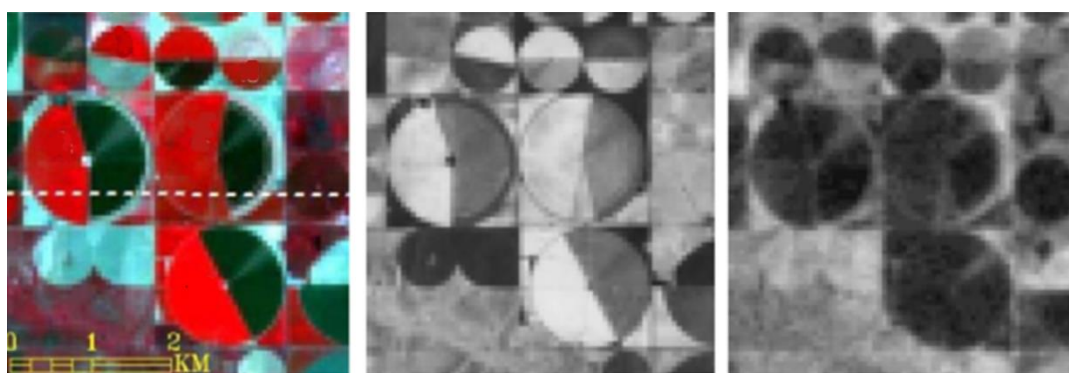


Figure 4.5: Colour infrared (left), NDVI (middle) and Thermal (right) image of pivot irrigated crops. Note that the NDVI shows high values for the vegetated areas, while in the Thermal image the vegetation has the lowest values (Gao et al., 2012).

5. Image Corrections and Analysis Techniques

5.1 Introduction

Many types of remotely sensed images (Landsat, SPOT, NOAA, ERS etc.) are recorded in digital form. A computer is needed to process these data. Moreover, a computer is very useful to process the large volume of data acquired by remote sensing systems. One Landsat TM scene, for example, consists of 7 spectral bands covering an area of 185 by 185 km with pixels of 30 by 30 m. The data volume in bytes can be computed as:

- number of pixels in one image line 185 km / 30 m = ± 6165 pixels;
- number of image lines: 185 km / 30 m = ± 6165 lines;
- 7 spectral bands (including the thermal band);

The total data volume is $6165 * 6165 * 7 = 266$ Megabytes. Processing by hand is virtually not possible. Often Landsat images are processed in quarter scenes. Quarter scenes cover an area of 90 by 90 km and their data volume is approximately 67 Mbytes, which can mostly be processed easily on image processing systems.

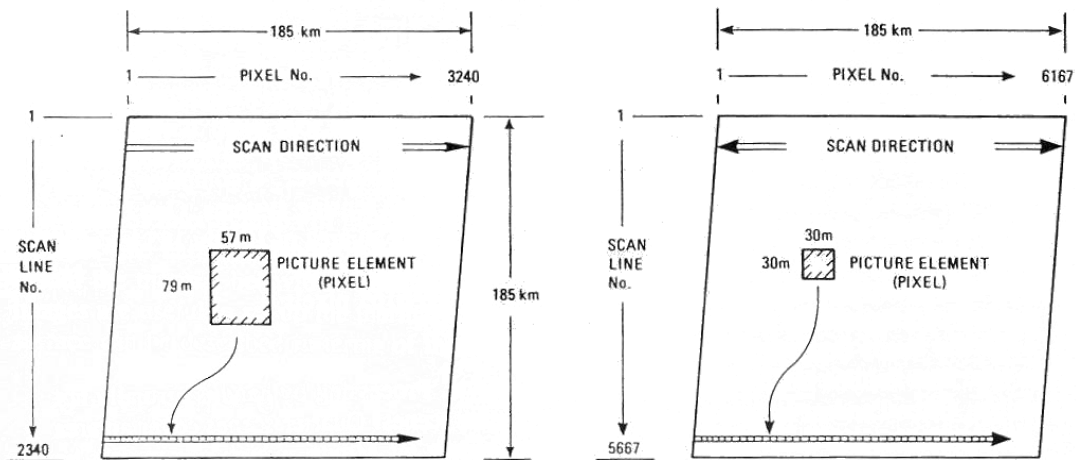
Image processing is defined as: 'digital techniques, consisting of a number of operations and modules as expedients to elucidate the information contents of images to the utmost' (an interactive approach of the data analysis and image interpretation is common practice). Hence, image processing comprises all manipulations of digital images such as geometric corrections, radiometric corrections, image enhancements, image filtering, data reduction techniques and image classifications. This chapter focuses mainly on processing of remote sensing images acquired in the optical wavelength such as Landsat TM, Landsat MSS and SPOT because environmentalists will mainly make use of these types of images.

5.2 Digital Image Structure

A digital recorded image consists virtually of a number of layers (or matrices) of numbers or digital numbers. The intensity value of a pixel (reflectance or thermal emission) is recorded as **digital number or DN**. Each layer represents a spectral band and each layer consists of a number of columns and rows (i.e. image lines). Each number per layer is the Digital Number (the measured radiance) per **picture element or pixel**.

The measured radiance is mostly stored as a byte (8 bits), values can vary from 0 to 255 and calibration data are needed to transfer them to reflectance or absolute radiance. Sometimes, digital recorded data are stored as 10 bits e.g. NOAA-AVHRR or 16 bits (words) e.g. AVIRIS. Landsat data are stored as a byte. A Landsat TM image consist of 7 layers or matrices (because it has 7 spectral channels) and it has approximately 6165 image lines with approximately 6165 pixels on each image line. Figure 5.1 and 5.2 illustrates the structure of an Landsat TM scene.

The structure of a digital recorded image is sometimes called an 'image cube'. The X- and Y-coordinates within the matrix of DN represent the position of each pixel in the field. The Z-coordinate represents the spectral position (1 to 7 for TM). As is already discussed, the spatial resolution of the thermal band of Landsat TM is 120 by 120 m. When it is stored in a digital form e.g. on **Computer Compatible Tape (CCT)** it is resampled to a pixel size of 30 by 30 m.



$2340 \text{ scan lines} \times 3240 \text{ pixels} = 7.6 \times 10^6 \text{ pixels per band}$
 $7.6 \times 10^6 \text{ pixels} \times 4 \text{ bands} = 30.4 \times 10^6 \text{ pixels per scene}$

A. MULTISPECTRAL SCANNER.

$5667 \text{ scan lines} \times 6167 \text{ pixels} = 34.9 \times 10^6 \text{ pixels per band}$
 $34.9 \times 10^6 \text{ pixels} \times 7 \text{ bands} = 244.3 \times 10^6 \text{ pixels per scene}$

B. THEMATIC MAPPER.

Figure 5.1: Arrangement of scan lines and pixels in Landsat MSS and TM images (Sabins, 1987).

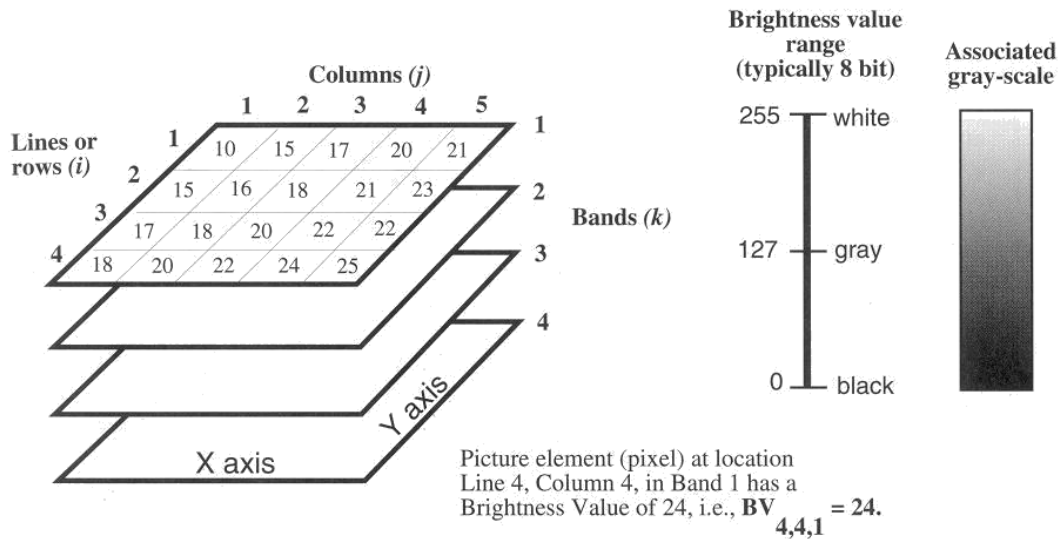


Figure 5.2: Digital structure of a Landsat TM image (left) and 8 bits radiometric resolution of the pixel values.

Line dropouts

As was already discussed in chapter 1, Landsat MSS and Landsat TM register(ed) radiance 6 lines at a time respectively 16 lines at a time. On some image data of one image line are missing due to (temporal) failure of one of the detectors. As a result every 6th or 16th line appear black. These lines are called periodic line dropouts. The data in these scan lines is lost. Most image processing systems try to correct these lines by averaging the line above and below the lost line.

Striping

Striping in an image refers to a regular pattern of (horizontal) stripes in an image. Most often these stripes are caused by a slight difference in calibration of the 6 (for MSS) or 16 (for TM) sensors. A slight difference in sensitivity of the sensors might cause 'striping patterns' in the image. The effect can play

an important role while sensing dark surfaces such as water bodies. Image enhancement e.g. by histogram stretch causes also enhancement of the striping. Striping deteriorates image classification and hampers image interpretation.

5.3 Radiometric Corrections

Radiometric correction is an image restoration operation. Image restoration techniques aim at compensating for errors, noise and distortion by scanning, transmission and recording images. Sources of radiometric distortion are the atmosphere and the instruments used to register the image data (Richards, 1986). Figure 5.3 shows the effect of the atmosphere on the measured brightness of one single pixel. The sun radiates directly electromagnetic to the pixel at a certain location but this pixel also receives scattered radiance from the sky (sky irradiance 1) and scattered radiance from neighbouring pixels (sky irradiance 2). The amount of scattering varies strongly in space and time and depends on the condition of the atmosphere (see also section on Rayleigh and Mie scatter). Remember that **Rayleigh and Mie scatter** are wavelength dependent and that their effects will be different in the different wavebands of a remote sensing system. The sensor measures radiance directly originated from the pixel (figure 5.3), but it also receives radiance scattered in the atmosphere (path radiance 1) and radiance reflected from neighbouring pixels (path radiance 2).

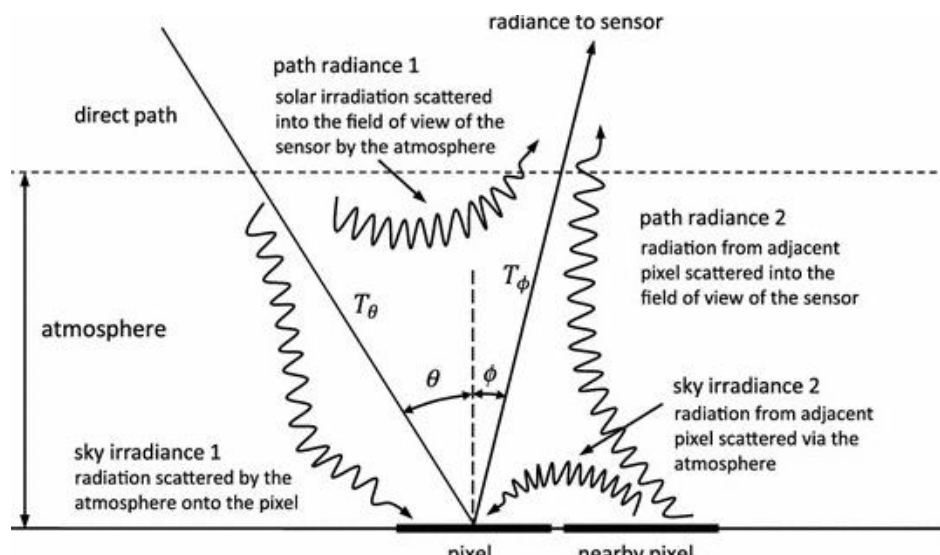


Figure 5.3: Effect of the atmosphere on the brightness of a pixel (Richards, 2012).

Radiometric errors can also be caused by the design and operation of the sensor system. The most significant of these errors is related to the detector system. An ideal radiation detector should have a linear transfer characteristic (i.e. radiation in \rightarrow signal out) as shown in figure 5.4. However, real detectors have some degree of non-linearity and will give a small signal out even when no radiation is detected: dark current, or the offset in figure 5.4. The slope of the characteristic is called transfer gain or gain. Consequently, two steps are generally necessary for radiometric correction 1) correction for gain and offset of the detector and 2) correction for the atmospheric conditions at the time of data acquisition.

Spaceborne and airborne remote sensing images can be delivered in various units (Chander et al. 2009):

- 1) **Raw Digital Numbers (DN)**, these are uncalibrated pixel values where you only have relative information about different reflectance or emission of objects in the image.

- 2) **Radiance**, the pixel values present by the sensor registered incoming electromagnetic radiance in units of watts per square meter per steradian per micrometer i.e. $\text{W/m}^2/\text{ster}/\mu\text{m}$. As shown in the figure radiance is the radiant flux per unit solid angle Ω or steradian leaving a source in a given direction per unit-projected area A . The ASTER image is available in radiance.
- 3) **Reflectance**, the pixel values in the image give the ratio between incoming radiance (mostly from the sun) and the radiance registered by the sensor. This ratio has no units. Reflectance is most widely used and in the literature you will normally find reflectance spectra of objects.
- So, if you use remote sensing images, it is very important to know in what (physical) units the pixels present their information.

Often, images are radiometrically corrected/calibrated using specific formulas. The radiometric correction process can be divided into two important steps:

1. **DN to radiance to TOA reflectance**. If you have type 1 data (i.e. DN), a correction for the sensitivity of the sensor is required into radiance. Normally pre-launch calibration values or on-board calibration values are used for this process. These calibration values tell you to what radiance values the DN values (0 to 255 or 0 to 1023) correspond. If you have type 2 data (radiance) available, you have to convert radiance into reflectance. This is **Top of Atmosphere (TOA)** reflectance, so not yet the reflectance at the surface!
2. **Atmospheric correction** for the conditions at the time of data acquisition. Atmospheric correction aims at correcting for distortion in the atmosphere of the measured radiance by aerosols, moisture, gasses etc. Advanced radiative transfer models or empirical approaches can be used for atmospheric correction of images.

For the first step two equations are required. Equation 2 gives the relation between the DN coming from the sensor and radiance in $\text{W/m}^2/\text{ster}/\mu\text{m}$. Equation 1 computes the ratio of radiance measured at the sensor entrance and the incoming solar radiance:

$$R(\lambda) = \frac{\pi L(\lambda)}{E_0(\lambda) \left(\frac{1}{r^2}\right) \cos(\theta_0)} \quad (1)$$

Where λ is the spectral band and the radiance, $L(\lambda)$, is determined for each sensor band by:

$$L(\lambda) = G \times DN + B \quad (2)$$

- E_0 : is the solar constant in the bandpass of the sensor (Wolfe & Zisis, 1993);
- r : is the normalized Earth - Sun distance (in astronomical units ~ 1.0);
- θ_0 : is the solar zenith angle at the image centre (i.e. seasonal position of the sun);
- π : 3.14159265;
- DN : is the digital count (DN) in the specific spectral sensor band;
- G : is the calibration slope for the specific sensor band (channel gain);
- B : is the calibration offset for zero radiance for that sensor band (bias or channel offset).

The solar constant can be derived from the Infrared Handbook (Wolfe & Zisis, 1993) or other lookup tables. For the Landsat ETM+ bands the solar constant is given per band:

Table 5.1: Solar Constant Lookup-table for Landsat ETM+ (nasa.gov), Note that the ETM+ thermal band (6) is excluded.

Band	Solar constant (W/m ² /ster/μm)
1	1970
2	1842
3	1547
4	1044
5	225.7
7	82.06
PAN	1369

There are also other approach to radiometric correction available: if sufficient measurements of the conditions of the atmosphere such as optical thickness, scattering and sun elevation are available, and if the surface reflectance of several dark and bright targets in the study area are determined, then the image can be radiometrically corrected using models such as the 5S code, LOWTRAN or ATCOR. A detailed description of the atmospheric effect on remote sensing imagery is provided by Kaufman (1989), Kaufman and Sendra (1988), Richards (1986) and Lillesand et al. 2015. Model descriptions of LOWTRAN and 5S-code are available from Kneizys et al. (1988) and Tanré et al. (1985).

A bulk correction method for atmospheric effects is called the histogram method or darkest pixel method or haze removal. This technique is based on the fact that the near infrared spectral band (Landsat MSS band 7 or Landsat TM band 4) is essentially free of atmospheric effects (figure 5.5). This can be verified by examining DN-values of clear water and shadows. Their DN values should be close to zero. The assumption of this technique is that atmospheric scattering has added a constant value to each pixel in a band. Hence, the lowest value in the histogram of each band is subtracted from all pixels in that specific band (figure 5.6).

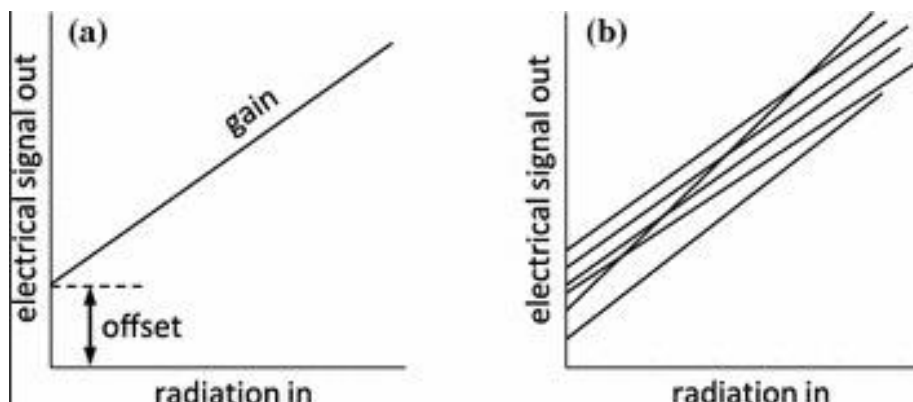


Figure 5.4: a) Transfer characteristic of a radiation detector: gain and offset and b) Hypothetical mismatches in detector characteristics (Richards, 2012).

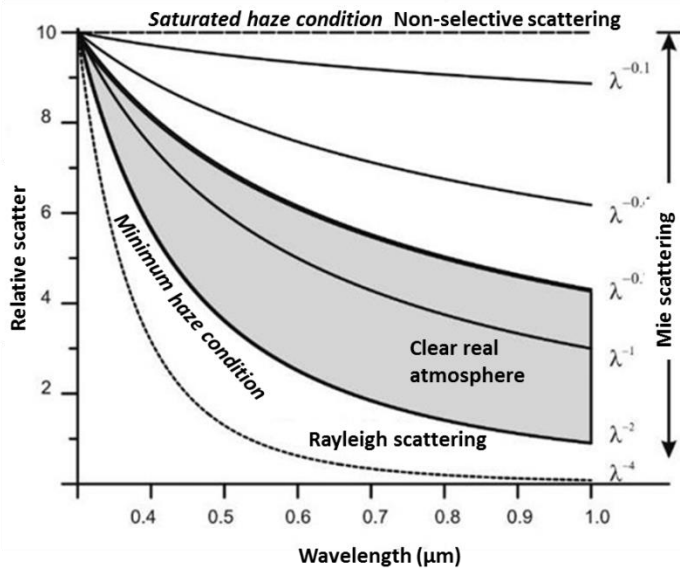


Figure 5.5: Relative scatter as a function of wavelength for various levels of atmospheric haze (Adapted from: Sabins, 1987).

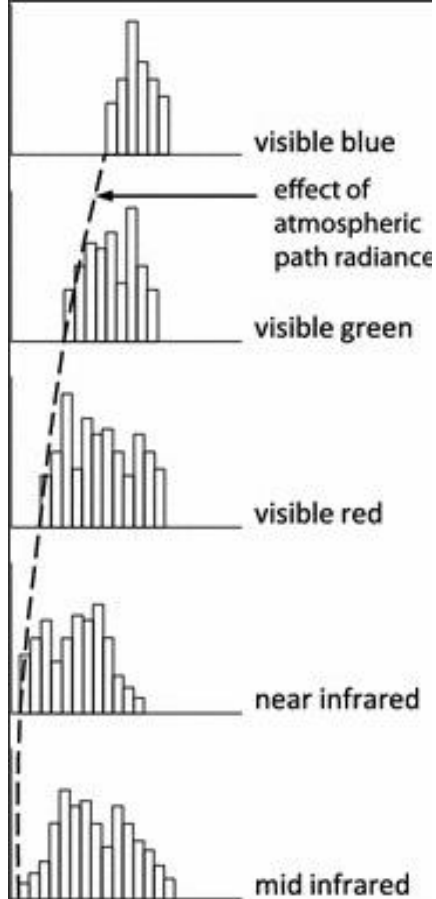


Figure 5.6: Illustration of the effect of path radiance resulting from atmospheric scattering (Richards, 2012).

5.4 Geometric Corrections

There are many potential sources of geometric distortions of remotely sensed images (Richards, 1986):

1. the rotation of the earth during image acquisition;
2. the finite scan rate of some sensors;
3. the wide field of view of some sensors;
4. the curvature of the earth;
5. sensor non-idealities;
6. variations in platform altitude, attitude and velocity;
7. panoramic effects related to imaging geometry;
8. An inclination of the satellite required to obtain a full earth coverage (see ch.2: orbits).

Point 3 is especially important for satellites such as NOAA-AVHRR with a large swath width (2700 k).

Point 6 is not very important for satellite systems because their movements are rather stationary. For aircrafts, however, these effects can be very large. Figure 5.7 shows the 6 potential variations of aircraft motion and figure 5.8 their effect upon an image.

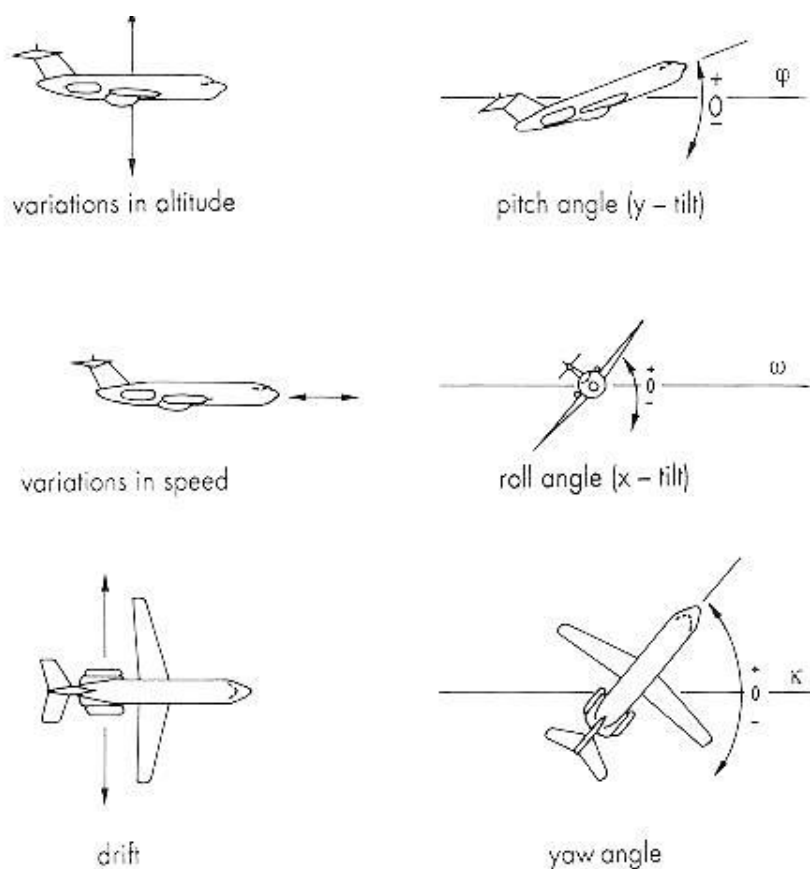


Figure 5.7: The six most important flight parameters of an aircraft (Buiten & Clevers 1994).

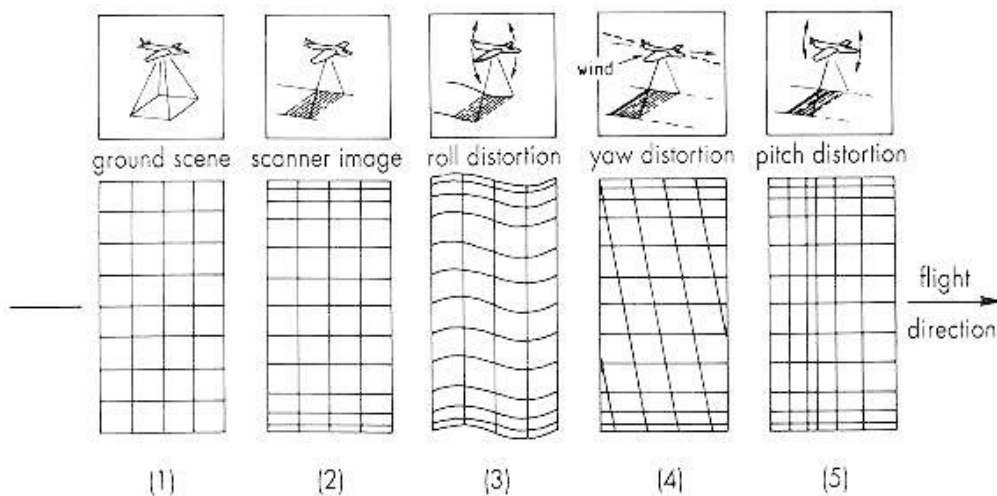


Figure 5.8: Geometric distortions of airborne remote sensing images by aircraft flight movements.

The most commonly applied method to correct for geometric distortion is by comparing the position of specific points in the image with the corresponding coordinates of these points on a map. These points are called **Ground Control Points or GCPs** and are most often bridges, road crossings or large buildings. Based on several of these ground control points, geometric transformation functions can be computed and used to fit the image on the map coordinates. Transformation functions look like:

$$\begin{aligned} u &= f(x,y) \\ v &= g(x,y) \end{aligned}$$

The (x,y) coordinates describe the position of the GCPs on the map, (u,v) describe the coordinates of the GCPs in the image in terms of rows and columns. f and g are the transformation functions. For satellite imagery a first order geometric transformation is best to correct satellite images, airborne images sometimes require higher order transformations. However, higher order transformations require more GCPs. The accuracy of the transformation function is mostly given in *RMS-error* (root mean square error) and refers to the distance between the input location of a GCP and the retransformed location for the same GCP.

Resampling

Having determined the geometric transformation function by using GCPs the next step is to compute DN values for the new defined image grid (x,y) based on the DN values in the old grid (rows, columns). The spacing of the grid is chosen according to the pixel size required e.g. from 30 by 30 m to 50 by 50 m. As the old pixels will never fit exactly on the newly defined pixels an interpolation of the new DN values is necessary. This process is called **resampling** and comprises three techniques (figure 5.9):

1. **Nearest neighbour resampling:** the new pixel value is the nearest neighbour in the old grid. The advantage of this method is that it is the easiest and fastest method and that the original data values are preserved.
2. **Bilinear interpolation:** the new pixel value is based upon the distances between the new pixel location and the four closest pixel values in the old grid (inverse distance interpolation). A disadvantage of this method is that the new DN-values are smoothed.
3. **Cubic convolution:** the new pixel value is computed from the 16 (or even 25) pixel values in the old grid closest to the new location.

Lillesand and Kiefer (2000) show the effect of the different resampling methods on a MSS image on page 476. Note the ‘stair stepped’ effect in the nearest neighbour resampling and the smoothing effect in the two other methods.

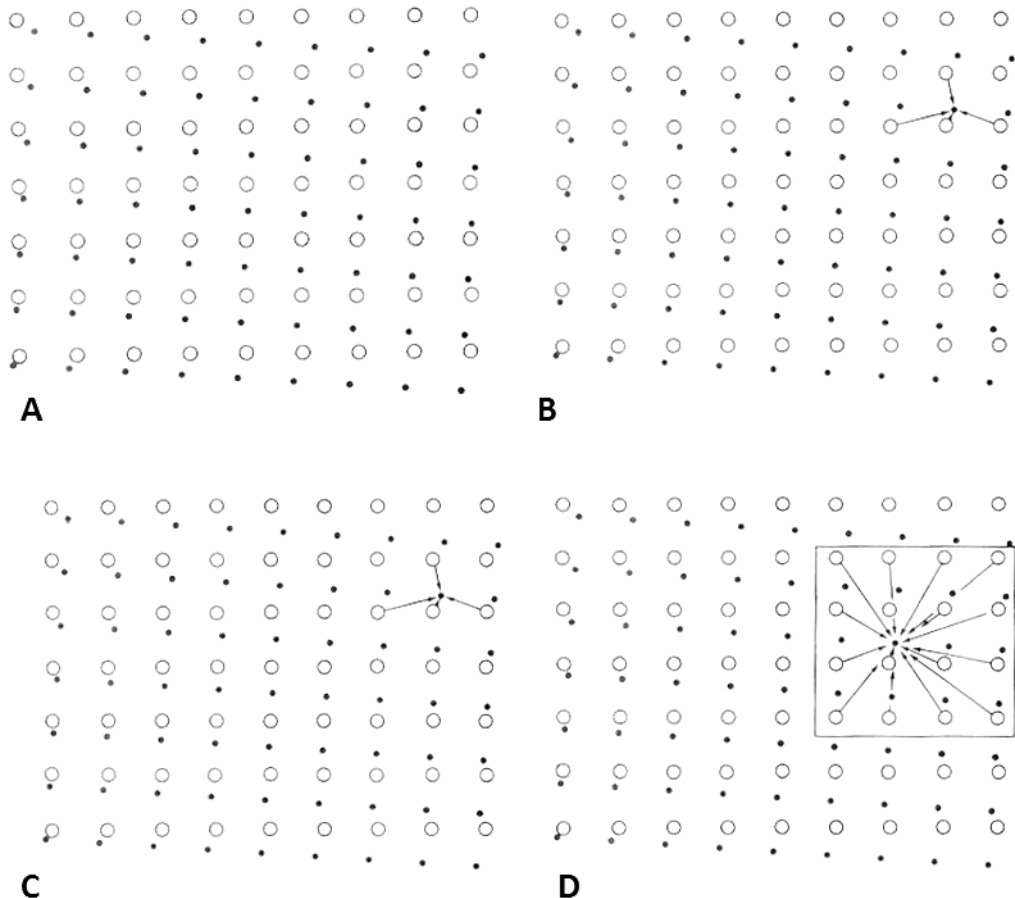


Figure 5.9: Resampling techniques:

- A) Open circles indicate reference grid from input image (and location determined from topographical map or GPS).
- B) Nearest Neighbourhood resampling: each estimated (new) value receives the value of the nearest point on the reference grid.
- C) Bilinear interpolation: each estimated value in the output image is formed by calculating the weighted average (inverse distance) of the four neighbours in the input image.
- D) Cubic convolution: each estimated value in the output matrix is found by computing values within a neighbourhood of 16 pixels in the input image.

5.5 Image Enhancement

Image enhancement is the modification of a digital image to alter its impact on the viewer. Generally enhancement is carried out after image restoration. Image enhancement may comprise contrast improvement (by stretching), edge enhancement by digital filtering and information extraction techniques such as ratioing or principal component transformation.

Contrast Enhancement

Techniques for improving image contrast are the most widely used in image processing. The sensitivity range of the Landsat sensors was designed to record a wide range of terrains from water bodies to bright ice fields. As a result few scenes have a brightness covering the full sensitivity range of the sensor. To produce an image with optimum contrast, it is important to use the entire brightness (and colour) range of the monitor. The **histogram** of the image provides information on the used brightness range. A histogram of a digital image is a x-y diagram showing the frequency of occurrence (number of pixels) of individual values (digital numbers). The histogram information provides useful information to stretch optimally the grey-tones or colours over the digital values (figure 5.10).

Linear contrast stretch is the simplest contrast enhancement method. Extreme black and extreme white are assigned to the smallest, respectively the largest DN value in the histogram. To fasten the process a lookup table or LUT is often used. Non-linear stretch or special stretch, this type of stretch uses a e.g. user-defined part of the histogram or a non-linear e.g. gaussian curve to perform a stretch on the image (figure 5.10). Histogram stretch: image values are assigned to the display levels (extreme black to extreme white) on the basis of their frequency of occurrence i.e. the number of pixels with a specific grey-tone is equal for all grey-tone classes and consequently, all grey levels occur in equal portions on the screen.

Density slicing

Density slicing converts the continuous grey tone of an image into a series of density intervals (or slices) each corresponding to a specified digital range and assigns a colour to each range. This technique emphasizes subtle grey-tone differences by assigning colours.

5.6 Digital Image Filtering

Spectral enhancement of images such as the previous described stretch techniques operates on each pixel of the image individually. Spatial enhancement techniques or convolution operations modifies pixel values based on the values of surrounding pixels. Spatial enhancements of most interest in remote sensing generally relate to smoothing of the image, edge detection and enhancement, and line detection. Such a digital filter operates by moving a **template, window or kernel (often 3 by 3 pixels)** over the image row-by-row and column-by-column. At each position of the template on top of the image a mathematical operation (sum, multiply, variance) is performed on the pixel values covered by the template. The response of this mathematical operation yields the new pixel value for the centre pixel of the template. Although templates of 3 by 3 pixels are most often used, templates of any size can be used. Examples of digital filters are the **low pass filter** aiming at image smoothing, the **high pass filter** aiming at image sharpening, the **gradient filter** aiming at enhancing edges or transition zones in the image, the **Laplace filter** and the **Sobel filter** both also aiming at enhancing edges and suppressing noise. More complex filters assess e.g. the variability of spectral reflectance in the template (texture filter, variance filters or fractal filters). A thorough description of image digital image filtering and other digital image processing techniques is given by Gonzalez and Wintz (1987). Table 5.1 shows the templates of a number of digital filters, figure 5.11 illustrates the effect of some digital filters on a simple digital profile of an image.

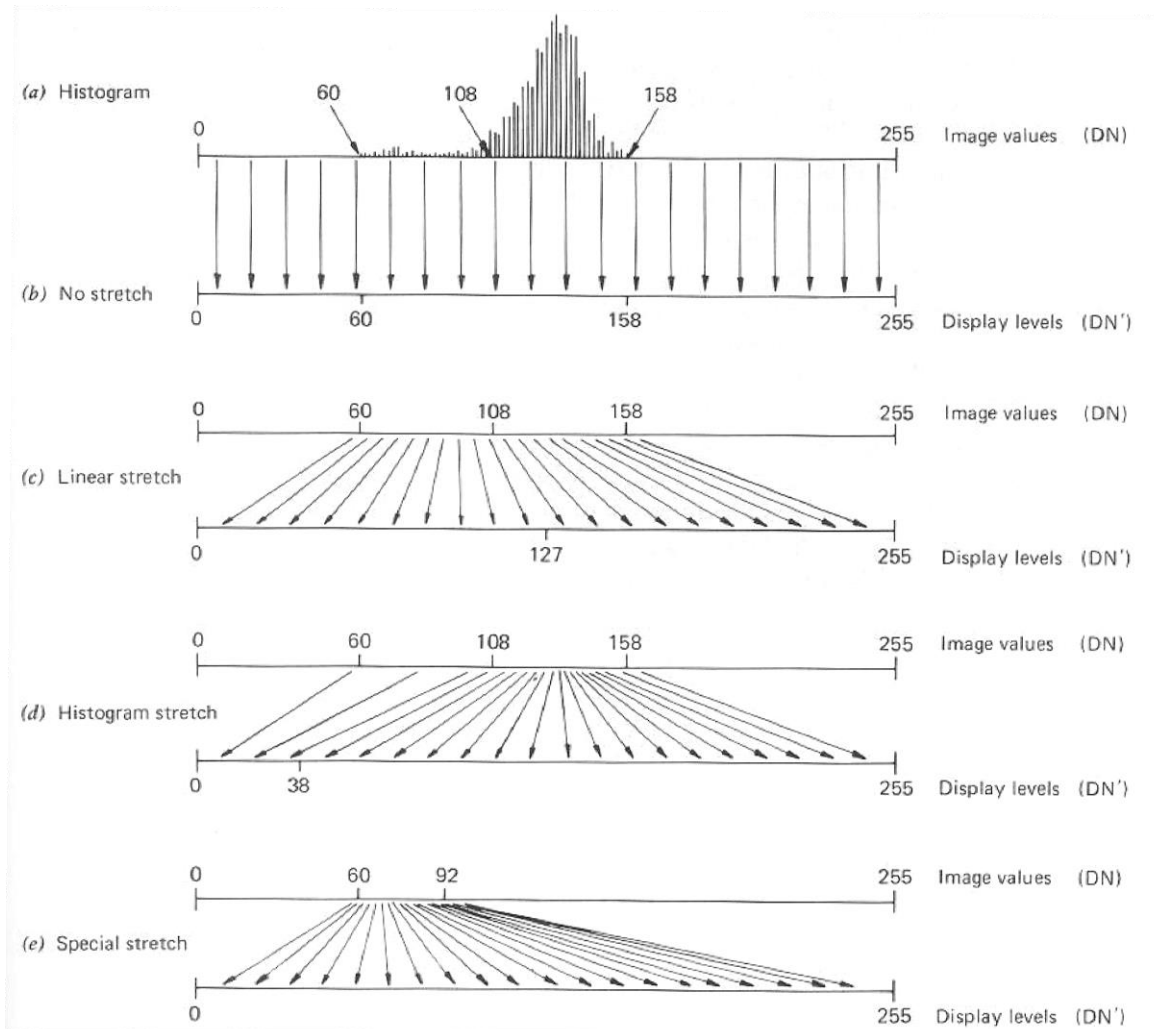


Figure 5.10: Principle of contrast stretch enhancement (*Lillesand & Kiefer, 1994*).

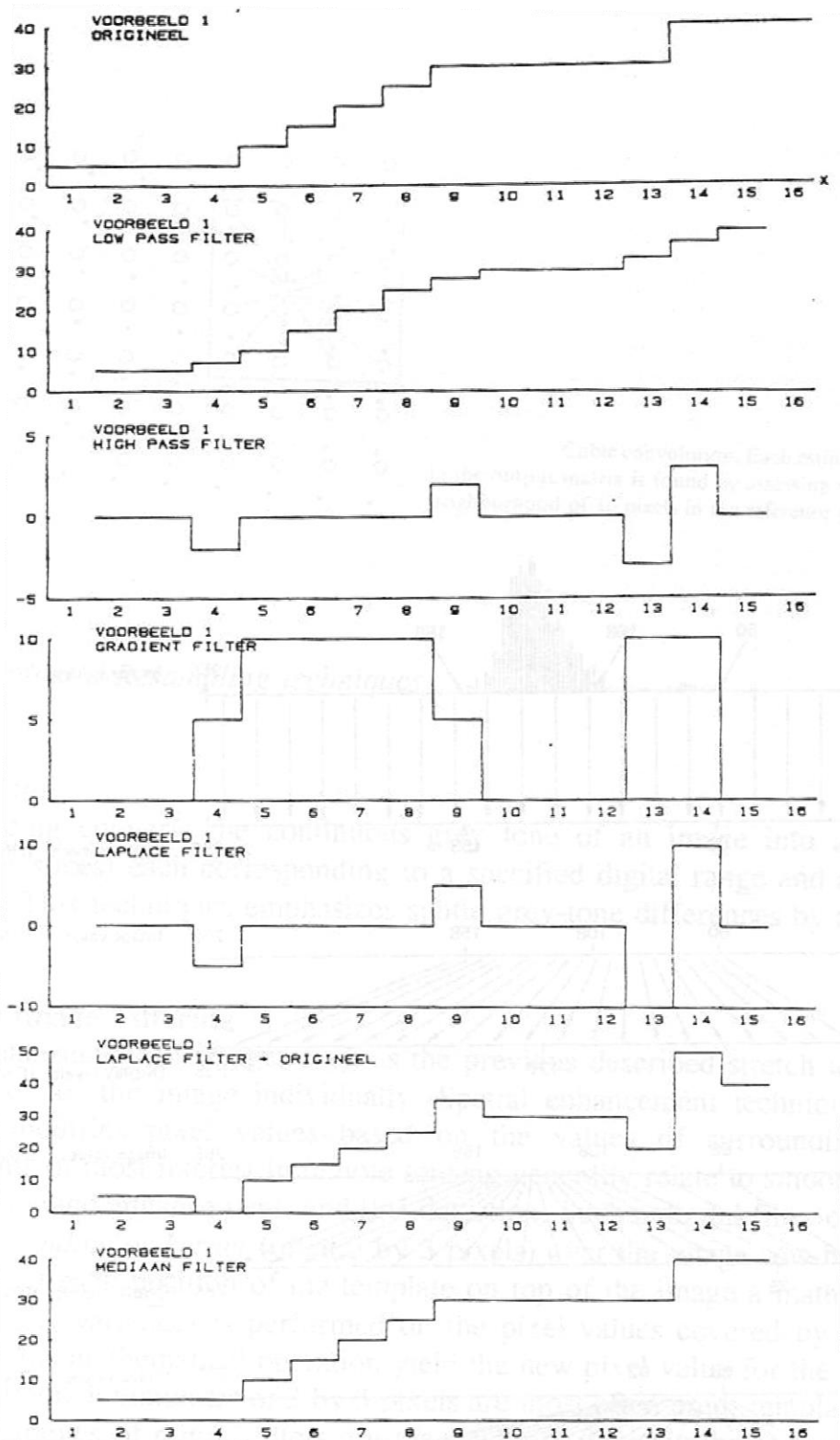


Figure 5.11: The effect of a number of digital filter on the profile of a digital image.

Table 5.2: Some examples of digital image filters.

Low pass filter:	$1/9 * \begin{vmatrix} 1 & 1 & 1 \\ 1 & 1 & 1 \\ 1 & 1 & 1 \end{vmatrix}$
High pass filter:	$\begin{vmatrix} -1 & -1 & -1 \\ -1 & 8 & -1 \\ -1 & -1 & -1 \end{vmatrix}$
Gradient filter:	$\begin{vmatrix} 0 & 0 & 0 \\ -1 & 0 & -1 \\ 0 & 0 & 0 \end{vmatrix}$
Laplace filter:	$\begin{vmatrix} 0 & -1 & 0 \\ -1 & 4 & -1 \\ 0 & -1 & 0 \end{vmatrix}$
Laplace + original:	$\begin{vmatrix} 0 & -1 & 0 \\ -1 & 5 & -1 \\ 0 & -1 & 0 \end{vmatrix}$
Median filter:	$\begin{vmatrix} v1 & v4 & v7 \\ v2 & v5 & v8 \\ v3 & v6 & v9 \end{vmatrix}$
Directional filter:	$1/f * \begin{vmatrix} 1 & 1 & 1 \\ 0 & 0 & 0 \\ 1 & 1 & 1 \end{vmatrix}$

5.7 Spectral Ratioing

Spectral ratioing refers to enhancement techniques by combining pixel values from different spectral bands. Ratio images are prepared by dividing the digital numbers in one band by the corresponding digital numbers in another band for each pixel, stretching the resulting values, and plotting the new values as an image. **The most widely used ratio techniques are ratios to enhance the vegetation cover or to distinguish bare soil from vegetation.** Spectral indices used for these purposes are e.g. (Huete, 1989; Sellers, 1989; Tucker, 1979), the VI: Vegetation Index, the **NDVI: Normalized Difference Vegetation Index**, the GEMI, the **SAVI: Soil Adjusted Vegetation Index**, the PVI: Perpendicular Vegetation Index, the GVI: Green Vegetation Index, or the TVI: Transformed Vegetation Index. Figure 1.9 and figure 5.12 illustrates the principle of the vegetation indices. Most vegetation indices combine one infrared spectral band with one visible band.

Vegetation indices are often used to estimate from remote sensing images the leaf area index, the vegetation cover or the biomass for specific areas (De Jong 1994; Huete, 1989). Although there is a correlation between biomass, leaf area index, vegetation cover and spectral vegetation indices, some

caution is necessary. The relations between spectral indices and these vegetation properties is often area-specific (that means that functions developed in one study area cannot be used directly in other areas), the condition of the soil and the type of soil beneath the vegetation or crop has a certain impact on the value of the spectral indices: although the vegetation cover remains the same, the value of the spectral index might change due to a change in underlying soil.

An advantage of using spectral ratioing techniques is that they express the spectral characteristics of image features regardless the intensity of illumination. Consequently, the same object at sunlit sites or at shadow sites will appear different in the original spectral bands but will have the same spectral brightness after spectral ratioing. Figure 5.13 shows the principle with an computational example.

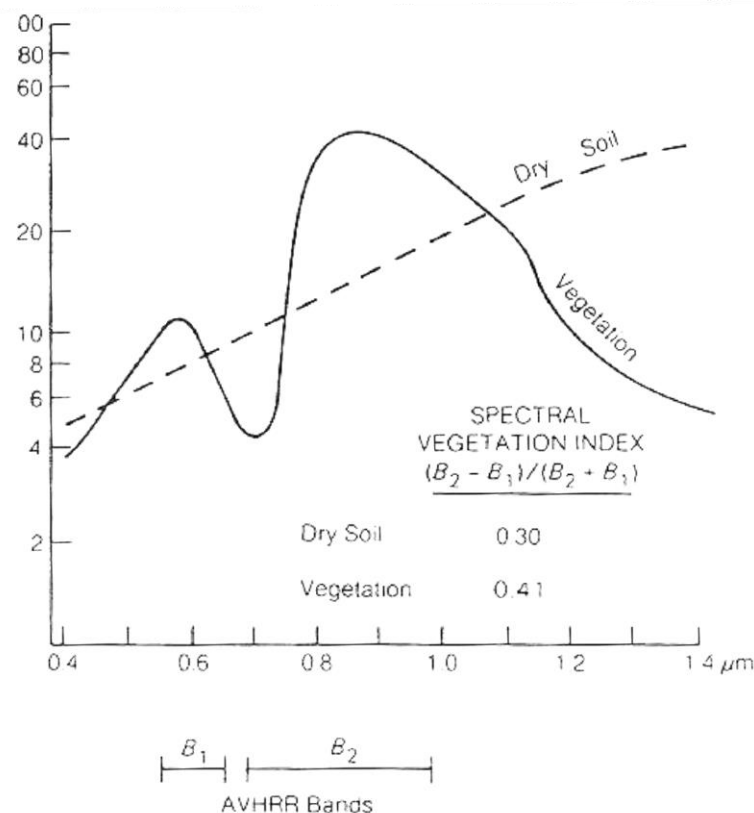
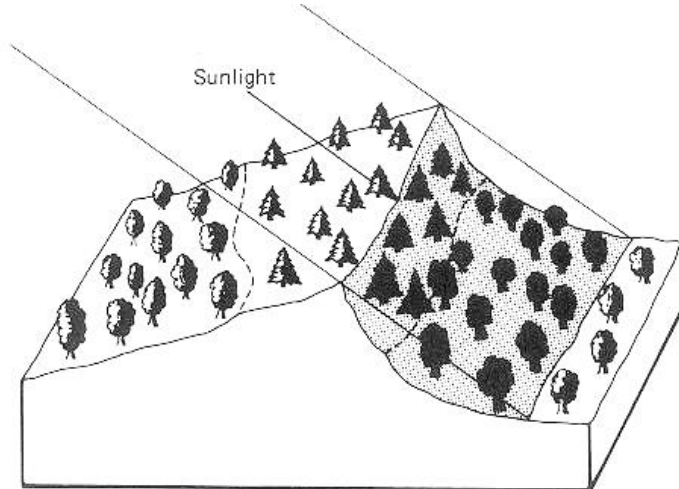


Figure 5.12: Reflectance spectra of vegetation and dry soil and their computed vegetation index (Sabins, 1987).



Land cover/illumination		Digital Number		
		Band A	Band B	Ratio (band A/band B)
Deciduous	Sunlit	48	50	0.96
	Shadow	18	19	0.95
Coniferous	Sunlit	31	45	0.69
	Shadow	11	16	0.69

Figure 5.13: Reduction of scene illumination effects through spectral ratioing (Lillesand & Kiefer, 1994).

5.8 Digital Image Transformation

Principal Component Transformation: PCA

Multi-spectral bands of e.g. Landsat TM or SPOT show often a very high correlation especially among the visible bands or among the infrared bands. That indicates that the different spectral images are to a large extent similar. **Principal Component Analysis (PCA)** is a technique to reduce the redundancy of information in spectral data. The purpose of PCA is to compress all of the information contained in e.g. 6 Landsat TM bands into fewer bands. The statistical distribution of the pixel values over the multi-spectral bands is used to compute a new, most effective, abstract coordinate system. Figure 5.14 shows the principle for a two-dimensional situation i.e. 2 spectral bands. For a Landsat TM image 6 spectral bands are used and hence, a transformation is computed in a 6 dimensional space.

Tasseled Cap Transformation

The **Tasseled Cap transformation** was originally developed as a linear transformation of Landsat multi-spectral scanner (MSS) data that projects soil and vegetation information into a single plane in the multi-spectral data space (Kauth and Thomas, 1976). The name Tasseled Cap originates from the 'triangular, cap shaped region with a tassel' in the visible and near infrared space (figure 5.15). Standard Tasseled Cap transformation coefficients for Landsat TM for the USA are presented in table 5.3. Basically three new dimensions are considered: brightness, greenness and wetness. **Brightness** is a measure of overall reflectance, i.e. differentiating light soils from dark soils. **Greenness** displays the contrast between the sum of the near-infrared reflectance and the sum of the visible reflectance and is thought to be a measure of the presence and density of green vegetation. **Wetness** is most sensitive to changes of soil moisture content and plant moisture.

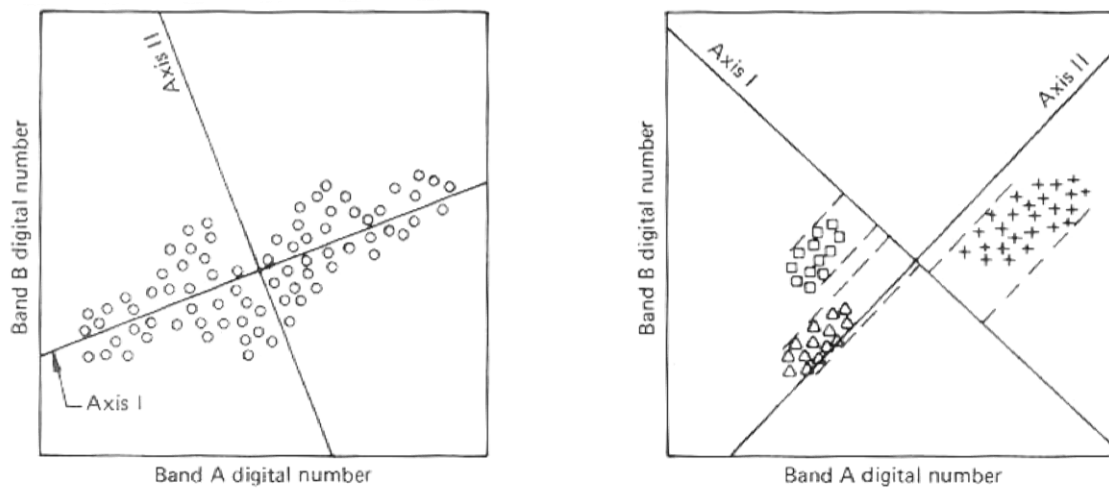


Figure 5.14: Rotated coordinate system used in a principal component transformation (Lillesand & Kiefer, 1994).

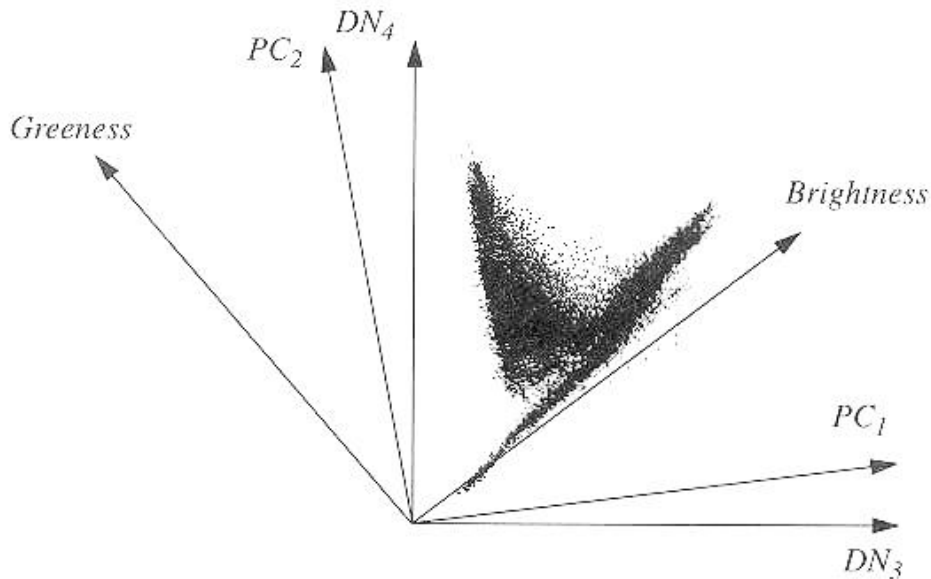


Figure 5.15: Graphical representation of the Tasseled Cap Transformation (Schowengerdt, 1997).

Table 5.3: Thematic Mapper Tasseled Cap Transformation Coefficients proposed by Crist and Cicone (1984a).

	TM1	TM2	TM3	TM4	TM5	TM7
TC1: Brightness	0.3037	0.2793	0.4743	0.5585	0.5082	0.1863
TC2: Greenness	-0.2848	-0.2435	-0.5436	0.7243	0.0840	-0.1800
TC3: Wetness	0.1509	0.1973	0.3279	0.3406	-0.7112	-0.4572

Linear Spectral Unmixing

Linear spectral unmixing (LSU) is a method to determine relative abundances of materials in a multi- or hyperspectral image. Pixels often represent a combination of different materials. LSU tries to find so-called endmembers (extreme pixel vectors) that can be used to unmix the pixels using a linear model. That way, the relative abundance of materials that are depicted can be determined, based

on the materials' spectral characteristics. The reflectance at each pixel of the image is assumed to be a linear combination of the reflectance of each material (or endmember) present within the pixel. For example, if 25% of a pixel contains material A, 25% of the pixel contains material B, and 50% of the pixel contains material C, the spectrum for that pixel is a weighted average of 0.25 times the spectrum of material A, plus 0.25 times the spectrum of material B, plus 0.5 times the spectrum of material C. So, given the resulting spectrum (the input data) and the endmember spectra, Linear Spectral Unmixing solves for the abundance values of each endmember for every pixel (www.exelisvis.com).

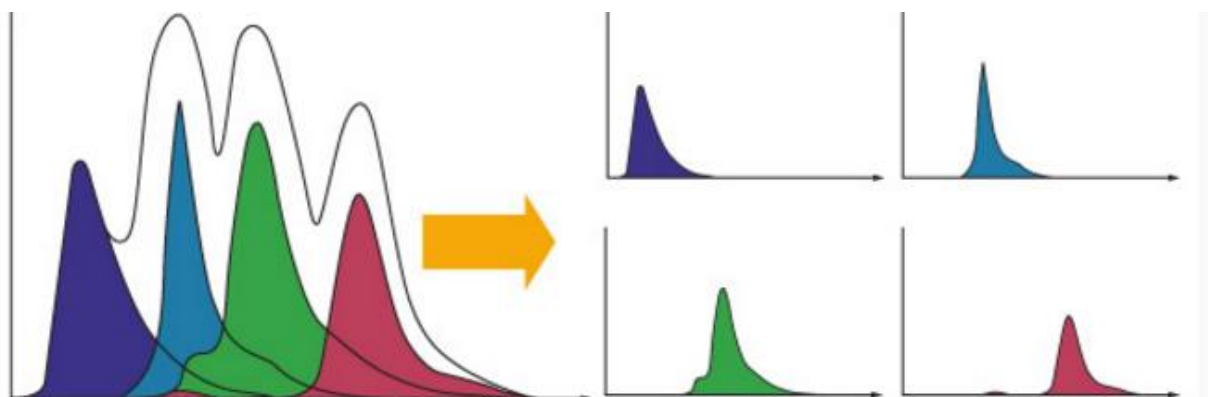


Figure 5.16: Spectral Unmixing. The various contributions to the total pixel spectrum (left) are separated into the individual endmembers (<http://www.sonybiotechnology.com/sa3800/tech2>).

5.9 Image classification

Digital image classification refers to the process of assigning pixels to classes. Usually each pixel is treated as an individual unit composed of values in several spectral bands. **Classification** of each pixel is based on the match of the spectral signature of that pixel with a set of reference spectral signatures. The term 'classifier' refers loosely to a computer program that implements a specific procedure for image classification. The classes form regions on a map or an image, so that after classification the digital image is presented as a GIS-layer or a mosaic of uniform parcels each identified by a colour or symbol. Most classifiers are spectral classifiers or point classifiers because they consider each pixel as a point observation. Other methods of image classification are based on textural information of the image, they use information from neighbouring pixels to assign classes to pixels and are referred to as context classifiers or textural classifiers.

A basic distinction between classifiers separates **supervised** from **unsupervised** classification: In *supervised classification* (figure 5.17), the image analyst controls the pixel categorization process by specifying, to the classification algorithm, numerical descriptors of the various land cover types in an image. Representative sample sites of known cover type (called *training areas* or *ground truth polygons*) are used to characterise land cover types in terms of average reflectance values per spectral band and their variance. While classifying, each pixel in the image, is compared numerically to each category of land cover and labelled with the category, it is most similar. The success of the supervised classification depends on the capability of the analyst to define representative training areas. Some criteria for training area are:

- the number of pixel per land cover type must be sufficient e.g. 100 pixels per land cover type;
- the size of the training area should be sufficient large to include the spectral variance;

- the training areas should be uniform with a statistically normal distribution and without outliers: the histogram of a training area should never display two or more distinct peaks, the classification can never be successful with such a histogram shape.

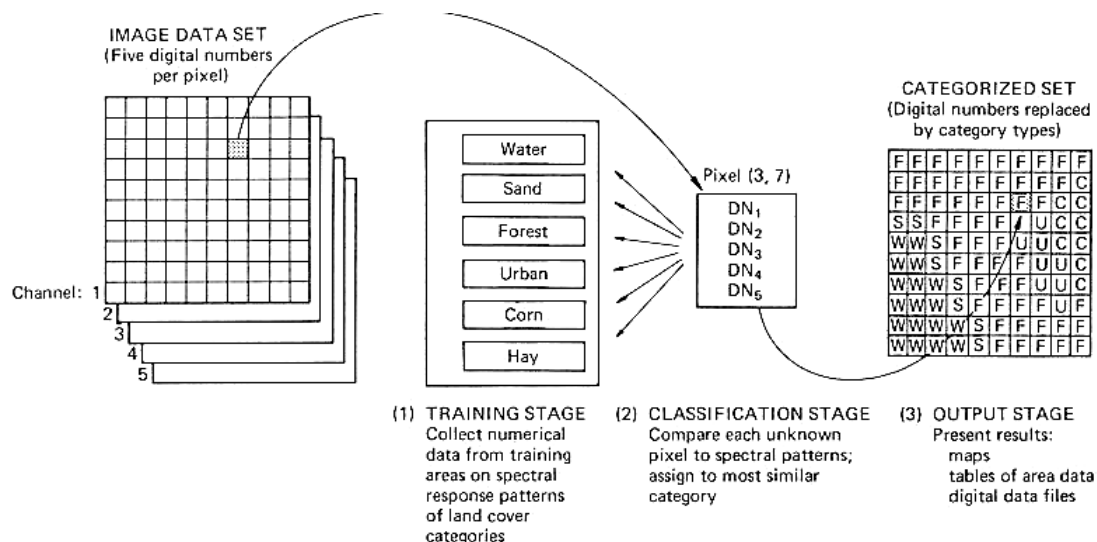


Figure 5.17: Principle of supervised image classification (Lillesand & Kiefer, 1994).

In the **unsupervised classification** approach the image data are first classified by aggregating them into spectral clusters based on the statistical properties of the pixel values (average, variation). Then the image analyst determines the land cover identity of each cluster by comparing the classified image data to ground reference data. A disadvantage of the unsupervised approach is that it is often not easy to relate image clusters to land cover types.

When the **training stage** of the supervised classification approach is completed, the image classification itself can be performed. In this classification stage the results of training are extrapolated over the entire scene. There are **three widely-used classification methods**:

- the minimum distance to mean classifier;
- the parallelepiped classifier;
- the maximum likelihood classifier.

The **minimum distance to mean classifier** is the simplest method and requires not as much computation time as the other two approaches. Figure 5.18 shows the procedure for only two spectral bands. First, the mean of each training class is calculated for each waveband (this is called the mean vector). Second, the pixels to be classified in the entire image are assigned to the class nearest to them. Third (optional), a data boundary is located at a certain distance so that if a pixel falls outside this boundary, it will be classified as unknown. The limitation of this classifier is its insensitivity to variance in the spectral properties of the classes.

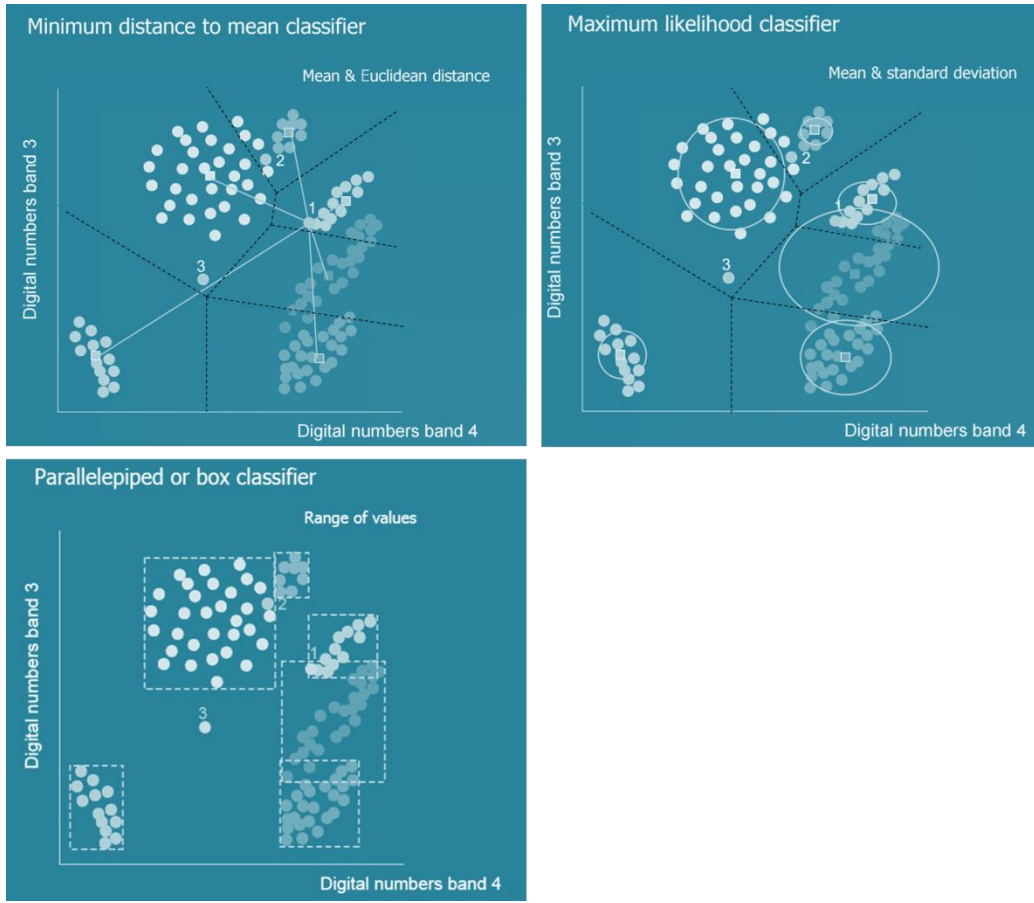


Figure 5.18: Minimum distance to mean (top left), maximum likelihood (right) and box (bottom left) classifiers.

Several methods exist to compute distances in multi-dimensional spaces such as the spectral 6-dimensional space of the Landsat TM. One of the simplest methods is the **Euclidean distance**.

$$D_{ab} = \left[\sum_{i=1}^n (a_i - b_i)^2 \right]^{1/2}$$

where i is one of n spectral bands, a and b are pixel values in the different spectral bands and D_{ab} is the Euclidean distance between the two pixels. This measure can be applied to many dimensions (or spectral channels). Figure 5.19 illustrates the Euclidean distance measure.

The **parallelepiped classifier or box classifier** is also very popular as it is fast and efficient. It is based on the ranges of values within the training data to define regions within the multi-dimensional space. Hence, it creates imaginary boxes in the spectral space. Figure 5.18 shows an example of the parallelepiped classification procedure with only two spectral bands for simplicity. The spectral values of unclassified pixels are projected into the data space and those that fall within the regions defined by the training data are assigned to the corresponding categories. Although this procedure is accurate, direct and simple, one disadvantage is obvious. Spectral regions for training categories may intersect or overlap (in such a case classes are assigned in sequence of classification). A second disadvantage is that other parts of the image may remain unclassified because they do not 'fall' into a box.

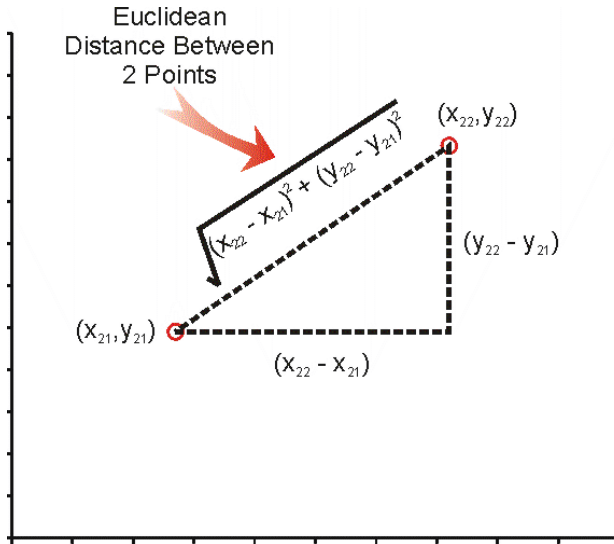


Figure 5.19: Illustration of the Euclidean distance measure (<http://hlab.stanford.edu>).

The **maximum likelihood classifier** is the most advanced classifier but it requires a considerable amount of computation time. As computers have become very fast and powerful, the latter is no longer a problem and the maximum likelihood classifier is widely used nowadays. The maximum likelihood approach does not only take into account the average DN-values of the training areas, it also accounts for the variance of pixel values of the training areas. The variances are used to estimate the probability of membership for a certain land cover class. Figure 5.21 shows a three-dimensional plot with the **probability density functions** of several land cover classes in spectral band 3 (visible red) and 4 (near infrared). The variance of the pixel values of the class ‘sand’ is very small (a distinct peak), the variance for urban is large. (Compare this with the Veluwe TM image exercise). Notice that the variance for the class ‘water’ is larger in band 3 than in band 4.

The equiprobability contours shown in figure 5.20 serve as a decision rule to assign pixels to certain land cover classes. The equiprobability contours are drawn using information from the training areas. The probability differs from one spectral band to another. The maximum likelihood classifier is a very powerful classifier but it is sensitive for the quality of the training data: the likelihoods (or probabilities) are computed based on the assumption that the training data have a multi-variate, normal (Gaussian) frequency distribution. Remote sensing data do not always fulfil this condition, you should check the distribution of your training data before using this classifier.

The maximum likelihood classifier is based on the Bayesian decision rule. This technique allows to use so-called ‘**a priori information**’ during the classification. If a certain crop grows e.g. only on a specific type of soil and a digital soil map is available, the classification can be directed by using this information by: ‘it is very unlikely that this crop will occur on other soil type than...’. Examples and procedures are described by Strahler (1980), De Jong and Riezebos (1991) and Jansen (1994).

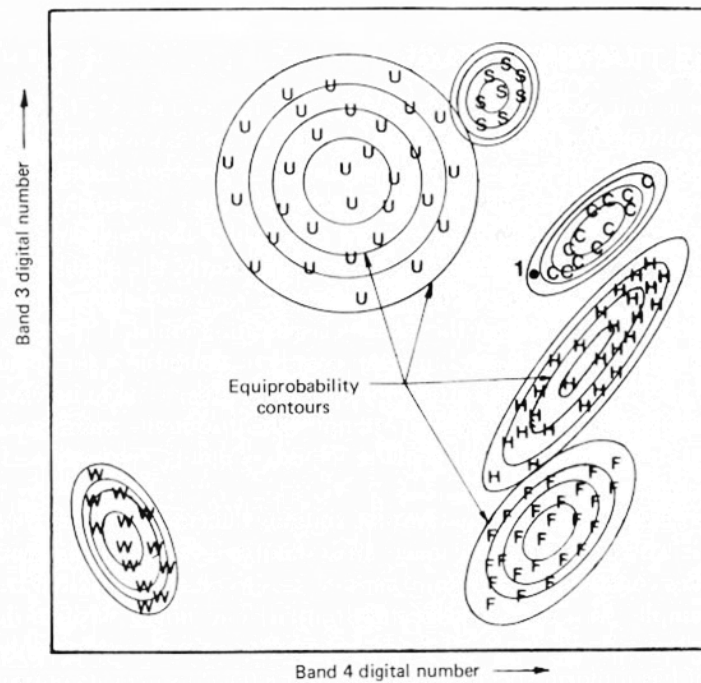


Figure 5.20: Equiprobability contours defined by the maximum likelihood classifier (Lillesand & Kiefer, 1994).

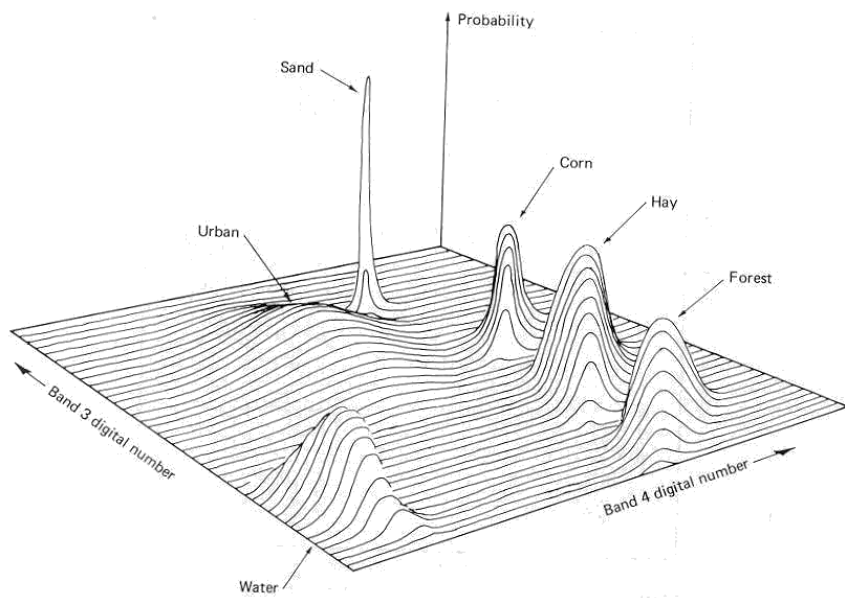


Figure 5.21: Probability density functions defined by the maximum likelihood classifier (Lillesand & Kiefer, 1994).

Spectral Angle Mapping

Spectral Angle Mapper (SAM) is a physically-based spectral classification that uses an n -Dimensional angle to match pixels to reference spectra where n is the number of bands in the image. The algorithm determines the spectral similarity between an image spectrum (representing an unknown material) and a reference spectrum (representing a known material) by calculating the angle between the spectra, treating them as vectors in n -dimensional spectral space, where n is the number of bands (figure 5.22). This technique, when used on calibrated reflectance data, is relatively

insensitive to illumination and albedo effects. SAM compares the angle between the endmember spectrum vector and each pixel vector in n -D space. Smaller angles represent closer matches to the reference spectrum (www.exelisvis.com).

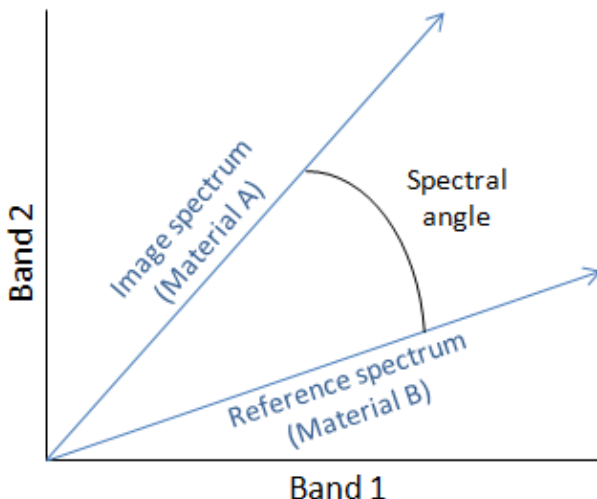


Figure 5.22: Illustration of spectral angle mapping, using 2 bands (www.exelisvis.com).

Only a few types of classifiers are described in these lecture notes. Many other approaches to the classification of digital images have been developed. It is not possible to state that a given classifier is ‘best’ for all circumstances, because the characteristics of each image, the conditions of the area of interest and the objectives of the study vary so greatly. Therefore, it is essential that the image analyst understands the alternative strategies for image classification in order to select the most appropriate classifier for the task at hand.

Accuracy assessments

Accuracy of a classification of a remotely sensed image refers to the ‘correctness’: a measure of the agreement between a standard assumed to be correct and an image classification of unknown quality. Hence, if a number of pixels is classified as deciduous forest, the end-user wants to know what the chance (or probability) is that these pixels really represents deciduous forest or pine forest or bare soil. The most widely used procedure to assess accuracy is to work with two training sets. One training set is used to classify the image, the second set is used to estimate the correctness of the classification. Such an approach requires the availability of sufficient field data.

Sources of classification errors can be numerous: human errors by the assignment of classes, human errors during the field survey, errors due to the technical part of the remote sensing system e.g. striping or line drop out, due to spectral or spatial resolution of the system, non-purity of the pixels i.e. **mixed pixels** covering e.g. two agricultural lots do not give pure spectral signatures of land cover types, etc. Many methods are developed to assess image classification accuracy and detailed descriptions are given by Campbell (1987) and Rosenfield & Fitzpatrick-Lins (1986).

The **error matrix** (table 5.4) or confusion matrix is the standard form of reporting site-specific uncertainty of a classification. It identifies overall errors and misclassification for each thematic class. Compilation of an error matrix is required for any serious study of accuracy. The error matrix consists of

an $n * n$ array where n represents the numbers of thematic classes.

The left hand side (y-axis) of the error matrix is labelled with categories on the reference (correct) classification. The upper edge (x-axis) is labelled with the same categories and refer to the classified image or map to be evaluated. The matrix reveals the results of a comparison of the evaluated and reference image. Together with the matrix, computed by the sum of the diagonal entries, is the overall accuracy given. Inspection of the matrix reveals how the classification represents actual areas in the field. Furthermore, the matrix reveals class-wise how confusion during the classification occurs. Campbell (1996) provides a good description of the error matrix.

Table 5.4: An example of an error matrix.

Reference image		Image to be evaluated							Totals
		Urban	Crop	Range	Water	Forest	Barren		
Urban	150	21	0	7	17	30	225		
Crop	0	730	93	14	115	21	973		
Range	33	121	320	23	54	43	594		
Water	3	18	11	83	8	3	126		
Forest	23	81	12	4	350	13	483		
Barren	39	8	15	3	11	115	191		
Totals	248	979	451	134	555	225	1748		

*Note: Percentage correct = sum of diagonal entries/total observations

6. Image Interpretation

6.1 Introduction

The objective of most environmental studies is not to determine the usefulness of remote sensing techniques for specific survey. Remote sensing is mostly a tool to collect information on the environment. The technical aspects of remotely sensed image acquisition, pre-processing and processing are often of minor importance. However, a certain level of knowledge of the technical aspects of remote sensing will be very useful for environmentalists to decide whether they should use data from radar systems or optical systems and to separate natural phenomena in their images from system caused patterns. Furthermore, some knowledge is necessary of the spectral behaviour of the objects of interest: soils, vegetation, crops and water. This chapter gives an introduction to the spectral behaviour of these four objects.

6.2 Spectral Behaviour of Vegetation

The reflectance of vegetation in the visible wavelengths (0.43 - 0.66 μm) is generally small and reflection in near infrared (0.7 - 1.1 μm) is generally large. Figure 6.1 shows the major influences on spectral properties of a leaf. Three features of leaves have an important effect on the reflectance properties of leaves:

- Pigmentation;
- Physiological structure;
- Water content.

Pigments (chlorophyll a and b) absorb radiation of the visible wavelengths. The species-specific structure causes discontinuities in the refractive indices within a leaf, which determine its near infrared reflectance. The reflection properties of a vegetation canopy are affected by the **physiological structure**: the spatial distribution of vegetated and non-vegetated areas, the number of layers of the vegetation cover, the types of vegetation, the leaf area index, the leaf angle distribution and the vegetation conditions. Figure 6.2 shows an simplified example. Some narrow absorption bands due to lignin, cellulose etc. are present in near and short-wave infrared wavelengths. The presence of water often masks their absorption features and the bandwidth of the TM is in fact too broad to detect these narrow absorption bands.

Water content of the leaves, and water in the atmosphere, reduce overall leaf reflectance and causes some narrow absorption features described earlier: the water absorption bands. Three major water absorption bands are located near 1.4, 1.9 and 2.7 μm , two minor absorption bands occur near 0.96 and 1.1 μm . The combined effect of pigments and physiological structure give healthy vegetation its typical reflectance properties. Combinations of the visible and near infrared spectral bands (see section on spectral ratioing) enables us to discriminate bare soil surfaces or water bodies from vegetation and to assess different percentages of vegetation coverage as shown in figure 6.3. A thorough description of the optical properties of vegetation and leaves is given by Guyot et al. (1992), Cohen (1991), Elvidge (1990), Goel (1989).

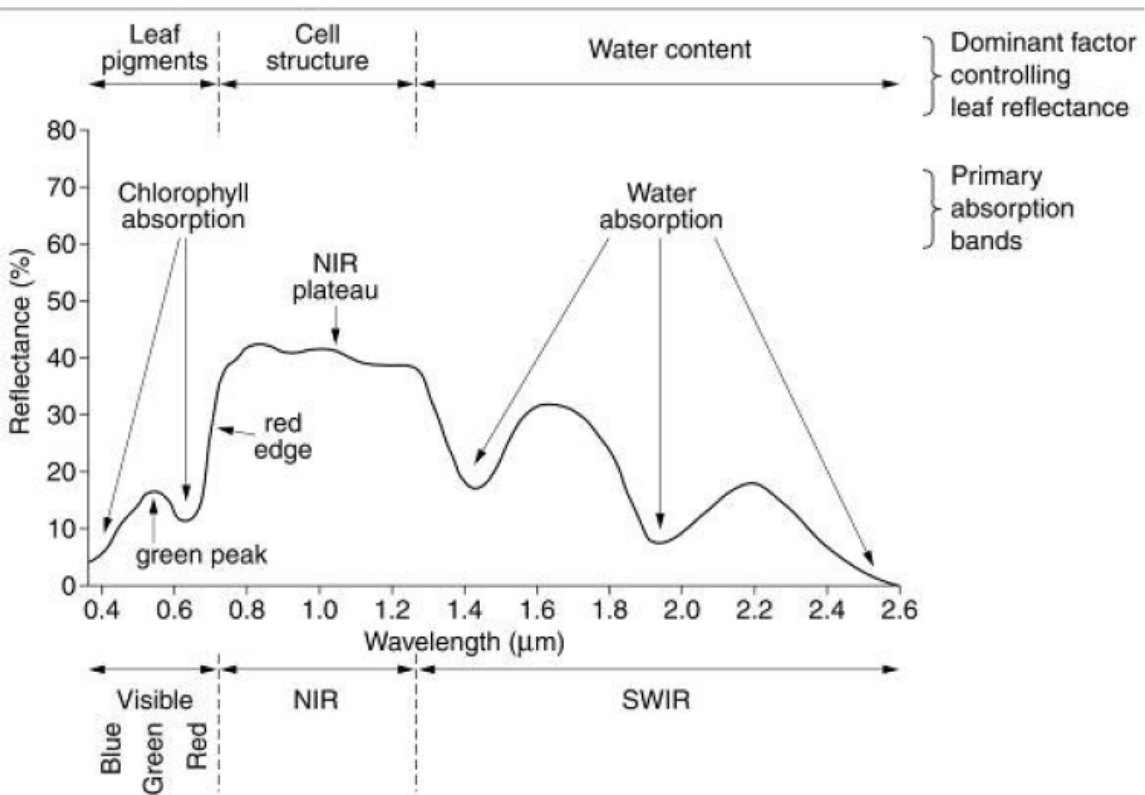


Figure 6.1: Major influences on spectral properties of a leaf (<http://www.gov.scot>).

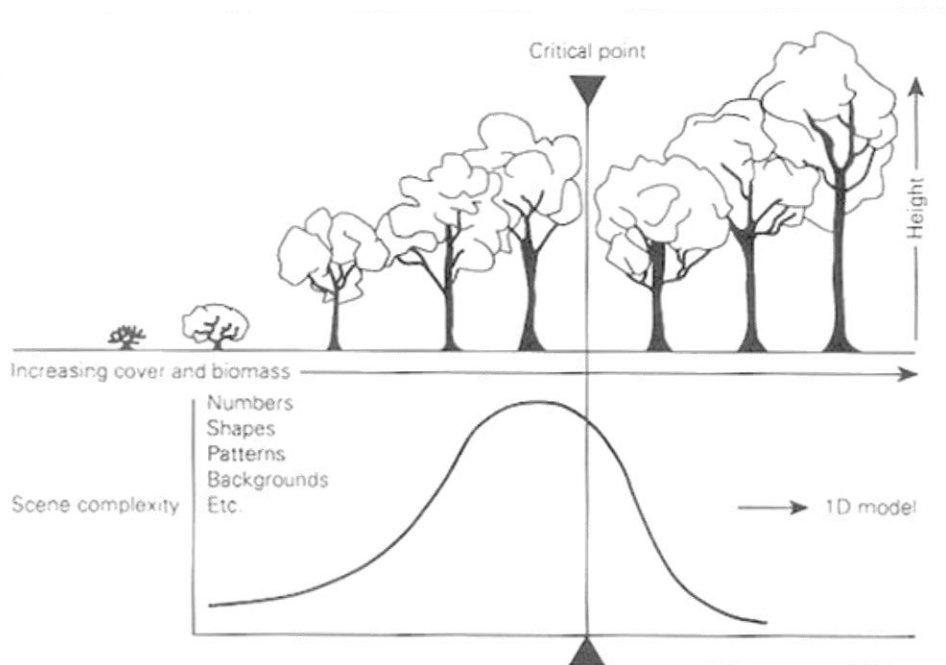


Figure 6.2: The effect of a changing canopy on a remote sensing scene.

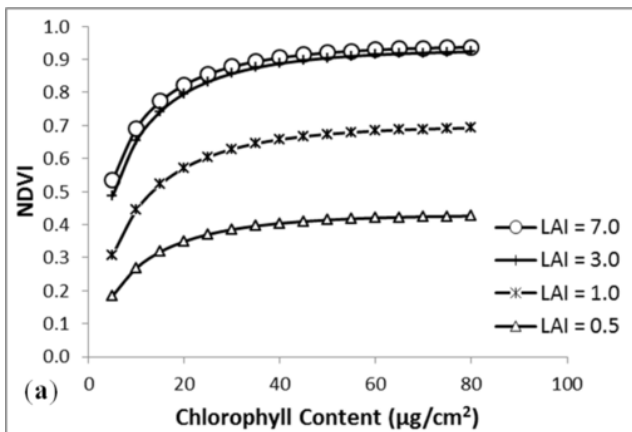


Figure 6.3: NDVI vs chlorophyll content for various LAI's (leaf area index) (Adapted from: Salas and Henebry, 2014).

Red Edge of the Vegetation Reflectance Curve

The red-edge is a characteristic feature of the spectral response of vegetation and perhaps is the most studied feature in the spectral curve. It is characterized by the low red chlorophyll reflectance to the high reflectance around 800nm (often called the red-edge shoulder) associated with leaf internal structure, water content and indicative for vegetation stress. Since the red-edge itself is a fairly wide feature of approximately 30nm, it is often desirable to quantify it with a single value so that this value can be compared with that of other species. For this the red-edge inflection point is used. This is the point of maximum slope on the red infrared curve.

For an accurate determination of the red-edge inflection point, a large number of spectral measurements in very narrow bands are required. For laboratory and field based studies, this is not a major obstacle as most laboratory based spectrometers record the reflectance in a large number of very narrow bands and so the derivative spectra give a fairly accurate position of the inflection point. For data where a large number of bands are not available within the red-edge region, the inflection point is approximated by fitting a curve to fewer points. One such method, described by Clevers and Jongschaap (2003), uses a polynomial function to describe the data and then obtains the inflection point from the equation. Guyot and Baret (1988) applied a simple linear model to the red infrared slope. They used four wavelength bands, centered at 670, 700, 740 and 780nm. Reflectance measurements at 670nm and 780nm were used to estimate the inflection point reflectance using the following equation:

$$R_{red\ edge} = \frac{R_{670} + R_{780}}{2}$$

Next, a linear interpolation procedure is applied between 700nm and 740nm to estimate the wavelength of the inflection point using a second equation:

$$\lambda_{red\ edge} = 700 + 40 \frac{R_{red\ edge} - R_{700}}{R_{740} - R_{700}}$$

An illustration of a vegetation reflectance curve around the red edge position is given in the figure 6.4. Furthermore, it is shown how the Red Edge Position can be computed using the method given by the two formulae above.

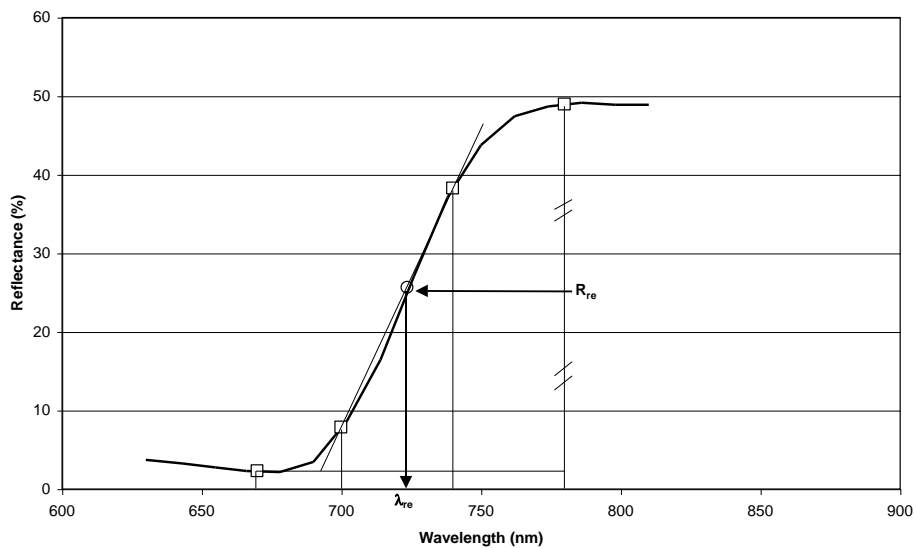


Figure 6.4: Illustration of the "linear method" (Guyot and Baret, 1988).

The red-edge index may be considered as a particular "vegetation index" of interest because of its low sensitivity to disturbing factors such as atmospheric conditions or soil brightness and its high sensitivity to canopy characteristics such as chlorophyll content or LAI.

6.3 Spectral Behaviour of Soils

The spectral behaviour of a soil is considerably different from vegetation: a soil reflectance curve in visible and infrared wavelengths shows less 'peak and valley' variation. The factors that influence soil reflectance seem to act over less specific spectral bands than for vegetation. This is the case when soil spectra are collected using conventional broadband sensors with a general band-width of 60 nm or more (SPOT, MSS, TM). Figure 6.5 shows examples of soil reflectance spectra. Notice the overall convex shape. If soil spectra are studied in more detail i.e. at increased spectral resolution (20 nm or less), significant differences between soil spectra become apparent (Goetz et al., 1985). A soil spectrum measured at high spectral resolution shows several diagnostic absorption features. In particular the short-wave infrared spectral region from 2000 to 2500 nm contains diagnostic absorption features of soil

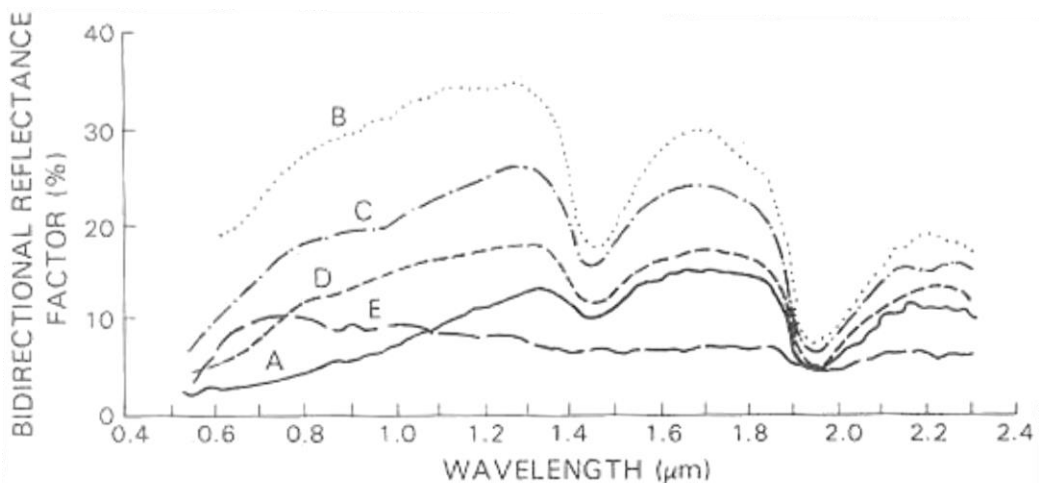


Figure 6.5: Some examples of soil reflectance spectra (Asrar, 1989).

constituents. The spectral resolution of Landsat TM and the French SPOT vary from 60 to 270 nm. Consequently, these broadband sensors are only marginally suitable for detecting these absorption features because the absorption bands of most soil materials are too small and are blurred in the broadbands (20 nm bands are generally adequate for the detection of absorption features, unfortunately, these kind of systems are not yet available aboard satellites). An example of absorption bands is given in figure 6.6.

The most important **soil properties** regarding reflection in optical wavelengths are:

- Moisture content;
- Organic matter content;
- Texture;
- Structure;
- Iron content;
- Mineral composition;
- Type of clay minerals;
- Surface conditions of the soil.

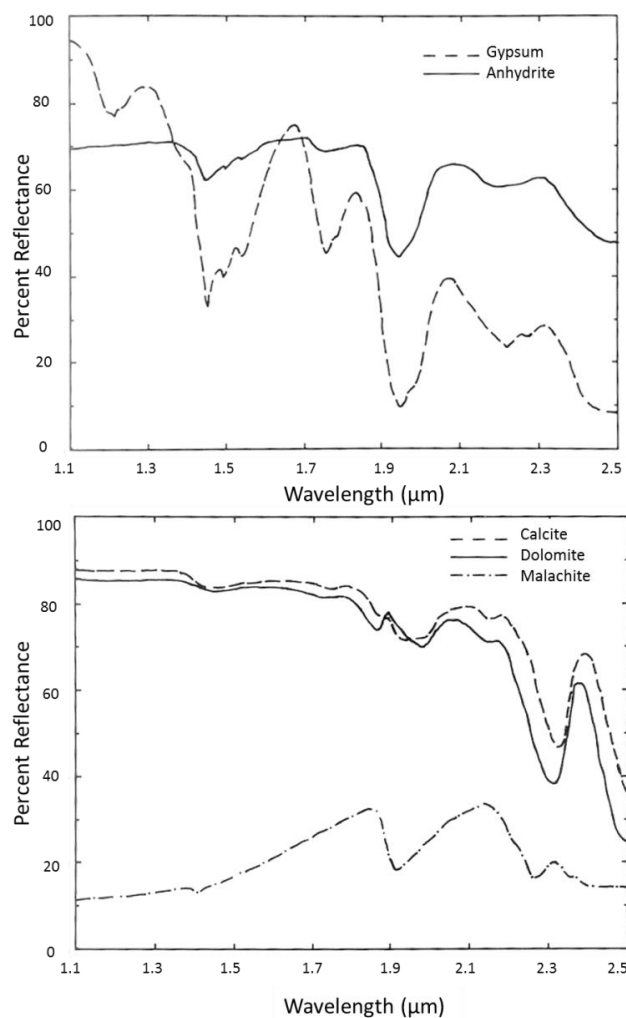


Figure 6.6: Reflectance spectra of carbonate minerals showing features at 2280 and 2340 nm and minerals showing OH en H₂O absorption bands (Asrar, 1989).

Increasing **moisture content** generally decreases soil reflectance across the entire spectrum. In fact, wet soils also appear darker to the eye than dry soils. Furthermore, reflectance spectra of moist soils include the prominent absorption bands for water and hydroxyl (OH^- ion) at 1.9 and 1.4 μm and the bands at 0.97, 1.20 and 1.77 μm . Figure 6.7 shows the effect of soil moisture on the reflectance curve of a soil.

Iron is an important constituent of a soil regarding its reflective properties. Many absorption features in soil reflectance are due to the presence of iron in ferric or ferrous form. For example, the general strong decrease of reflectance of soils towards the blue and ultraviolet wavelengths is caused by iron. Absorption features occur around 0.7 μm , 0.9 μm and 1.0-1.1 μm .

An increase of the **organic matter content** of a soil generally causes a decrease of reflectance over the entire spectrum that is similar to moisture. A high organic matter content and hence, a strong decrease of overall reflectance, might even mask other absorption features in the soil spectra. This effect is minimal for soils having organic matter contents below 2.0 to 2.5%. Unfortunately, little knowledge of the influence of different organic soil compounds and the different forms of organic matter on the spectral behaviour of soils is available in the literature.

The basic components of **soil minerals** are silicon, aluminium and oxygen. None of these soil constituents have diagnostic absorption features. Quartz for example, has a large reflectance throughout the short-wave spectrum and absorption features in short-wave quartz spectra are only due to impurities.

Soil particle size influences a number of soil properties such as moisture content and soil structure. Both of these properties also influence the reflectance of soils. Consequently, it is very difficult to measure the exact effect of increasing soil particle size on reflectance.

Most of the studies concerned with remote sensing and soils follow an empirical approach to distinguish soil types. Vegetation or crop cover always hampers the observation of soils in the optical wavelengths.

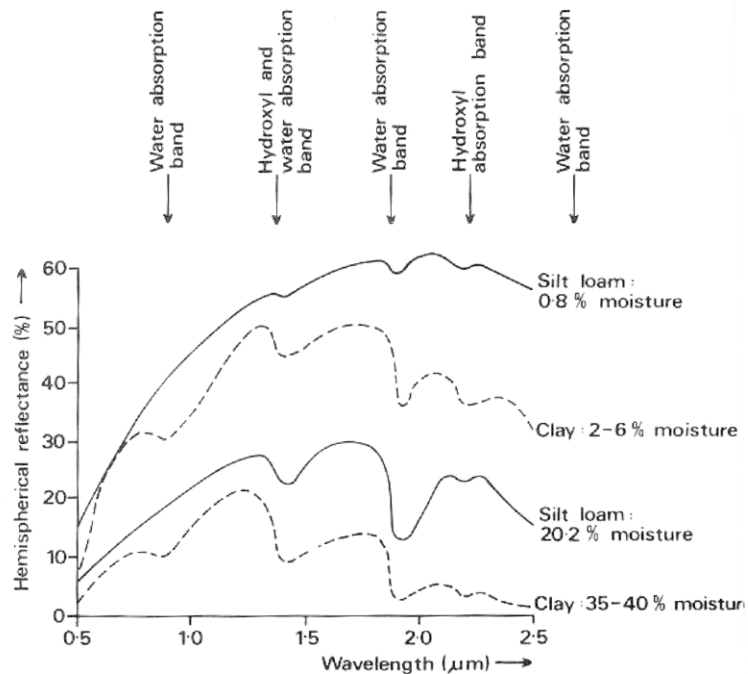


Figure 6.7: Spectral reflectance curves for wet and dry silty loam and wet and dry clay, and several diagnostic absorption features (Curran, 1986).

6.4 Multi-temporal Remote Sensing & Change Detection

Multi-temporal remote sensing techniques refer to the use of images of different dates to study temporal changes of e.g. crop cover or vegetation cover also often referred to as change detection. Sometimes the classification of agricultural crops can significantly be improved by monitoring the different growth stages of the crops. Maize e.g. has a short time span that the soil cover is high, the growing season lasts only from late June to late August. Cereals, in contrast, grow from late April to late July or early August. Hence, if multi-temporal remote sensing techniques are applied, the dates of image acquisition should be matched with the growing stages of the studied crops. A sequence of image acquired in January, June and August are mostly ‘best’ for multi-temporal crop classification.

A disadvantage of multi-temporal remote sensing is that it is expensive: multiple images must be acquired and radiometrically and geometrically corrected. Especially, the geometric correction must be very accurate otherwise the temporal change detected might be caused by ‘non-fitting’ agricultural lots. An example of a multi-temporal land use classification in the Po-valley in Italy is described by Azzali (1985). Figure 6.8 and 6.9 shows the temporal profiles of the crops.

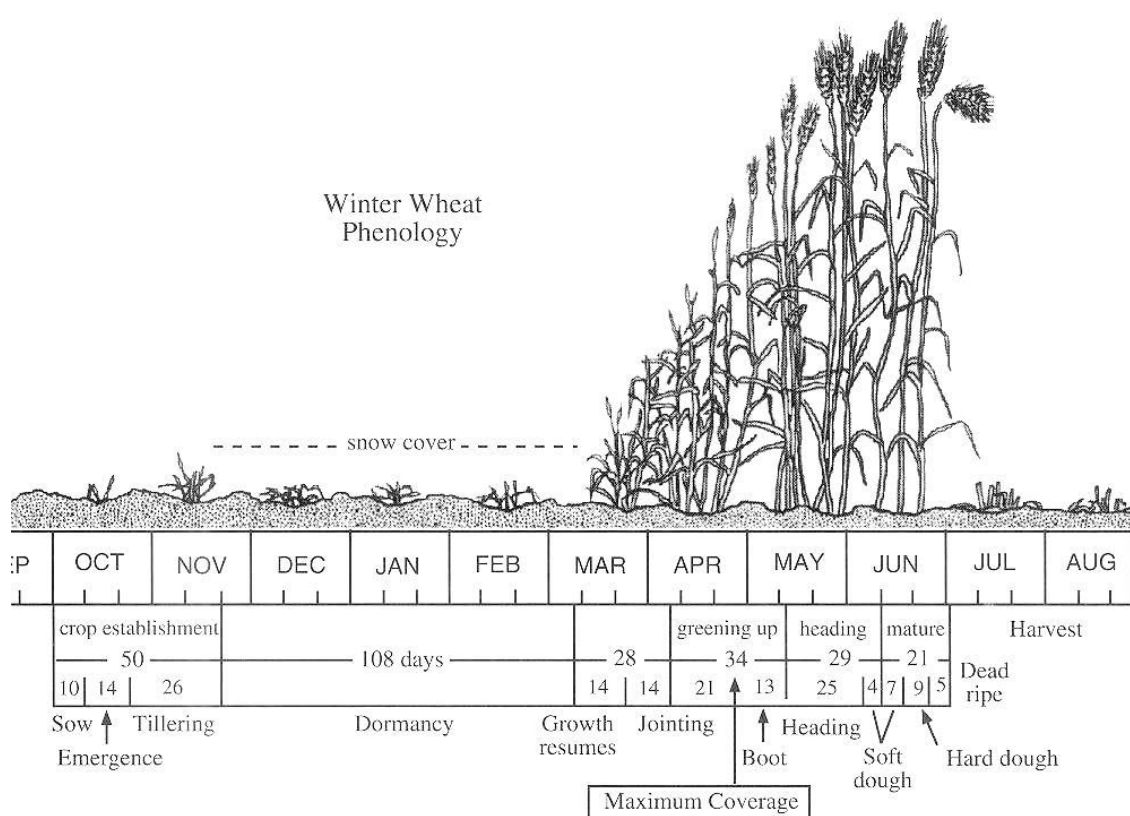


Figure 6.8: Temporal profile / phenological cycle of winter wheat (Jensen, 2000).

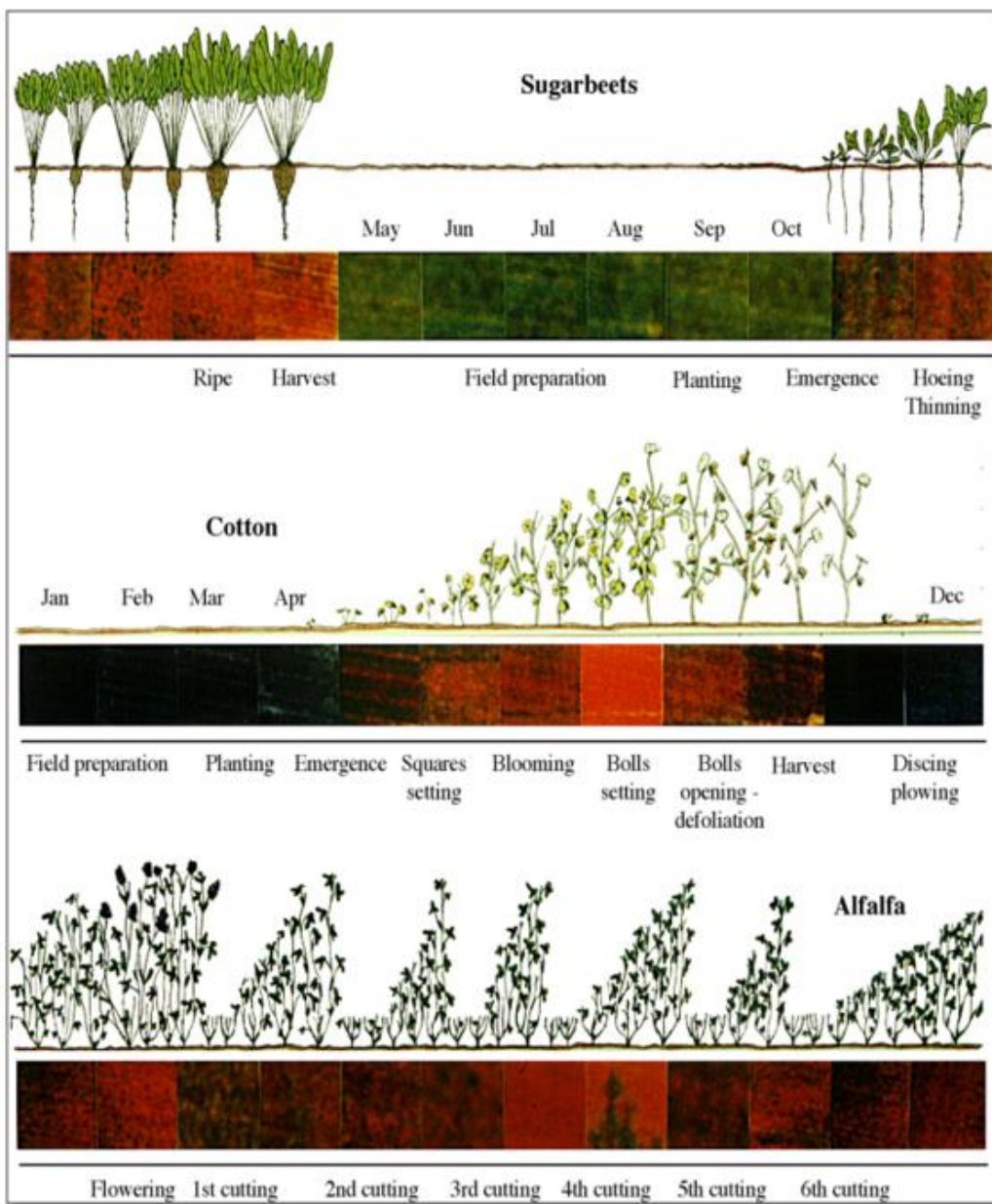


Figure 6.9: Phenological Cycles of sugar beets, cotton and alfalfa and images collected over a period of 12 months (Jensen, 2000).

Change detection is one of the most powerful applications of Earth observation. Several regions in the world are currently undergoing rapid, wide-ranging changes in land cover or land use. Well-known examples are of course the ongoing deforestation process in the Amazon, central Africa and Indonesia. Other examples are the changing land ice surface and length of glaciers as a result of our changing climate, or the use of InSAR to detect deformations of the surface. Earth observation provides a fast and relatively cheap way to inventory and monitor these changes. A prerequisite for the successful application of remote sensing for change detection is that the changes in land cover result in changes in radiance values and that these radiance changes are large with respect to other causes of radiance changes such as changing atmospheric conditions, differences in soil moisture and differences in sun angle (Mas, 1999; Singh, 1989). Change detection methods can basically be subdivided into the following broad classes:

1. **Image differencing:** registered images acquired at different times are subtracted to produce a residual image which represents the change between the two dates. Pixels of no radiance change are distributed around the mean while pixels of radiance change are distributed in the tails of the statistical distribution.
2. **Vegetation Index Differencing:** The NDVI is calculated (the normalized ratio of red and near infrared reflectance) for the images acquired at different dates. Next the NDVI values of the two images are subtracted and result in high positive or high negative values for change areas.
3. **Direct multi-date classification:** This method is based on the single analysis of a combined dataset of the two dates images aiming at identifying areas of changes. Two images are first merged into one multi-band image set. Classes where changes are occurring are expected to present statistics significantly different from where change did not take place and can so be identified. Unsupervised classification methods e.g. the isolate algorithm to reveal the spectral distance patterns in the data.
4. **Post-classification analysis:** The two (or more) images acquired at different dates are first independently classified using the same legend (number of classes and type of classes). Next, the two images are overlaid and compared by subtracting or otherwise. It should be noted that the accuracy of the change detection depends on the accuracies of each of the individual classification results and the geometric match of the imagery.

Detailed description of change detection studies are available in Lu et al. (2004), Lunetta & Elvidge (1999), Mas (1999) and Singh (1989).

6.5 Imaging Spectroscopy

As already discussed in chapter 2, imaging spectroscopy refers to the acquisition of images in many, very narrow, contiguous spectral bands in the optical part of the spectrum . Absorption features in soil and vegetation spectra are caused by the interaction between electromagnetic radiation (photons) and matter at the level of molecules and electrons. Two major types of interaction cause diagnostic features in reflectance spectra throughout the optical region: electronic processes and vibrational processes:

Electronic transitions refer to the changes in the energy state of electrons bound to atoms, molecules or crystal lattices. Electronic processes produce rather broad absorption bands for the weathered materials found at the soil surface. These bands occur mostly in the ultraviolet ($< 0.4 \mu\text{m}$) and extend as overtones with diminishing frequency into the visible and near infrared.

Vibrational transitions refer to the very small displacements of atoms from their equilibrium positions induced by radiation. Vibrational processes produce relatively very sharp absorption bands for the weathered materials found at the soil surface (Hunt and Salisbury, 1970). No bands due to the fundamental vibrational modes occur in the range short of $2.5 \mu\text{m}$. All features observed in the range short of $2.5 \mu\text{m}$ are exclusively overtones or combinations of tones of fundamental processes in the middle and far infrared (Hunt and Salisbury, 1976, 1970).

Imaging spectrometers are nowadays available aboard spaceborne and airborne systems. The first experiences with imaging spectrometry were with experimental sensors such as AVIRIS and GERIS . The first successful use of imaging spectroscopy was a mineral mapping campaign at Cuprite, Nevada (Kruse et al., 1990). Spectra of kaolinite, alunite and hematite could clearly be identified in the airborne images. Although the results were very good, this technique of mineral and soil mapping is fairly limited to bare or sparsely vegetated areas.

Two operational spaceborne spectrometers are: MODIS: Moderate resolution Imaging Spectrometer and ASTER. MODIS is a 36-channel spectrometer with bands in visible, near infrared, shortwave infrared and thermal wavelengths, its main objective is to collect information for ocean and cloud research. It has a spatial resolution of 250 m: <http://modis.gsfc.nasa.gov/> . Aster has bands in visible, near and mid infrared and thermal infrared. More information is available on: <https://asterweb.jpl.nasa.gov/index.asp>.

Hyperspectral remote sensing can also be used for ecological purposes, for instance determining biodiversity of an area. Species assemblages can be distinguished, but also species of e.g. single trees can be identified (Turner et al., 2003). Hyperspectral remote sensing can also be used for detailed land cover classification. For instance, Bachmann et al. (2002) used the airborne HyMap imaging spectrometer to be able to distinguish the rapidly varying land cover types on a barrier island, where six to seven very different vegetation zones may occur over a distance as little as 50m (figure 6.10). Imaging spectroscopy can also be essential in the assessment of environmental disasters, for instance the 2010 Deep Water Horizon Oil Spill in the Gulf of Mexico. Oil has a distinctive spectral profile due to three absorption features caused by the C-H bond. So, AVIRIS images were used to determine the location and extent of the oil on the surface of the ocean (Clark et al. 2010).



Figure 6.10: Supervised land cover classification based on HyMap imagery (Bachmann et al., 2002).

6.6 Remote Sensing projects in the Netherlands

The Dutch government has financially been stimulating research to and applications of remote sensing technology for several years. This resulted in the establishment of the Netherlands Space Office (NSO). The NSO acts as the Dutch agency for space affairs. It is the face of the Dutch space community for international space organisations like ESA, NASA and JAXA as well as the central point of contact for the space community within the Netherlands (spaceoffice.nl). The result is that many research institutes, universities and commercial companies have activities in this field. A few important projects are mentioned in this section. More info is available on: www.spaceoffice.nl

Monitoring of Heather Vegetation (HEIMON: Heidevergrassing-project)

Dutch heathlands are being exposed to environmental threats such as acid rain and a surplus of fertilizer in the groundwater. As a result heather vegetation is choked by grassy species. A remote sensing/GIS system was built to make an inventory of the condition of the Dutch heather vegetation. Institutes involved comprised the Utrecht University (Faculty of Geographical Sciences), the National Institute for Nature Conservation (RIN) and Eurosense b.v. The differences between the infrared and visible reflectance of heather vegetation and grassy species enable the distinction between affected areas and healthy heather vegetation. Remote sensing images (Landsat TM and multi-spectral SPOT) were used to create time series of heather development. The high spatial resolution of SPOT proved to be useful as the Dutch heathlands are rather small and scattered. The GIS/remote sensing system provides the heathland manager with information on the conditions of the vegetation and provides them a basis for sustainable management of these Dutch ecosystems. A detailed project description is available from Moen et al. (1991).

Land use mapping of the Netherlands

(Landelijke Grondgebruiksklassificatie van Nederland: LGN, www.lgn.nl)

Information on land use is required by many managing organizations concerned with environmental planning, agricultural statistics, groundwater control etc. For that reason a project was initiated in 1988 to collect information on land use and land cover from satellite images. The institutes involved were the Winand Staring Centre (Wageningen) and DHV consultants. A cloud-free mosaic of Landsat TM images of 1986 was created. An inventarisation of land cover and land use was made in training areas for each physiographic unit (sandy soils, peat soils, clay soils etc.). Fifteen classes of land use and land cover were distinguished. The overall accuracy was assessed on 67%. The final database of land cover is made available in a geographical information system. A detailed project description can be found in Thunissen et al. (1991).

Monitoring of Water quality

The surface water quality of the large lakes (IJsselmeer, Markermeer etc.) in the Netherlands is very important because they play a key role in the hydrological balance, in the drink water supply for e.g. the city of Amsterdam and in recreational activities. The Ministry of Infrastructure and Environment is responsible for the quality of these surface waters. A project was started in 1986 to study the usefulness of remote sensing as a tool for water quality control. Landsat TM, SPOT and NOAA-AVHRR images were analysed. It was shown that these sensors could detect spatial patterns of suspended matter and chlorophyll. Problems were identified with the high temporal dynamics of the surface water systems. NOAA-AVHRR can potentially provide an image every day but its spatial resolution is too small to detect the patterns of pollutants accurately. Landsat and SPOT only acquire an image every 16 days (if cloud cover does not prevent image registration), which is not sufficient to monitor highly dynamic systems such as surface water quality. A detailed project description is available in Buiteveld (1988). Between 2011 and 2013 a project called ALGWAD was instigated by Vrije Universiteit Amsterdam, the Institute for Environmental Studies and Water Insight in order to monitor the water quality of the Waddenze to help muscle farmers. Using MERIS imagery algae blooms could be tracked and the farmers could act. Alternatively, suspended matter in the form of sediment can be tracked (figure 6.11).

Vegetation and habitat monitoring

Wageningen University, Alterra, and the Ministry of Economic Affairs set up a project to investigate the possible uses of Remote Sensing for the monitoring of vegetation and ecologically valuable habitats in the Netherlands. Vegetation and habitat monitoring is very time and effort consuming, so policymakers run the risk that habitat deterioration is noted too late. Therefore remote sensing can be a very valuable asset in ecological preservation . Spaceborne or airborne, hyperspectral or microwave, anything can contribute in some way (Alterra, 2015).

Airborne DAIS7915 Experiments in the Peyne area, France.

The Department of Physical Geography is since 1997 involved in investigating the use of airborne imaging spectroscopy for environmental mapping. We determine the possibilities of mineral mapping in this study area using spectroscopic techniques, the possibilities of assessing canopy structural and chemical properties such as biomass and chlorophyll contents. Graduate and under graduate students are involved in these projects.

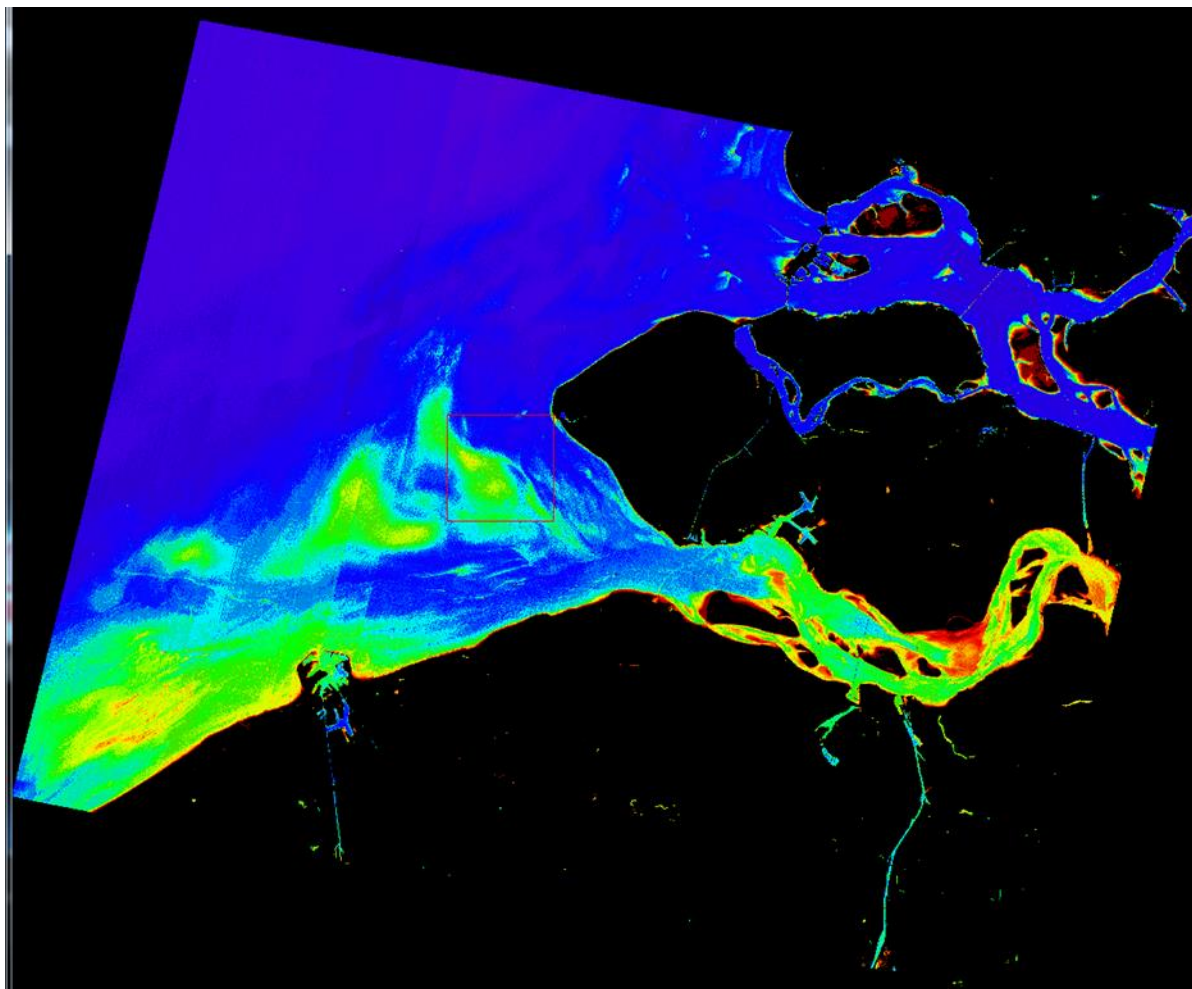


Figure 6.11: Suspended matter in the Westerschelde in the Netherlands.

7. Remote Sensing Software and Geographical Information Systems

7.1 Introduction

For many environmentalists remote sensing is a tool to collect information on the natural conditions of vegetation or soils in their study area. Somehow this information has to be extracted from the acquired images. Consequently, various software packages have been developed that can process raw images. However, a e.g. classified remote sensing image is not a final product. The airborne or space born digital images must be combined with other sources of information or serve as an input for hydrological models, erosion models for bird or animal migration. Other sources of information comprise spatial (soil maps, vegetation maps, digital elevation models, hydrological networks, roads, administrative boundaries) and non-spatial information or databases (e.g. climate data).

7.2 Remote Sensing Software

ERDAS and ENVI

The Erdas Imagine (Hexagon Geospatial) and ENVI (Exelis) are widely used programs for the analysis of raster data. They both allow the user to prepare, enhance and display images for use in GIS or other software. Data values inherent to images (hyperspectral, radar) can be manipulated in order to make certain features visible that would otherwise be hidden. Images can be radiometrically or geometrically corrected, objects can be identified, classified or otherwise extracted, allowing for further analysis. ENVI differs from ERDAS mostly in that ENVI has its own programming language associated with it, and it allows for somewhat more complicated image manipulation. ERDAS is used in the BSc Remote Sensing course, while ENVI is applied in the MSc course.

More information can be found on their respective websites:

<http://www.hexagongeospatial.com/products/producer-suite/erdas-imagine> and

<http://www.exelisvis.com/ProductsServices/ENVIProducts.aspx>

eCognition

eCognition introduced the computer method for extracting information from images using a hierarchy of image objects (groups of pixels) as opposed to traditional pixel processing methods. The technology examines pixels not in isolation, but in context. It builds up a picture iteratively, recognizing groups of pixels as objects. It uses the colour, shape, texture and size of objects as well as their context and relationships to draw conclusions and inferences, similar to a human analyst. eCognition is especially suited for object-based image analysis. It allows you to work with all kinds of geospatial data: raster, vector, point-clouds, etc.

Visit <http://www.ecognition.com/> for more information.

Agisoft Photoscan

Agisoft Photoscan is a software package developed for the processing of UAV acquired images. It allows you to load the images and accompanying EXIF file containing camera and GPS information, and create a single, large image. This stitched image can then be georeferenced by adding of ground control points. This ortho-rectified mosaic image can then be exported into any program for further analysis. Due to the stereo-imaging provided by UAVs, Photoscan can create 3D-point clouds from which Digital Elevation Models can be extracted.

Visit <http://www.agisoft.com/> for more information.

7.2 Data Integration Issues

A GIS or Geographical Information System is a computer system to store, process and display spatial and non-spatial information. As remote sensing images are already available in digital format, it is very easy to combine remote sensing data with data stored in a GIS. Figure 7.1 shows the principle of an integrated database containing remote sensing images, GIS maps and non-spatial information). Well known GIS programs are ArcGIS by ESRI.inc, or the free and open source software QGIS. Many image analysis programs, including ENVI and ERDAS already incorporate options to export images to a ArcGIS format.

The combination of images or maps from different sources requires an accurate geometric match. Consequently, geometric corrections are often necessary before the data can be integrated. Apart from geometric distortions the two images or maps may have a different pixel size. Resampling procedures can be helpful to overcome these problems. Resampling algorithms may work reasonable well for continuous data e.g. reflectance values, elevation information or groundwater levels. It is much more difficult to compute new pixel values for classified maps. Land use classes cannot be averaged, and other methods such as majority filters must be applied. A majority filter attaches the most occurring class in the input kernel to the output cell.

7.3 Modelling Spatial Processes in a GIS using Remote Sensing Data

Models are used to represent complex processes such as erosion or evapotranspiration because the scientific knowledge is lacking to describe that process exactly. A model is a simplified representation of reality, which describes the object or the process in a formal, structured way. Models can help us to increase our understanding of the process: they offer the opportunity to explore scenarios and to assess the importance of each individual input variable. The use of remote sensing information as input to a model requires that:

- The scale at which the model predicts the processes should match the scale of the images;
- The time-scale of the model should match the acquisition frequency of the images;
- It should be feasible to derive some of the model inputs from digital images.

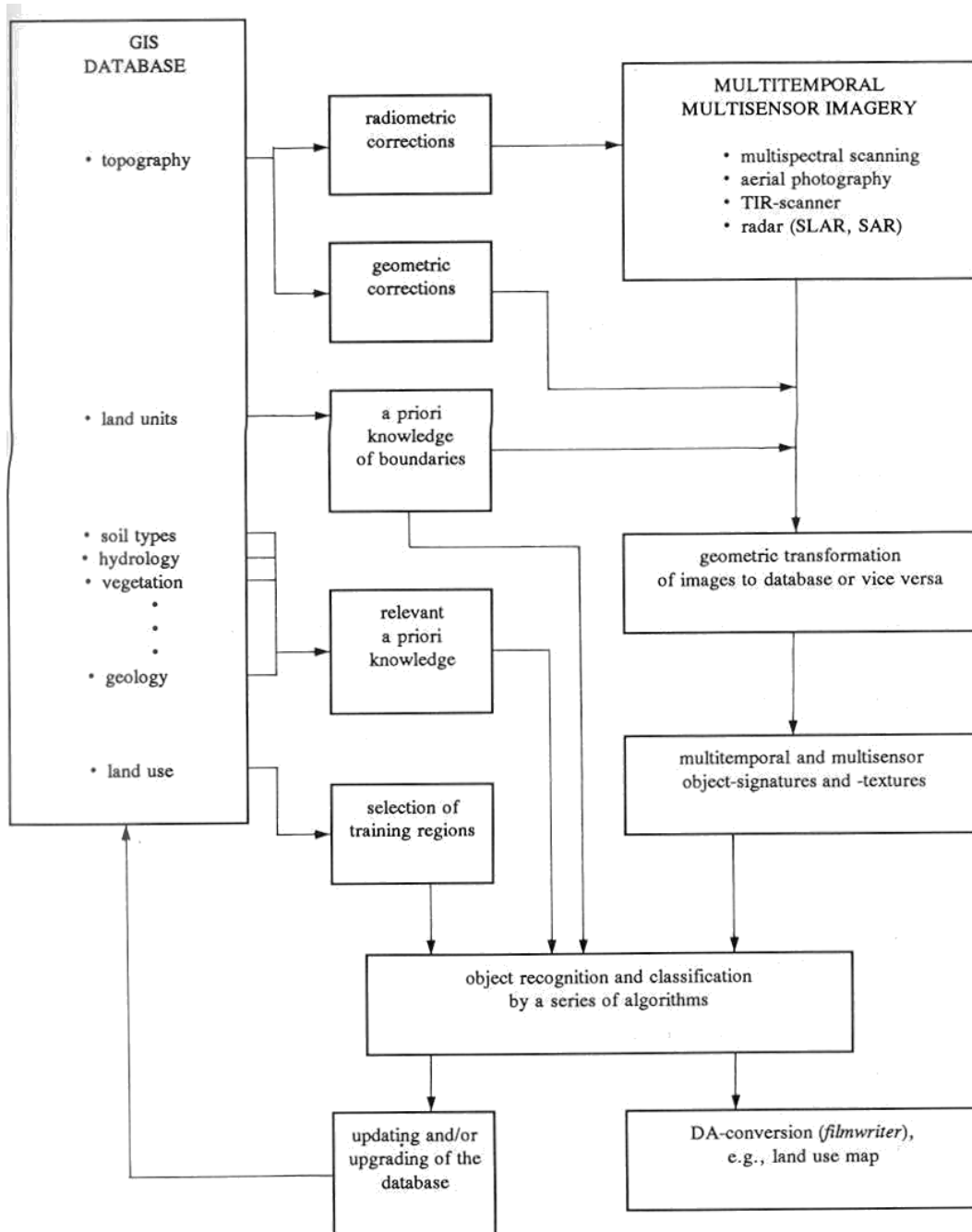


Figure 7.1: Integrated image processing and analysis by means of a GIS (Buiten & Clevers, 1993).

The scale of the image and the model should match because it does not make sense to model erosion or transpiration processes at field size using images with pixels of 1 km². The same is true for the time-scale, some models are developed to forecast e.g. soil losses of single storm events. Remote sensing input requires models that give long-term, e.g. seasonal or annual values. Furthermore, it is important that the model is based on variables that can indeed be derived from remotely sensed images. Consequently, other conditions to be fulfilled by the model are:

- It should be based on the concepts of the erosion process;

- The model can simulate the effects of temporal changes in land use and land management;
- The model should match the distributed character of remote sensing;
- The model should be validated for a number of study areas under a range of natural conditions.

Examples of modelling spatial processes in a GIS with input from remote sensing data can be found in De Jong (1994a), Nieuwenhuis (1993), Nieuwenhuis et al. (1985) and Menenti (1993, 1980). And more recently, in Thorp et al. (2015), Satapathy and Syed (2015) and Errico et al. (2015).

Information sources and important addresses:

GLOVIS: the satellite data portal

At the USGS Global Visualization Viewer <http://glovis.usgs.gov/> you can search and order selected satellite and aerial data. Landsat, ASTER and MODIS data can be accessed for free.

Netherlands Space Office

The Netherlands Space Office acts as the Dutch agency for space affairs. The Netherlands Space Office (NSO) was established by the Dutch government in order to develop the Netherlands' space programme and to bring that programme to action. The NSO is the face of the Dutch space community for international space organisations like ESA, NASA and JAXA as well as the central point of contact for the space community within the Netherlands. The NSO also works to innovatively and openly bring the story of spaceflight science, usage and exploration to teachers, students and the general public (spaceoffice.nl).

Visit their website: www.spaceoffice.nl for more information, and <http://www.spaceoffice.nl/nl/Satellietdataportaal/> for data access.

Kring voor Remote Sensing, now: Geo-information Netherlands

The 'Kring' is a Dutch organization for remote sensing, it provides news and information on remote sensing activities in its newsletters, it organizes symposia and excursions. Everybody interested in remote sensing can become a member (students are also welcome). Personal yearly membership is around Euro 25. In 2004 the Kring merged into GIN: Geo-informatie Nederland and can be accessed at <https://www.geo-info.nl/>

KNMI: Koninklijk Nederlands Meteorologisch Instituut, De Bilt (<http://www.knmi.nl/>).

Postbus 201
3730 AE De Bilt
Tel. 030-206670

The KNMI has a ground station to receive NOAA-AVHRR and Meteosat images and facilities to process these images.

Wageningen University Library: <http://library.wur.nl/>)

Droevedaalsesteeg 2
6708 PB

WageningenThe WUR -library has the largest collection of remote sensing publications in the Netherlands.

NPOC-NLR: National Point of Contact, Nederlands Lucht en Ruimtevaart Laboratorium.

National Point of Contact
Nederlands Lucht- en Ruimtevaart Laboratorium: <http://www.nlr.nl/NL/>
Postbus 153
8300 AD Emmeloord.

The NPOC provides information on all types of remote sensing imagery. The NPOC assists with ordering satellites images such as Landsat, SPOT, ERS etc. Furthermore, they provide technical assistance with data conversion, preprocessing of images and making hardcopies.

National and International Periodicals:

Remote Sensing Journals, ordered by impact factor:

1. Remote Sensing of Environment
2. ISPRS Journal of Photogrammetry and Remote Sensing
3. IEEE Transactions on Geoscience and Remote Sensing
4. Applied Earth Observation and Geoinformation
5. IEEE Applied Earth Observations and Remote Sensing
6. Remote Sensing
7. Photogrammetric Engineering and Remote Sensing
8. IEEE Geoscience and Remote Sensing Letters
9. International Journal of Remote Sensing
10. Remote Sensing Letters
11. Canadian Journal of Remote Sensing
12. GIScience & Remote Sensing
13. The Photogrammetric Record
14. Journal of Applied Remote Sensing

Other journals and sources of information:

EARSEL Advances in Remote Sensing. www.earsel.org

ESA Bulletin

Geocarto International

Mapping Awareness

Pattern Recognition Letters

Remote Sensing Reviews (1983-2001). Now incorporated into International Journal of Remote Sensing.

Many journals are nowadays also available over the internet, consult the library network.

References and further reading:

- ASD, website: <http://www.geo-airbusds.com/>. Accessed between 1-10-2015 and 29-10-2015.
- Asrar G. (Ed.), 1989, Theory and Applications of Optical Remote Sensing. New York, Wiley. 725 pp.
- ASTER (2003), Advanced Spaceborne Thermal Emission and Reflection Radiometer (ASTER). WWW document, <http://asterweb.jpl.nasa.gov>, accessed on 01/05/2005.
- Azzali S., 1985, Greenness and Brightness Formulae Applicable to East Sesia and Grande Bonifica Ferrarese. Institute for Land and Water Management Research, Note 1673. Wageningen, The Netherlands.
- Bachmann, C.M., Donato, T.F., Lamela, G.M., Rhea. W.J. ,Bettenhausen, M.H., Fusina, R.A., Du Bois, K.R. Porter, J.H. and Truitt, B.R., 2002. Automatic classification of land cover on Smith Island, VA, using HyMap imagery. IEEE Transactions on Geoscience and Remote Sensing, 40 (10), pp. 2313-2330.
- Buitenh J.H. & J.G.P.W. Clevers, 1993, Land Observation by Remote Sensing: Theory and Applications. Gordon and Breach, Reading. 642 pp.
- Campbell J.B., 1987, Introduction to Remote Sensing. New York, Guilford Press.
- Chander G., B.L. Markham & D.L. Helder, 2009, Summary of current radiometric calibration coefficients for Landsat MSS, TM, ETM+, and EO-1 ALI sensors. Remote Sensing of Environment 113, 893-903.
- Clark, R.N., Swayze, G.A., Leifer, I. Livo, K.E., Kokaly, R., Hoefen, T., Lundein, S., Eastwood, M., Green, R.O., Pearson, N., Sarture, C., McCubbin, I., Roberts, D., Bradley, E., Steele, D., Ryan, T., Dominguez, R., and the Air borne Visible/Infrared Imaging Spectrometer (AVIRIS) Team, 2010, A method for quantitative mapping of thick oil spills using imaging spectroscopy: U.S. Geological Survey Open-File Report 2010-1167, 51 p.
- Clevers J.G.P.W. and R.E. Jongschaap, 2003, Imaging Spectrometry for Agricultural Applications. In: F.D. van der Meer & S.M. de Jong, Imaging Spectrometry, Basic Principles and Prospective Applications. Kluwer Academic, Dordrecht. Pp.157-200.
- CNES, websites: <https://spot.cnes.fr/>, <https://pleiades.cnes.fr/>. Accessed between 1-10-2015 and 29-10-2015.
- Cohen W.B., 1991, Temporal versus Spatial Variation in Leaf reflectance under Changing Water Stress Conditions. International Journal of Remote Sensing, Vol.12, pp. 1865-1876.
- Crist E.P. & R.J. Kauth, 1986, The Tasseled Cap De-Mystified. Photogrammetric Engineering & Remote Sensing, Vol.52, pp.81-86.
- Crist E.P. & R.C. Cicone, 1984a, A Physically Based Transformation of Thematic Mapper Data: the TM Tasseled Cap. IEEE Transactions on Geoscience and Remote sensing, Vol. GE-22, pp.256-263.
- Crist E.P. & R.C. Cicone, 1984b, Comparisons of the Dimensionality and Features of Simulated Landsat-4 MSS and TM Data. Remote Sensing of Environment 14, pp.235-246.
- Crist E.P. & R.J. Kauth, 1986, The Tasseled Cap De-Mystified. Photogrammetric Engineering & Remote Sensing, Vol.52, pp.81-86.
- Crist E.P., R. Laurin & R.C. Cicone, 1986, Vegetation and Soils Information Contained in Transformed Thematic Mapper Data. Proc. of the International Geoscience and Remote Sensing Symposium (IGARSS'86), Zurich 8-11 Sept, pp.1465-1470.
- Curran P.J., 1986, Principles of Remote sensing. Essex, Longman Group, 282 pp.
- De Jong S.M. & F.D. Van de Meer F.D. (Eds.), 2004, Remote Sensing Image Analysis: Including the Spatial Domain. Bookseries on Remote Sensing Digital Image Processing Vol.5. Kluwer Academic Publishers, Dordrecht. ISBN: 1-4020-2559-9, 359 pp.

- De Jong S.M. & P.A. Burrough, in press, A Fractal Approach to the Classification of Mediterranean Vegetation Types in Remotely Sensed Images. Accepted for publication in Photogrammetric Engineering & Remote Sensing.
- De Jong S.M., 1994a, Applications of Reflective Remote Sensing for Land Degradation Studies in a Mediterranean Environment. *Netherlands Geographical Studies* 177, KNAG Utrecht, 240pp.
- De Jong S.M., 1994b, Derivation of Vegetative Variables from a Landsat TM Image for Erosion Modelling. *Earth Surface Processes and Landforms*, Vol.19, pp.165-178.
- De Jong S.M., 1993, An Application of Spatial Filtering Techniques for Land Cover Mapping Using TM-images. *Geocarto International*, Vol.8, pp. 43-50.
- De Jong S.M. & H.TH. Riezebos, 1991, Use of a GIS-database to Improve Multispectral Image Classification Accuracy. *Proc. EGIS*, 2-5 April, Brussels, pp. 503-508.
- Elvidge C.D., 1990, Visible and Near-Infrared Reflectance Characteristics of Dry Plant Materials. *International Journal of Remote Sensing*, Vol.11, pp.1775-1795.
- ERDAS Inc., 1993, Field Guide and User's Manual ERDAS, Atlanta USA.
- Errico, A., Angelino, C.V., Cicala, L., Persechino, G., Ferrara, C., Lega, M., Vallario, A., Parente, C., Masi, G., Gaetano, R., Scarpa, G.de, Amitrano, D., Ruello, G., Verdoliva, L. and Poggi, G., 2015. Detection of environmental hazards through the feature-based fusion of optical and SAR data: a case study in southern Italy. *International Journal of Remote Sensing* , 36 (13), pp. 3345-3367.
- ESA, 1993, ERS Users Handbook, Revision 1. ESA technical Report SP-1148, Estec, Noordwijk.
- ESA, websites www.esa.int, earth.esa.int, sentinel.esa.int. Accessed between 1-10-2015 and 29-10-2015.
- FAO, 1993, Radar imagery: theory and interpretation. RSC series No.67. Food and Agricultural Organization, Rome.
- Galli de Paratesi S. & P. Reiniger (Eds.), 1987, Heat Capacity Mapping Mission. Investigation No.25 Tellus Project. Technical Report JRC, Ispra.
- Goel, N.S. (1989), Inversion of Canopy Reflectance Models for Estimation of Biophysical Parameters from Reflectance Data. In: G. Asrar Ed., Theory and Applications of Optical Remote Sensing. Wiley, New York, pp. 205-251.
- Goetz A.F.H., G. Vane, J.E. Solomon & B.N. Rock, 1985, Imaging Spectrometry for Earth Remote Sensing. *Science* Vol. 228, pp. 1147-1153.
- Gonzalez R.C. & P. Wintz, 1987, Digital Image Processing. Addison-Wesley Pub. 503 pp.
- Graetz R.D. (1990), Remote Sensing of Terrestrial Ecosystem Structure: An Ecologist's Pragmatic View. In: R.J. Hobbs & H.A. Mooney, Remote Sensing of Biosphere Functioning. *Ecological Studies* 79. Springer-Verlag, New York. pp. 5-30.
- Guyot G., F. Baret & S. Jacquemoud, 1992, Imaging Spectroscopy for Vegetation Studies. In: F. Toselli & J. Bodechtel, Imaging Spectroscopy: Fundamentals and Prospective Applications. Kluwer Academic, Dordrecht, pp.145-165.
- Hansen R.F., 2001, Radar Interferometry: Data Interpretation and Error Analysis. Kluwer Academic Publishers, Dordrecht.308 pp.
- Huete A.R., 1989, Soil Influences in Remotely Sensed Vegetation Canopy Spectra. In: G. Asrar (Ed.), Theory and Applications of Optical Remote sensing. Wiley & Sons, New York, pp.107-141.
- Hunt G.R. & J.W. Salisbury, 1976, Visible and Near Infrared Spectra of Minerals and Rocks: XI. Sedimentary Rocks. *Modern Geology*, Vol.5, pp. 211-217.
- Hunt G.R. & J.W. Salisbury, 1971, Visible and Near Infrared Spectra of Minerals and Rocks: II. Carbonates. *Modern Geology*, Vol.2, pp.23-30.
- Janssen L.L.F., 1994, Methodology for Updating Terrain Object Data from Remote sensing Data. Thesis, Agriculture University Wageningen. 173 pp.
- Jenssen J.R., 2000, Remote Sensing of the Environment. Prentic Hall Int. London, 544pp.

- Kaufman Y.J., 1989, The Atmospheric Effect on Remote sensing and its Correction. In: G. Asrar (Ed.), Theory and Applications of Optical Remote sensing. Wiley & Sons, New York, pp.336-428.
- Kaufman Y.J. & C. Sendra, 1988, Algorithm for Automatic Atmospheric Corrections to Visible and Near-Infrared Satellite Imagery. Int. Journal of Remote Sensing 9, pp. 1357-1381.
- Kauth R.J. & G.S. Thomas, 1976, The Tasseled Cap, a Graphic Description of the Spectral-temporal Development of Agricultural Crops as Seen by Landsat. Proc. Symp. Machine Processing of Remotely Sensed Data. Purdue University, West Lafayette, Indiana, pp.41-51.
- Kloosterman E.H., H.T.C. van Stokkom & R.W.L. Jordans, 1991, Bruikbaarheid van de CAESAR-scanner voor Operationele Vegetatiekartering. BCRS-rapport 91-39, Delft.
- Kenizys F.X. et al., 1988, User's Guide to LOWTRAN7, AFGL-TR-88-0177, Environmental Research Paper No. 1010, Airforce Geophysics Laboratory, Hanscom AFB, Massachusetts.
- Kruse F.A., Kierein-Young K.S. & Boardman J.W., 1990, Mineral Mapping at Cuprite, Nevada with a 63-Channel Imaging Spectrometer. Photogrammetric Engineering & Remote Sensing, Vol.56, pp. 83-92.
- Lu, D. Corresponding author, Mausel, P., Brondízio, E. and Moran, E. ,2004. Change detection techniques. International Journal of Remote Sensing, 25 (12), pp. 2365-2401. DOI: 10.1080/0143116031000139863
- Lunetta R.S. and C. Elvidge, 1999, Remote Sensing Change Detection. Taylor & Francis, 320pp.
- Mas J.F., 1999, Monitoring Land Cover Changes: a Comparison of Change Detection Techniques. International journal of Remote Sensing 20, pp. 139-152.
- LANDSAT (2003). "USGS Landsat Project." WWW document, <http://landsat7.usgs.gov> accessed 03/12/2003
- Lillesand T., R.W. Kiefer & J. Chipman, 2015, Remote Sensing and Imgae Interpretation. Wily, New York. 768pp.
- Markham B.L. & J.L. Baker, 1986, EOSAT Landsat Technical Notes No.1. EOSAT, Lanham, Maryland, pp.1-8.
- Markham, B.L. & J.L. Baker, 1985, Spectral Characterization of the Landsat Thematic Mapper Sensors. International Journal of Remote Sensing, Vol.6, pp.697-716.
- Menenti M., 1993, Contribution of Remote Sensing to the Management of Water in Arid Areas. In: H.J. Buitenhuis & J.G.P.W. Clevers (Eds.), Land Observation by Remote Sensing: Theory and Applications Pudoc, Wageningen, pp.385-401.
- Menenti M., 1980, Physical Aspects and Determination of Evaporation in Deserts Applying Remote Sensing Techniques. PhD-thesis & Report 10 DLO Staring Centrum, Wageningen.
- MODIS, 2003, Moderate Resolution Imaging Spectroradiometer. <http://modis.gsfc.nasa.gov/>, accessed on 01/05/2005.
- Moen J.P., F.J.M. van der Wel, J.T. de Smidt, L.L. Vels & D.J. Harms, 1991, Monitoring van Heidevergrassing met behulp van Remote Sensing en een Geografisch Informatiesysteem (HEIMON). BCRS rapport 91-12, Delft.
- Mücher, C.A., van der Wijngaart, R., Huiskes, H.P.J., Meijninger, W.M.L. and Schmidt, A.M.,2015. Mogelijkheden van Remote Sensing voor vegetatiemonitoring in Nederland; Verkenning van de toegevoegde waarde van de huidige Remote Sensing-technieken op gangbare methoden voor de monitoring en beoordeling van de kwaliteit van beheertypen en habitattypen. Wageningen, Alterra Wageningen UR (University & Research centre), Alterra-rapport 2591. 116 p.p.48
- Mulders M.A., 1987, Remote Sensing in Soil Science. Developments in Soil Science 15. Elsevier, Amsterdam, 379 pp.
- NASA, websites: www.nasa.gov, <http://landsat.gsfc.nasa.gov>, <http://weather.msfc.nasa.gov/GOES/>, <http://trmm.gsfc.nasa.gov/>. Accessed between 1-10-2015 and 29-10-2015.

- Nieuwenhuis G.J.A., 1993, Agrohydrological Applications of Remote Sensing. In: H.J. Buiten & J.G.P.W. Clevers (Eds.), Land Observation by Remote Sensing: Theory and Applications Pudoc, Wageningen, pp.373-384.
- Nieuwenhuis G.J.A., E.H. Smidt & H.A.M. Thunissen, 1985, Estimation of Regional Evapotranspiration of Arable Crops from Thermal Infrared Images. International Journal of Remote Sensing 6, pp.1319-1334.
- Peterson D.L., J.D. Aber, P.A. Matson, D.H. Card, N. Swanberg, C. Wessman & M. Spanner, 1988, Remote Sensing of Forest Canopy and Leaf Biochemical Contents. Remote Sensing of Environment 24, pp.85-108.
- Pieters C.M. & P.A.J. Englert (Eds.), 1993, Remote Geochemical Analysis: Elemental and Mineralogical Composition. Cambridge University Press, Cambridge. 594 pp.
- Reeves R.G. (Ed.), 1975, Manual of Remote Sensing. ASPRS, Falls Church.
- Richards J.A., 1986, Remote Sensing Digital Image Analysis, An Introduction. Springer-Verlag, Berlin. 281 pp.
- Roekel, A. van, (2014, January 24). Satelliet helpt mosseltelers. *Kennislink*. Retrieved from www.kennislink.nl 20-10-2015.
- Rosenfield G.H. & K. Fitzpatrick-Lins, 1986, A Coefficient of Agreement as a Measure of Thematic Classification Accuracy. Photogrammetric Engineering & Remote sensing, Vol.52, pp. 223-227.
- Rubin T.D., 1993, Spectral Mapping with Imaging Spectrometers. Photogrammetric Engineering & Remote sensing, Vol.59, pp. 215-220.
- Sabins F.F., 1987, Remote Sensing: Principles and Interpretation. Freeman and Company, New York, 449 pp.
- Satapathy, I. and Syed, T.H., 2015. Characterization of groundwater potential and artificial recharge sites in Bokaro District, Jharkhand (India), using remote sensing and GIS-based techniques. Environmental Earth Sciences, 74, pp. 4215-4232.
- Sellers P.J., 1989, Vegetation-Canopy Spectral Reflectance and Biophysical Processes. In: G. Asrar (Ed.), Theory and Applications of Optical Remote sensing. Wiley & Sons, New York, pp.297-335.
- Singh A., 1986, Digital Change Detection Techniques using Remotely Sensed Data. International Journal of Remote Sensing 6, pp.989-1003.
- Strahler A.H., 1980, The Use of Prior Probabilities in Maximum Likelihood Classification of Remotely Sensed Data. Remote Sensing of Environment 10, pp.135-163.
- Tanré D., C. Deroo, P. Duhaut, M. Herman, J.J. Morcette, J. Perbos & P.Y. Deschamps, 1985, Effects Atmosphérique en Télédétection, Logiciel de Simulation du Signal Satéllitaire dan le Spectre Solaire. Proc. 3rd Int. Coll. on Spectral Signatures of Objects in Remote Sensing, 16-20 December, Les Arcs, pp.315-319.
- TERRA, 2005, TERRA, The EOS Flagship. WWW document, <http://terra.nasa.gov/> accessed 01/05/2005.
- Thorp, K.R., Hunsaker, D.J., French, A.N., Bautista, E. and Bronson, K.F., 2015. Integrating geospatial data and cropping system simulation within a geographic information system to analyze spatial seed cotton yield, water use, and irrigation requirements. Precision Agriculture, 16 (5), p.p. 532-557.
- Thunissen H., R. Olthof, P. Getz & L. Vels, 1991, Grondgebruiksdatabase van Nederland met behulp van Landsat Thematic Mapper Opnamen. BCNS rapport 91-32, Delft.
- Tucker C.J., 1979, Red and Photographic Infrared Linear Combinations for Monitoring Vegetation. Remote Sensing of Environment 8, pp.127-150.
- Tucker C.J., J.A. Gatlin & S.R. Schneider, 1984, Monitoring Vegetation in the Nile Delta with NOAA-6 and NOAA-7 AVHRR imagery. Photogrammetric Engineering and Remote Sensing 50, pp. 53-61.
- Tucker C.J., C.O. Justice & S.D. Prince, 1986, Monitoring the Grasslands of the Sahel 1984-1985. Int. J. Remote sensing 7 (11): 1571-1581.

- Van der Meer F.D. & S.M. de Jong (Eds.), 2002, Imaging Spectrometry: Basic Principles and Prospective Applications. Bookseries Remote Sensing and Digital Image Processing Vol.4. ISBN: 1-4020-0194-0. Kluwer Academic Publishers, Dordrecht. 403 pp.
- Vane G. & A.F.H. Goetz, 1988, Terrestrial Imaging Spectroscopy. *Remote Sensing of Environment* 24, pp.1-29.
- Wanders N., D. Karssenberg, M.F.P. Bierkens, R.M. Parinussa, R.A.M. de Jeu, J.C. van Dam, S.M. de Jong, 2012, Observation uncertainty of satellite soil moisture products determined with physically-based modeling. *Remote Sensing of Environment* 127, pp.341-356
- Woodcock C.E., A.H. Strahler & D.L.B. Jupp, 1988a, The Use of Semivariograms in Remote Sensing: I. Scene Models and Simulated Images. *Remote Sensing of Environment* 25, pp.323-248.
- Woodcock C.E., A.H. Strahler & D.L.B. Jupp, 1988b, The Use of Semivariograms in Remote Sensing: II. Real Digital Images. *Remote Sensing of Environment* 25, pp.349-379.

List of Tables and Figures:

Table 2.1: Landsat Sensor band characteristics (http://landsat.gsfc.nasa.gov/ , landsat.usgs.gov)	25
Table 2.2: SPOT characteristics (Source: www.geo-airbusds.com)	26
Table 2.3: Pléiades Characteristics. (Source: www.pleiades.cnes.fr)	28
Table 2.4: Sentinel-2 bands (www.earth.esa.int)	30
Table 2.5: Comparison of Landsat, SPOT and Sentinel 2 instrument characteristics (NASA, CNES, ADS, ESA)	30
Table 2.6: Aster system properties	31
Table 2.7: MODIS system properties (modis.gsfc.nasa.gov)	32
Table 2.8: Technical Specifications of GERIS	34
Table 3.1: Radar wavelengths and frequencies used in remote sensing (<i>Sabins, 1987</i>)	39
Table 4.1: Kinetic versus radiant temperature for four material types	60
Table 5.1: Solar Constant Lookup-table for Landsat ETM+ (nasa.gov), Note that the ETM+ thermal band (6) is excluded	67
Table 5.2: Some examples of digital image filters	75
Table 5.3: Thematic Mapper Tasseled Cap Transformation Coefficients proposed by Crist and Cicone (1984a)	78
Table 5.4: An example of an error matrix	85
 Figure 1.1: A system for electromagnetic Remote Sensing of the Earth including communication facilities	4
Figure 1.2: The four components of a Remote Sensing system (active and passive): the source of radiation, the atmosphere, the Earth surface or objects and the sensor (<i>Wikipedia</i>)	5
Figure 1.3: Electromagnetic radiation (or light) can be represented as waves	6
Figure 1.4: The electromagnetic spectrum. Note the logarithmic scale! (<i>Lillesand & Kiefer, 1994</i>)	7
Figure 1.5: Spectral distribution of energy radiated from a blackbody of various temperatures according to the law of Stefan-Boltzman and the displacement law of Wien (http://woodahl.physics.iupui.edu)	8
Figure 1.6: Atmospheric windows in the visible, infrared and microwave regions of the spectrum. Wavelengths bands of commonly used remote sensing systems are shown (www.intechopen.com/source/html/9531/image6.jpg)	9
Figure 1.7: Atmospheric absorption and atmospheric scattering of electromagnetic radiance by particles in the atmosphere	10
Figure 1.8: Relative scatter as a function of wavelength for various levels of atmospheric haze (<i>Adapted from: Sabins, 1987</i>)	11

Figure 1.9a: Interaction mechanisms between electromagnetic energy and matter (<i>Adapted from: Jenkins, J. on www.slidesharecdn.net</i>).....	12
Figure 1.9b: Illustration of the more complex interaction between electromagnetic radiation, the atmosphere and the Earth's surface (http://atmos.caf.dlr.de/).	13
Figure 1.9c: Distortion of surface material reflectance spectrum by the atmosphere with a) detection of the solar curve from a perfectly reflecting surface in the absence of the atmosphere, b) the effect of the atmosphere on detecting the solar curve, c) detection of the real spectrum distorted by the atmosphere and the solar curve (<i>Richards, 2012</i>).	13
Figure 1.10: Specular and diffuse reflectors (<i>Lillesand & Kiefer, 1994</i>).	14
Figure 1.11: Spectral reflectance curves for vegetation and a number of other objects (www.ccpo.odu.edu).	14
Figure 1.12: Scanning systems for acquiring remote sensing images (www.e-education.psu.edu)	16
Figure 1.13: Diagrammatic representation of a multi-spectral scanner (<i>Curran, 1985</i>).	17
Figure 1.14: A three dimensional space is required to described colour in RS. The Munsell colour systems uses value and chroma instead of intensity and hue respectively (<i>Adapted from: http://www.tomjewett.com/</i>).	18
Figure 1.15: Colour formation on IR colour film (<i>Lillesand & Kiefer. 1994</i>).	19
Figure 1.16: A prism is used to split white light into its individual components (www.epicphysics.com).	20
Figure 1.17: Illustration of how A) wavelength (hue), B) intensity and C) saturation of colour interact and D) mix colours.	20
Figure 2.1: Timeline of the Landsat program (<i>USGS.com</i>).	23
Figure 2.2: From left to right and top to bottom: Landsat 1-8, excluding 6 (http://landsat.gsfc.nasa.gov/).	24
Figure 2.3: Sun-synchronous orbit of Landsat 4 and 5 (<i>CCRS tutorial & Lillesand & Kiefer, 2000</i>).	25
Figure 2.4: An illustration of SPOT off-nadir viewing system (<i>Curran, 1985</i>).	27
Figure 2.5: Illustration of SPOT's stereo-photogrammetric function (www.geo-airbusds.com).	27
Figure 2.6: SPOT program's timeline (www.geo-airbusds.com).	27
Figure 2.7: Sentinel 1-6 (earth.esa.int).	29
Figure 2.8: Comparison of Sentinel 2 bands with those of Landsat 7 and 8 (www.earth.esa.int).	29
Figure 2.9: Concept of imaging spectroscopy.....	35
Figure 2.10: Deploying the SenseFly Swinglet UAV (www.sensefly.com).	36
Figure 3.1: Operating principle of SLAR (<i>Lillesand & Kiefer, 1994</i>).	38
Figure 3.2a: Incidence angle and depression angle (<i>Sabins, 1987</i>).	39
Figure 3.2b: Range, incidence angle, look angle and depression angle (180-look angle) (www.radartutorial.eu).	40
Figure 3.3: Radar resolution in range ($H\beta \cos 2\theta$) and azimuth ($H\beta \cos \theta$) direction with increasing range, with: H = flight altitude, Θ = grazing angle and β = antenna beam width (www.radartutorial.eu).	40
Figure 3.4: Radar resolution in the range (look) direction (<i>Sabins, 1987</i>).	41
Figure 3.5: Radar beam width and resolution in the azimuth direction (<i>Sabins, 1987</i>).	41
Figure 3.6: Synthetic Aperture Radar (SAR) system (<i>Sabins, 1987</i>).	42
Figure 3.7: Concept of Synthetic Aperture Radar (SAR) system cont'd.	43
Figure 3.8: Corner reflection: the microwave radiation is reflected straight back to the antenna (<i>Curran, 1985</i>).	44
Figure 3.9: Radar illumination and shadows at different depression angles (www.radartutorial.eu and <i>Henderson & Lewis, 1998</i>).	44

Figure 3.10: Models of surface roughness criteria and return intensity for a 23.5 cm radar system (<i>Sabins, 1987</i>).....	46
Figure 3.11: Backscatter of natural targets in the microwave spectrum (<i>FAO, 1993</i>)	47
Figure 3.12: The ERS-1(left) and 2 (right) satellites in the test room at ESTEC in Noordwijk NL (<i>earth.esa.int</i>).	49
Figure 3.13: ASCAT swath geometry for an orbit height of 822 km (<i>eumetsat: ASCAT product guide</i>).	51
Figure 3.14: Principle of InSAR (<i>volcano.si.edu</i>).	52
Figure 3.15: A) Radar intensity map of northern Turkey near Izmit and the Black Sea. B) Interferogram constructed of two radar images of 13 August 1999 and 17 September 1999 showing the deformation pattern due to the Izmit earth quake at 17 August 1999 (<i>Hansen, 2001</i>).	52
Figure 3.16: Dyke displacement (www.esa.int , www.hansjebrinker.com).	53
Figure 3.17: GOCE-derived geoid (www.esa.int).	54
Figure 3.18: Representation of how the GOCE gradiometer works (http://www.goce- projektbuero.de/).....	54
Figure 4.1: Spectral emissivities and radiant exitances for a blackbody, a grey body and a selective radiator (<i>Lillesand and Kiefer, 1994</i>).	57
Figure 4.2: Spectral radiance for water (a) versus a blackbody and (b) quartz versus a blackbody (<i>Lillesand and Kiefer, 1994</i>).	58
Figure 4.3: Electromagnetic spectrum showing atmospheric absorption and remote sensing windows. Gasses responsible for atmospheric absorption are indicated. Two thermal atmospheric windows are visible in red: 3 to 5 μm and 8 to 14 μm . The solar emission range is indicated in yellow (<i>adapted from www.helpsavetheclimate.com</i>).	59
Figure 4.4: Schematic diagram showing the effect of differences in thermal inertia on surface temperature during diurnal solar cycles.....	61
Figure 4.5: Colour infrared (left), NDVI (middle) and Thermal (right) image of pivot irrigated crops. Note that the NDVI shows high values for the vegetated areas, while in the Thermal image the vegetation has the lowest values (<i>Gao et al., 2012</i>).	62
Figure 5.1: Arrangement of scan lines and pixels in Landsat MSS and TM images (<i>Sabins, 1987</i>).	64
Figure 5.2: Digital structure of a Landsat TM image (left) and 8 bits radiometric resolution of the pixel values.....	64
Figure 5.3: Effect of the atmosphere on the brightness of a pixel (<i>Richards, 2012</i>).	65
Figure 5.4: a) Transfer characteristic of a radiation detector: gain and offset and b) Hypothetical mismatches in detector characteristics (<i>Richards, 2012</i>).	67
Figure 5.5: Relative scatter as a function of wavelength for various levels of atmospheric haze (<i>Adapted from: Sabins, 1987</i>).	68
Figure 5.6: Illustration of the effect of path radiance resulting from atmospheric scattering (<i>Richards, 2012</i>).	68
Figure 5.7: The six most important flight parameters of an aircraft (<i>Buiten & Clevers 1994</i>).	69
Figure 5.8: Geometric distortions of airborne remote sensing images by aircraft flight movements. 70	
Figure 5.9: Resampling techniques: A) Open circles indicate reference grid from input image (and location determined from topographical map or GPS).	71
Figure 5.10: Principle of contrast stretch enhancement (<i>Lillesand & Kiefer, 1994</i>).	73
Figure 5.11: The effect of a number of digital filter on the profile of a digital image.	74
Figure 5.12: Reflectance spectra of vegetation and dry soil and their computed vegetation index (<i>Sabins, 1987</i>).	76
Figure 5.13: Reduction of scene illumination effects through spectral ratioing (<i>Lillesand & Kiefer, 1994</i>).	77

Figure 5.14: Rotated coordinate system used in a principal component transformation (<i>Lillesand & Kiefer, 1994</i>).....	78
Figure 5.15: Graphical representation of the Tasseled Cap Transformation (<i>Schowengerdt, 1997</i>)	78
Figure 5.16: Spectral Unmixing. The various contributions to the total pixel spectrum (left) are separated into the individual endmembers (http://www.sonybiotechnology.com/sa3800/tech2)....	79
Figure 5.17: Principle of supervised image classification (<i>Lillesand & Kiefer, 1994</i>).	80
Figure 5.18: Minimum distance to mean (top left), maximum likelihood (right) and box (bottom left) classifiers.....	81
Figure 5.19: Illustration of the Euclidean distance measure (http://hlab.stanford.edu).....	82
Figure 5.20: Equiprobability contours defined by the maximum likelihood classifier (<i>Lillesand & Kiefer, 1994</i>).	83
Figure 5.21: Probability density functions defined by the maximum likelihood classifier (<i>Lillesand & Kiefer, 1994</i>).....	83
Figure 5.22: Illustration of spectral angle mapping, using 2 bands (www.exelisvis.com).	84
Figure 6.1: Major influences on spectral properties of a leaf (http://www.gov.scot).	87
Figure 6.2: The effect of a changing canopy on a remote sensing scene.	87
Figure 6.3: NDVI vs chlorophyll content for various LAI's (leaf area index) (<i>Adapted from: Salas and Henebry, 2014</i>).....	88
Figure 6.4: Illustration of the “linear method” (<i>Guyot and Baret, 1988</i>).	89
Figure 6.5: Some examples of soil reflectance spectra (<i>Asrar, 1989</i>).....	89
Figure 6.6: Reflectance spectra of carbonate minerals showing features at 2280 and 2340 nm and minerals showing OH en H ₂ O absorption bands (<i>Asrar, 1989</i>).	90
Figure 6.7: Spectral reflectance curves for wet and dry silty loam and wet and dry clay, and several diagnostic absorption features (<i>Curran, 1986</i>).....	91
Figure 6.8: Temporal profile / phenological cycle of winter wheat (<i>Jensen, 2000</i>).....	92
Figure 6.9: Phenological Cycles of sugar beets, cotton and alfalfa and images collected over a period of 12 months (<i>Jensen, 2000</i>).....	93
Figure 6.10: Supervised land cover classification based on HyMap imagery (<i>Bachmann et al., 2002</i>).	96
Figure 6.11: Suspended matter in the Westerschelde in the Netherlands.	98
Figure 7.1: Integrated image processing and analysis by means of a GIS (<i>Buiten & Clevers, 1993</i>). ..	101